Surface characterization of Pluto, Charon, and (47171) 1999 TC$_{36}$

Von der Fakultät für Elektrotechnik, Informationstechnik, Physik
der Technischen Universität Carolo-Wilhelmina
zu Braunschweig
zur Erlangung des Grades eines
Doktors der Naturwissenschaften
(Dr.rer.nat.)
genehmigte
Dissertation

von Silvia Protopapa
aus Galatina / Italien

To my father

Contents

Summary

Transneptunian objects are among the most primitive bodies of the Solar System, and the investigation of their surface composition provides constraints on the formation and evolution of this population. In this dissertation we apply the Hapke radiative transfer model, which is the most used to describe the properties of planetary regolith, to reproduce the reflectance measurements of three Transneptunian objects: Pluto, Charon, and (47171) 1999 TC_{36}. Retrieving information about the nature and properties of the surface compounds of the analysed bodies is the main goal of this thesis.

The present work casts new light on Pluto and Charon's surfaces, by means of L- and M-band spectroscopy. We present the first resolved Pluto and Charon spectra up to 5 μm and 4 μm, respectively, obtained with the adaptive optics instrument NACO at the ESO Very Large Telescope during 3-7 August 2005. It is the first time that the complete L-band spectrum of Pluto is measured without unresolved contamination by light from Charon and the first M-band spectrum ever measured. A new absorption band centered near 4.6 μm has been detected. CO ice, known to be present on the surface of Pluto, and nitriles, expected but never detected, are proposed as main candidates to explain this signature. A geographic mixture of pure methane ice with two different grain sizes, methane and CO ice diluted in nitrogen, CH_2CHCN, and Titan tholin gives the best-fit to Pluto's spectrum. Differences compared to published Pluto spectra from 2001 taken at similar longitude could be due to a different surface coverage in latitude or to a possible resurfacing process on Pluto. We suggest two possible resurfacing mechanisms to explain the increasing abundance of pure CH_4 from 2001 to 2005: ice condensation from the atmosphere and wind transport of ice grains. These results complement NASA's New Horizons mission, expected to arrive in 2015, that will perform spectroscopy of Pluto's surface in JHK band only.

Our Charon spectrum, the first one in the L-band, is characterized by broad water ice signatures in agreement with the short wavelength measurements. NACO observations for Charon allowed us to compute a standard spectroscopic model for Pluto's moon. This can be used to subtract Charon's contribution from ground-based spectra of the combined Pluto/Charon system.

Near-infrared photometric and spectroscopic observations of (47171) 1999 TC_{36} obtained with the adaptive optics instrument NACO at the ESO Very Large Telescope during 12 October 2006 are presented together with FORS1, ISAAC, and SINFONI spectroscopic observations carried out about one month later on 8 and 9 November 2006. We present the reflectance spectrum of the unresolved binary system (47171) 1999 TC_{36} in the wavelength range between 0.37 and 2.33 μm. The modeling analysis reveals the possible presence on the surface of serpentine. This represents a new step forward the firm identification of hydrated minerals on the surface of Transneptunian objects, important for

the understanding of aqueous alteration processes. An intimate mixture of Triton tholin, Titan tholin, serpentine, and Triton tholin diluted in water ice gives the best-fit to the measured spectrum. Any significant differences from the published spectra of (47171) 1999 TC_{36} taken on 2001 and 2003 could be due to surface heterogeneity.

1 Transneptunian Objects Populations

The detection of 1992 QB$_1$ by Jewitt et al. (1992) marked the discovery of a new frontier of our Solar System. Before this detection, the Kuiper Belt was only an hypothesized population of objects beyond the orbit of Neptune, a possible source of the short period comets (Fernandez and Ip 1981; Duncan et al. 1988). Pluto was considered a unique icy planet in a peculiar orbit at the outer edge of the Solar System. Fifteen years after this discovery more than 1200 new icy bodies have been detected, and Pluto is now recognized as one of the several large bodies in the vast swarm of Transneptunian objects (TNOs)[1] (Brown 2002). Scientific interest in these bodies arises because they are considered to be the most pristine Solar System objects observable from Earth. Improving the knowledge of these distant bodies thus extends the understanding of the origin and evolution of the Solar System. Currently, the study of TNOs is one of the most active frontiers of Solar System research.

This chapter is divided in three parts. The first part is devoted to the description of the current dynamics in the Kuiper Belt (Section 1.1), compared in Section 1.2 with the structure predicted for the long-term dynamical evolution of the Transneptunian region. This will be used to highlight the main physical and dynamical properties of the Kuiper Belt, which are explained by the Nice Model, the most complete scenario for the primordial evolution of the outer Solar System (Section 1.3). In the second part the state-of-the-art of the surface characterization of TNOs, based on ground-based observations, is presented. The importance of the visible and infrared spectroscopy as a tool for understanding the formation and evolution of this population is highlighted (Section 1.4). Finally, the third part of this introduction focuses the attention on the large TNOs (Section 1.5.1) and the multiple systems in the Kuiper Belt (Section 1.5.2). These are two peculiar TNOs populations, which have Pluto, one of the main subject of this thesis, as their best representative. Some information on New Horizons, NASA's Pluto-Kuiper Belt mission is given in Section 1.6. This introduction intends to give a general picture of the context in which this thesis is inserted, in order to understand the motivations and the goals of the presented work (Section 1.7).

1.1 Current short-term dynamics of the Kuiper Belt

A primary goal of this section is to present the orbital structure of the Kuiper Belt. Therefore we introduce in this section the various sub-classes that constitute the Transneptunian

---

[1]Different terms are used in reference to the icy bodies beyond the orbit of Neptune. Many authors use "Kuiper Belt objects" (KBOs), others use "Transneptunian objects" (TNOs). In this thesis the two terms are completely equivalent.

population.

First, it is necessary to define the boundaries of the Transneptunian region: an object is considered a TNO if it has semimajor axis a between 30 and 2000 AU, Tisserand[2] parameter T_J with respect to Jupiter greater than 3.05, and perihelion q greater than 7.35 AU. The populations of bodies that limit TNO semimajor axes are the Centaurs and the Oort Cloud, while the eccentricities e are limited by the Jupiter family comets (see Figure 1.1).
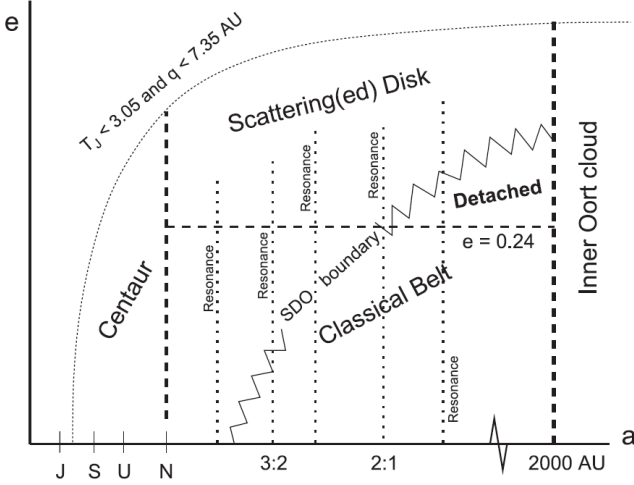
Figure 1.1: A cartoon where the different sub-populations in the Transneptunian region are shown. The x-axis is the semimajor axis, and in the y-axis there is the eccentricity. Source: Gladman et al. (2008).

In this thesis we follow the classification of TNOs introduced by Gladman et al. (2008), that is based on orbital dynamics through a 10 My numerical integration. In this way it is possible to distinguish two main sub-populations in the Transneptunian region: the *resonant* and *non resonant*. The latter is in turn subdivided in three categories: the *scattered disk*, the *detached population*, and the *classical belt*. Figure 1.2 shows the orbital distribution of the sample of TNOs with three or more opposition as presented in the IAU's Minor Planet Center as of May 2006.

---

[2]The Tisserand parameter T_J with respect to Jupiter is defined by the relation

$$T_J = \frac{a_J}{a} + 2 \sqrt{\frac{a}{a_J}(1 - e^2)} \cos i \,, \qquad (1.1)$$

where a, e, and i are the orbital semimajor axis, eccentricity, and inclination, respectively, of the object with respect to Jupiter's orbit and a_J is the semimajor axis of Jupiter (about 5.2 AU) (Gladman et al. 2008).
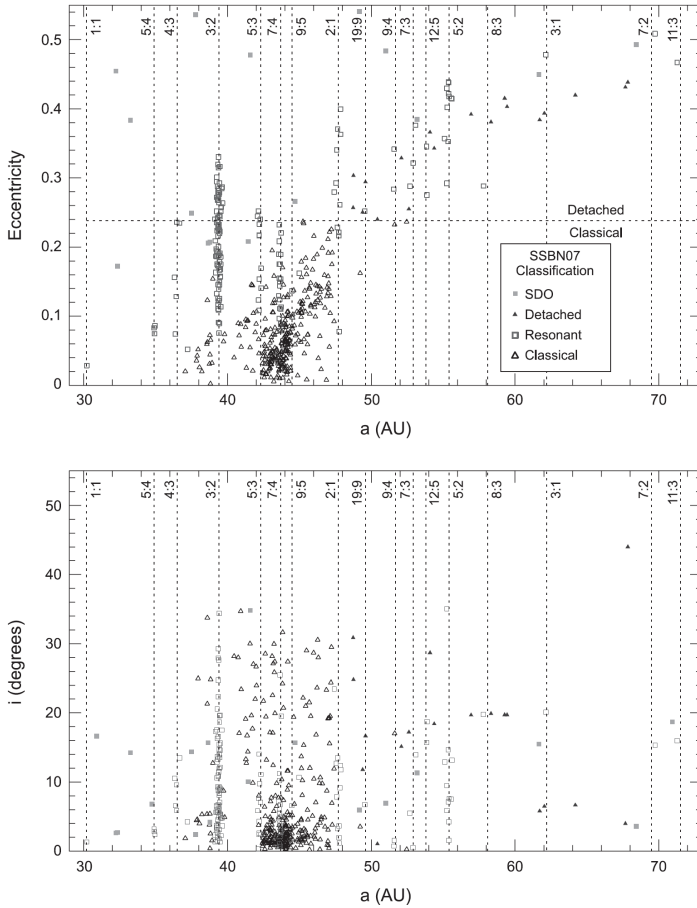
Figure 1.2: The orbital distribution, eccentricity (upper plot) and inclination (lower plot), of TNOs presented by Gladman et al. (2008) for a between 30 and 73 AU. Resonant semimajor axes are labelled and indicated by dotted lines. The horizontal dashed line in the upper plot marks the arbitrary division between the detached TNOs and classical belt. Beyond $a = 73$ AU all objects are detached or are belonging to the scattering disk (SDO), with the exception of two bodies of insecure resonant classification. Source: Gladman et al. (2008).

- **Resonant Objects** The resonant objects (open squares in Figure 1.2) are those trapped in mean motion resonance (MMR) with Neptune. An object is in MMR with Neptune p:q, where p and q are integers, if its orbital period can be expressed in the following way

$$P_{TNO} = \frac{q}{p} P_N \,, \tag{1.2}$$

where P_{TNO} and P_N are the orbital periods of the TNO and Neptune, respectively. We define order of the resonance the difference $p - q$.

The prototype resonant TNO is Pluto, which belongs with other TNOs, *Plutinos*, to the 3:2 MMR at 39.5 AU. The MMR offers a protection mechanism against close encounter with the resonant planet (Morbidelli et al. 2008). In particular, it allows large-*e* orbits to survive for 4.5 Gy despite approach or even crossing of Neptune's orbit (see Section 1.2).

- **Scattered Disk Objects** According to the definition of Gladman et al. (2008), scattering disk objects (SDOs) are those bodies that are currently scattering actively off Neptune. In particular, an excursion in *a* greater than 1.5 AU during the 10 My integration classifies the object as an SDO. This definition does not take into account the origin of these objects and it is purely dynamic. In general, the scattered disk contains those objects that have been lifted into eccentric orbits by weak gravitational interaction from Neptune.

- **The Detached Transneptunian Objects** It is common to find in literature the distinction between scattered objects and detached objects. The detached TNOs, also summarized as "extended scattered disk", are those TNOs with large eccentricities ($e > 0.24$) that are not exposed to gravitational scattering of one of the outer planet, namely of Neptune (see Figure 1.1). The extended scattered disk has probably been generated by perturbations associated with a passing star (Delsanti and Jewitt 2006). The detachment processes of the orbits are still under investigation (Gomes et al. 2008; Morbidelli et al. 2008).

- **The Classical Belt** Gladman et al. (2008) nomenclature deviates from the older publication (Delsanti and Jewitt 2006) that defines the classical TNOs as the non resonant objects between the 3:2 MMR at 39.5 AU and the 2:1 MMR at 48 AU. On the contrary, according to Gladman et al. (2008), the classical belt extends inward the 3:2 MMR to the stable low-e region and outwards to the sparsely populated low-e orbits outside 48 AU. Therefore, it is possible to distinguish within the classical belt between the *inner* classical belt ($a < 39.4$ AU), *outer* classical belt ($a > 48$ AU) and *main* classical belt. Figure 1.2 shows the presence of two sub-populations in the classical region. The low inclination (*cold*) population with $i < 5°$, and the high (*hot*) inclination population that extends to inclinations of 30° to 40°. The terms *hot* and *cold* do not refer to temperature, but rather to the level of dynamical excitation of the bodies (see Section 1.3). The coexistence of these two populations in the Kuiper Belt has puzzled astronomers (Morbidelli and Levison 2003), and it sill does.
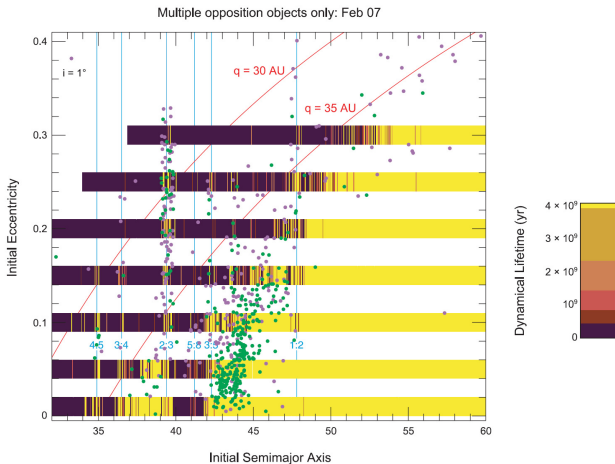
Figure 1.3: The dynamical lifetime for small particles in the Kuiper Belt derived from 4 billion years integrations. Each test particle is represented by a narrow vertical strip, the center of which is located at the particle's initial eccentricity and semimajor axis (initial orbital inclination for all objects is $1°$). The color of each strip represents the dynamical lifetime of the particle. The locations of the important Neptune MMRs are shown in blue and two curves of constant perihelion distance are shown in red. The (a,e) elements of the TNOs with orbits determined over three observed oppositions are also shown. Green dots are for $i < 4°$, magenta dots otherwise. Source: Morbidelli et al. (2008).

1.2   Long-term dynamics of the Kuiper Belt

In the previous section we stated that the MMR offers a protection mechanism against close encounters with the resonant planet allowing large-e orbits to survive for 4.5 Gy despite approaching or even crossing Neptune's orbit (Morbidelli et al. 2008). This conclusion results from simulations performed by Duncan et al. (1995) and Kuchner et al. (2002), that aimed at the understanding of the long-term dynamical behaviour of objects in the Kuiper Belt. One of the results of these simulations is shown in Figure 1.3, in which the dynamical lifetime of TNOs as function of their initial semimajor axis and eccentricity, fixing the inclination at $1°$, is presented. This map has been computed numerically by simulating the evolution of massless particles from their initial conditions, under the gravitational perturbations of the giant planets. The planets were assumed to be on their current orbits throughout the integrations. Each particle was followed until it had close encounter with Neptune. The vertical strips indicate the timespan required for a particle to encounter Neptune as a function of its initial semimajor axis and eccentricity. Strips that are colored yellow represent objects that survive for the complete simulation period, 4×10^9 years (approximately the age of the Solar System), without encountering

the planet. This means that the yellow strips represent objects that are stable over the age of the Solar System. The figure also shows the orbital elements of the known TNOs distinguishing between bodies with inclination less than 4° (green dots) from those (magenta dots) with higher inclination. The locations of important Neptune MMRs are shown in blue, and two curves of constant perihelion distance are shown in red. It must be remarked that the convention adopted in Section 1.1 according to which p:q resonance denotes the resonance of p orbital periods of the inner object (usually Neptune) to q periods of the TNO (see Section 1.1) is not used in the figure. Conversely, in Figure 1.3 the integer p and q refer to the object and Neptune, respectively.

Figure 1.3 shows the complex dynamical structure of the Kuiper Belt, although some general trends can be easily identified. It is clear that objects with perihelion distances less than ~35 AU are unstable. The instability is not due to close encounters with Neptune, but instead due to the overlapping of its outer MMRs. Indeed, it is known that MMRs become wider at large eccentricity and that resonance overlapping produces large scale chaos (Chirikov 1960). The main exceptions from the trend toward instability at small perihelion distances are the objects librating about MMRs with Neptune. As noted by Malhotra (1996), at any resonance one finds a family of stable orbits such that the semimajor axis equals a_{res} for all orbits in this family, and the eccentricity ranges from zero to some maximum value e_{max}; for $e > e_{max}$ the orbit becomes unstable. In some neighbourhood $a_{res} \pm \Delta a$ stable orbits librate with finite amplitude about the exact resonant orbit.

MMRs are not the only important agent governing the dynamics in the Kuiper Belt. For example, Figure 1.3 displays a dark region for $40 < a < 42$ AU. This instability is due to the presence of overlapping secular resonances that occur in this region for objects with low inclination. This means that a low inclination object in this region undergoes large variation in orbital eccentricity, the perihelion distance eventually decreases below 35 AU and the object enters in the scatter(ing/ed) disk. Conversely, a high inclination object in the same semimajor axis region is stable. Indeed, Figure 1.3 shows that many objects with $i > 4°$ (magenta dots) are present between 40 and 42 AU. Only green dots representing low inclination objects are absent. It is interesting to compare the numerical results of the long-term dynamical simulation (Figure 1.3) to the current orbital elements of the known KBOs (Figure 1.2). Effectively, there are no objects with perihelion distances less than 35 AU unless in MMR with Neptune and no objects with low inclination and low eccentricities in the region between 40 and 42 AU. As predicted by the long-term dynamical simulation we observe conspicuous populations of objects in MMRs with Neptune.

1.3 Origin of the dynamical structure in the Kuiper Belt

The described structure of the Kuiper Belt requires an explanation in the framework of the primordial Solar System evolution. In particular, the main properties that need to be explained are the following:

- The existence of conspicuous populations of objects in MMRs with Neptune. It is necessary to understand how and why objects populated these resonances.

- The outer edge of the classical belt (Figure 1.2). This edge appears to be precisely at the location of the 2:1 MMR with Neptune. The low density or absence of low

eccentricity objects beyond the 2:1 MMR is not due to observational bias (Trujillo and Brown 2001).

- The inclination distribution of the classical belt. As mentioned before (see Section 1.1), Figure 1.2 (bottom panel) shows a cluster of objects with low inclination $i \leq 5°$ but also objects with inclination up to 30° or 40°. This cluster persists even considering the biases (Brown 2001).

- The correlations between physical properties and orbital distribution. Levison and Stern (2001) and Grundy et al. (2005) found that the hot population contains bigger objects, while the cold population presents a deficit of gray color bodies with respect to the hot population (Doressoundiram et al. 2001, 2005).

- The existence of the detached objects.

- The mass deficit of the Kuiper Belt. The current mass of the Kuiper Belt (0.01-0.1 $M_{\oplus}$, Earth masses) is 2 or 3 orders of magnitude less with respect to what models say was needed in order for the TNOs to accrete where we see them (Gladman et al. 2001; Bernstein et al. 2004). Detailed modeling of accretion in a massive primordial Kuiper Belt was performed by Stern and Colwell (1997a,b) and Kenyon and Luu (1998, 1999a,b). All the models agree that, in order to reproduce the present size distribution of TNOs, ~10-30 $M_{\oplus}$ of solid material in a dynamically cold disk are needed as initial condition.

1.3.1   The Nice Model

A valid model for the Kuiper Belt's primordial evolution should explain all the properties detailed above. The first model that reproduces many of the characteristics of the outer Solar System is the *Nice model*.

In the Nice model, the giant planets are assumed to be initially on nearly-circular and coplanar orbits, with orbital separations significantly smaller than the ones currently observed. More precisely, the giant planets are confined in the region from ~5.5 to ~14 AU. The gas giants (Jupiter and Saturn) are placed closer to the Sun than the ice giants (Uranus and Neptune). Saturn is assumed to be closer to Jupiter than their mutual 2:1 MMR. In addition to the giant planets, a massive particle disk is assumed to exist beyond the orbit of the giant planets, ending at ~34 AU, and with a surface density that falls linearly with heliocentric distance (Tsiganis et al. 2005; Morbidelli et al. 2008). It has been found by Tsiganis et al. (2005) that in order to accurately reproduce the characteristics of the outer planetary system, the total mass of the disk must have been ~35$M_{\oplus}$.

With the above configuration, the planetesimals at the inner edge of the disk evolve into Neptune scattering orbits on a timescale of a few million years. Consequently, the planets migrate because of the exchange of angular momentum with the disk particles during this process. After a significant period of time, ranging from 350 My to 1.1 Gy, Jupiter and Saturn cross their mutual 2:1 MMR (Gomes et al. 2005). The resonance crossing excites their eccentricities to values slightly larger than those currently observed (see Figure 1.4). The sudden jump in the eccentricities of Jupiter and Saturn has a drastic effect on the planetary system as a whole. The secular perturbations that Jupiter and
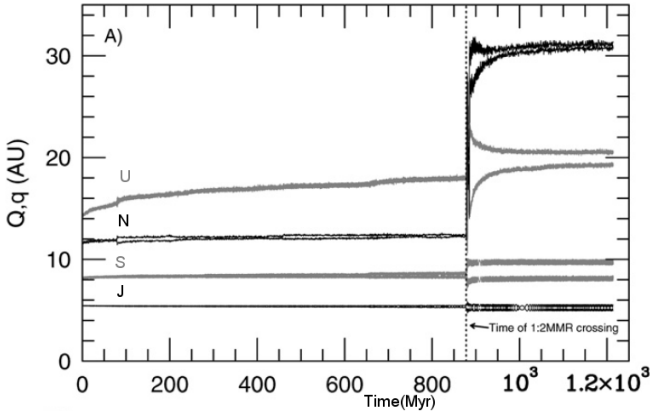
Figure 1.4: The orbital evolution of the giant planets in the Nice model is shown. Two curves are plotted for each planet: the minimum (q) and maximum (Q) heliocentric distances as function of time (My). U is for Uranus, N for Neptune, J for Jupiter and S for Saturn. The separation between the upper and lower curves for each planet is indicative of the eccentricity of the orbit. The vertical dotted line marks the epoch of the 2:1 MMR crossing. Source: Levison et al. (2008).

Saturn exert on Uranus and Neptune force the eccentricities of the ice giants to increase by an amount that depends on the masses and semimajor axes of all planets. As a result of the compactness of the system, the planetary orbits become chaotic and intersect. When this occurs, a short phase of encounters follows the resonance crossing event. These encounters increase the inclinations of the planetary orbits. In addition, both ice giants are scattered outward and penetrate the disk. Thus, the flux of small bodies towards Saturn and Jupiter, and hence their rate of migration, increases abruptly. During this fast migration phase, the eccentricities and inclinations of the planets slowly decrease by dynamical friction and the planetary system is stabilized. The planets stop migrating when the disk is almost completely depleted. The final outcome of the simulations in the Nice model reproduces quantitatively the current architecture of the giant planets, in terms of semimajor axes, eccentricities, and inclinations (Tsiganis et al. 2005). In Figure 1.5 the basic steps of the Solar System evolution in the Nice model are shown.

As described in the Nice model, Neptune undergoes a transient phase during which its eccentricity is high. In many of the simulations performed by Tsiganis et al. (2005) and Gomes et al. (2005) this high eccentricity phase is achieved when Neptune has a semimajor axis of 27-29 AU, after its encounter with Uranus. When Neptune's orbit is eccentric the full (a,e) region up to the location of the 2:1 MMR with Neptune is chaotic, even for small eccentricities. When Neptune is at ~28 AU a large portion of the current Kuiper Belt is already inside of the location of the 2:1 MMR with Neptune. Thus, the
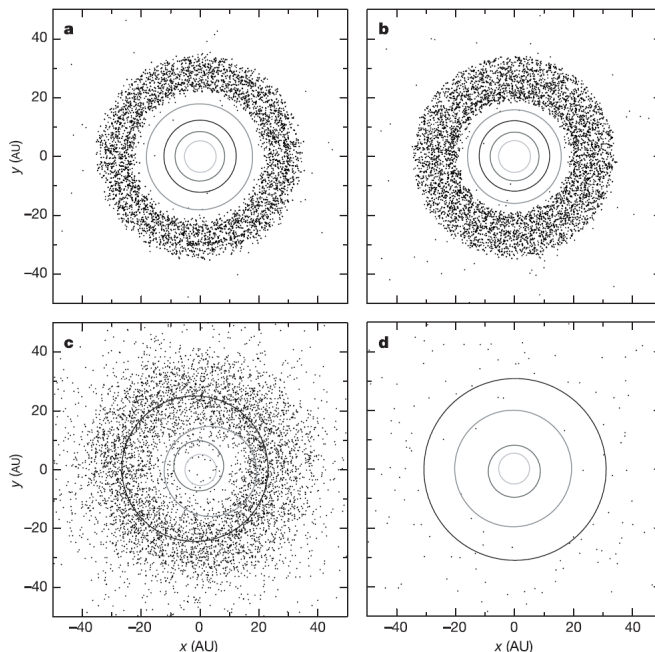
Figure 1.5: The four panels correspond to four different snapshots taken from simulations performed by Gomes et al. (2005). The four giant planets were initially on nearly circular, co-planar orbits with semimajor axes of 5.45, 8.18, 11.5, and 14.2 AU. The dynamically cold planetesimal disk had $35M_{\oplus}$, with an inner edge at 15.5 AU and an outer edge at 34 AU. Each panel represents the state of the planetary system at four different epochs: (a) At a time close to the beginning of the evolution. The orbits of the giant planets (concentric circles) are very close to each other and are quasicircular. They are surrounded by a disk of planetesimals, whose inner edge is due to the perturbations from the planets and the outer edge is assumed to be at 34 AU. (b) Immediately before the great instability. Saturn is approximately crossing the 2:1 resonance with Jupiter. (c) At the time of the instability. Notice that the orbits of the planets have become eccentric and penetrate the planetesimal disk. (d) The planets are parked on orbits very similar (in terms of separation, eccentricity, and inclination) to the current ones. The massive planetesimal disk has been destroyed. Only a small fraction of the planetesimals remain in the system on orbits typical for TNOs. Source: Gomes et al. (2005).

whole region is unstable and can be invaded by objects coming from within the outer boundary of the disk (<34 AU) (Levison et al. 2008). Indeed, it has been shown by

19

Morbidelli (2002) that when Neptune's eccentricity is high, the widths of all its mean motion resonances increase. In particular, numerical experiments of the scattering process show that for eccentricities larger than ~0.15 the MMRs inside the 2:1 MMR overlap one another. Thus, there is literally a chaotic sea that extends outward from the orbit of Neptune to its 2:1 MMR through which particles can freely wander. It is clear from these simulations that the 2:1 MMR provides the boundary to this region. When the eccentricity of Neptune decreases, which takes between ~0.3 and ~4 My, the mechanism that causes this chaos disappears. The Kuiper Belt becomes stable, and the objects that happen to occupy it at that time remain trapped. This mechanism explains the observed dynamically cold population in the Kuiper Belt.

The dynamically hot population is captured later, when Neptune is migrating to its final position in a low-eccentricity orbit. In the Nice model the insertion of the hot population in the belt is similar to how it is described by Gomes (2003). Some of the scattered bodies decouple from the planet's gravity influence, decreasing their eccentricities through interactions with some secular or MMR. If Neptune had not migrated, the decoupled phases would have been transient. In fact, the dynamics are reversible, so that the eccentricity would have eventually increased to Neptune-crossing values. Instead, Neptune's migration brakes the reversibility, and some of the decoupled bodies manage to escape from the resonances, remaining permanently trapped in the Kuiper Belt. This population captured from the scattered disk has a much more extended inclination distribution, for two reasons: (1) the inclinations get excited during the scattered disk phase before capture and (2) there is a dynamical bias in favour of the capture of high-inclination bodies, because at large i the ability of mean-motion resonances to decrease the eccentricity is enhanced.

The Nice model provides a qualitative explanation for the observed correlations between inclination and physical properties. The particles that are trapped in the cold classical belt come, almost exclusively, from the outermost parts of the planetesimal disk, in particular beyond 29 AU. Conversely, a significant fraction of those trapped in the hot population come from the inner disk. Thus, if one assumes that the largest objects could form only in the inner part of the disk, then these objects can only (or predominantly) be found in the hot population. Similarly, if one assumes that, for some unknown reason, the objects from the outer part of the disk are red and those from the inner part are gray, the cold population would be composed almost exclusively of red objects, whereas the hot population would contain a mixture of red and gray bodies (Morbidelli et al. 2008).

The simulations presented by Levison et al. (2008) show that 50 to 130 particles out of 60000 are trapped in the classical belt (cold and hot populations together in roughly equal proportion). According to the Nice model, the original planetesimal disk contained $35 M_\oplus$ and predicts that the classical Kuiper Belt should currently contain between 0.02-0.08$M_\oplus$, in good agreement with observational estimates.

Comparing the observed orbital distribution of TNOs and that obtained from simulations based on the Nice model, it is possible to conclude that the Nice model reproduces the deficit of low-eccentricity objects between 45 and 48 AU together with the outer edge of the classical belt at the final location of the 2:1 MMR with Neptune (Levison et al. 2008). Finally, the Nice model reproduces in a satisfactory way the orbital distributions of the populations in the MMRs with Neptune and the presence of the detached population.

In summary, the strength of the Nice model is that it is able to explain all the intriguing properties of the Kuiper Belt, at least at a semiquantitative level, in the framework of a single, unique event. It also quantitatively reproduces the orbital architecture of the giant planet system (orbital separations, eccentricities, inclinations (Tsiganis et al. 2005)). The main weakness of the Nice model is that the eccentricities in the classical belt are too large. The median eccentricity obtained in the simulations is 0.10-0.13, whereas the observed value is 0.07. Another weakness of the Nice model is the ad-hoc assumption on the color of the cold population without physical reason.

Another strength of the Nice model is that it is able to explain the Late Heavy Bombardment (LHB). The LHB is the event occurred ~700 million years during which a cataclysmic spike in the cratering rate occurred on the Moon, and by inference on the terrestrial planets. In the Nice model the LHB was triggered by the rapid migration of the giant planets which occurred after Jupiter and Saturn crossed their mutual 2:1 MMR. The crossing time range from 350 Myr to 1.1 Gyr, in agreement with the timing of the LHB. The sudden destabilization of the planetesimal disk produces an abrupt spike in the flux of bodies from the outer Solar System entering the region of the terrestrial planets. In addition, the rapid migration of Jupiter and Saturn from their mutual 2:1 MMR to their current position, destabilizes approximately 90% of the asteroids residing in the asteroid belt at the time. Together, outer Solar System planetesimals and escaping asteroids cause a shortlived bombardment on the terrestrial planets lasting $\leq$100 Myr, the magnitude of which is consistent with constraints on the lunar crater rate (Gomes et al. 2005).

1.4   Surface properties of the Transneptunian Objects

In the frame of the origin of the Kuiper Belt described in the previous section, it is clear that TNOs are among the most primitive bodies of the Solar System, and the investigation of their surface composition provides constraints on the evolution of our planetary system.

To determine the surface properties of these remote objects, photometry is the only available technique for the majority of the TNOs, which are extremely faint bodies, with the exception of Pluto that has a brightness of ~13.6 mag. A photometric survey is the natural first step in the investigation of TNOs because it is the only kind of survey capable of providing a global view of the Transneptunian belt. One of the useful physical parameters that can be derived from broadband photometry is the color of the objects, that is the difference between the magnitudes obtained in two different filters. Colors can be used to classify objects into groups. It is also possible to look for statistically significant correlations between colors and other properties of TNOs, like orbital properties (for a review on the color properties of TNOs see (Doressoundiram et al. 2008) or the database compiled by O. Hainaut, www.sc.eso.org/~ohainaut/MBOSS).

However, photometry can provide only limited constraints on the surface composition of the Kuiper Belt population. More detailed information on the composition of TNOs can be acquired from spectroscopic observations in the visible and near-infrared, the most diagnostic wavelength ranges for this task.

In the visible range, TNOs are characterized by mostly featureless spectra with different spectral gradients, ranging from neutral to very red (see Figure 1.6). The spectral gradient S is a measure of the reddening of the reflectance spectrum between two wave-

lengths. It is expressed in percent of reddening per 0.1 μm and is given by

$$S(\lambda_2 > \lambda_1) = (R_{F2,V} - R_{F1,V})/(\lambda_2 - \lambda_1)\,, \tag{1.3}$$

where λ_1 and λ_2 are the central wavelengths of the F1 and F2 filters, respectively. $R_{F,V}$ represents the reflectance of the object in the F filter, after normalizing the spectrum to 1 in the V filter. We have

$$R_{F,V} = 10^{-0.4[(M_F - M_V) - (M_F - M_V)_{\odot}]}\,, \tag{1.4}$$

where M_F (M_V) and $M_{F\,\odot}$ ($M_{V\,\odot}$) represent the magnitude in the filter F (V) of the object and the Sun, respectively (Doressoundiram et al. 2008). By definition, spectral gradient values are a direct measure for the intrinsic reddening of the object produced by the surface properties, indeed the solar colors are removed; hence, $S = 0$ means exactly solar colors (neutral spectral gradient). Red spectral gradient corresponds to $S > 0$.

The existing data show that the visible wavelength emphasizes particularly the "red" objects, whose reflectance increases rapidly with wavelength. Indeed, the red spectral gradient is generally associated to the presence of organic material on the surface of the body, such as tholins, which are the refractory residues of the irradiation of gases and ices containing hydrocarbons (Cruikshank et al. 2005). They are produced in laboratory conditions that are reasonably analogous to the conditions of the exposure of atmospheric gases and surface ices in planetary settings in various natural environments, particularly in the outer Solar System. Different types of tholins have been studied. In particular, the most common are Triton tholin and Titan tholin. They have been obtained irradiating gaseous mixtures of nitrogen (N_2) and methane (CH_4). The initial gaseous mixtures are 99.9%N_2:0.1%CH_4 in case of Triton tholin and 90%N_2:10%CH_4 for Titan tholin (McDonald et al. 1994; de Bergh et al. 2008). The visible range is also important to detect aqueous altered minerals like for example phyllosilicates (Lazzarin et al. 2003; Fornasier et al. 2004a). Fornasier et al. (2004a) detected in the visible spectrum of the TNO 2003 AZ_{84} a very broad and weak absorption band around 0.7 μm. This absorption is very similar to a feature observed on low albedo main belt asteroids and attributed to the action of the aqueous alteration process on minerals. This process has been also claimed as the most plausible explanation for some peculiar visible absorption bands observed on 38628 Huya and 47932 GN_{171} (Lazzarin et al. 2003; de Bergh et al. 2004, Figure 1.7).

The presence of ices and minerals on the surface of TNOs is known from density measurements, which are available for some Transneptunian binaries (Noll et al. 2008). Because of the ice surface composition of TNOs, the near-infrared spectral region (1-2.5) μm has proven to be the most diagnostic wavelength range for the surface characterization of these objects. Indeed ices, such as H_2O and CH_4, have strong absorption bands in this region. Also, TNOs are sufficiently bright in the near-infrared range to allow studies with modern telescopes and spectrometers. L- (centered at ~3.5 μm) and M-band (centered at ~4.5 μm) infrared spectroscopy of distant Solar System objects has great scientific potential as well. Indeed the fundamental vibrational transitions of many ice species are located in this region and the absorptions are much stronger than the ones observed shortwave of 2.5 μm, opening the possibility of detecting additional minority species, as well as better constraining the distributions of known ices. Relatively few observations have been undertaken at wavelengths longer than 2.5 μm because of the weak solar flux, the presence of strong telluric absorptions, and lack of adequate instrumentation.
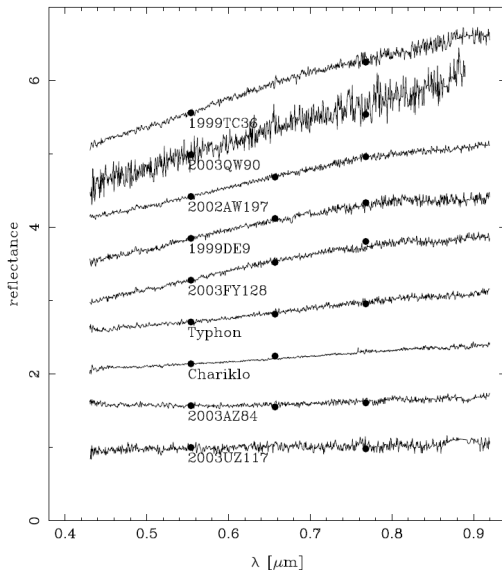
Figure 1.6: Visible reflectance (fraction of incident radiation scattered into many directions by a material, see Section 2.2) spectra of several TNOs (apart Chariklo that is a Centaur). Spectra are shifted vertically by 0.57 for clarity. The spectra gradient S (%(0.1 $\mu m)^{-1}$) varies from 1.5±0.7 (2003UZ$_{117}$) to 37.3±0.7 (1999 TC$_{36}$). Source: Alvarez-Candal et al. (2008).

The analysis of the available TNOs spectra has shown a large difference in the spectral behaviour of these bodies, indicating the presence of four broad groups in the Kuiper Belt (Barucci et al. 2008), which are hereby presented in more detail.

1.4.1   Methane-dominated spectra

Large TNOs with diameter greater than 1300 km present near-infrared spectra dominated by methane ice absorption bands (Brown 2008). Pluto (Olkin et al. 2007), representative of this population, together with Eris (Brown et al. 2005; Licandro et al. 2006a; Dumas et al. 2007; Merlin et al. 2007), Sedna (Barucci et al. 2005), 2005 FY$_9$ [newly named Makemake] (Licandro et al. 2006b; Brown et al. 2007a; Tegler et al. 2007, 2008) and Triton (Quirico et al. 1999), usually thought to be a large TNO captured by Neptune, belong to this category. The only exception is 2003 EL$_{61}$ [newly named Haumea] (Brown et al. 2007b), a large TNO characterized by water ice absorption bands (see next section). Figure 1.8 shows the reflectance spectra of Pluto and 2005 FY$_9$ compared with the synthetic spectrum of CH$_4$. The spectrum of 2005 FY$_9$ is very similar to that of Pluto and both
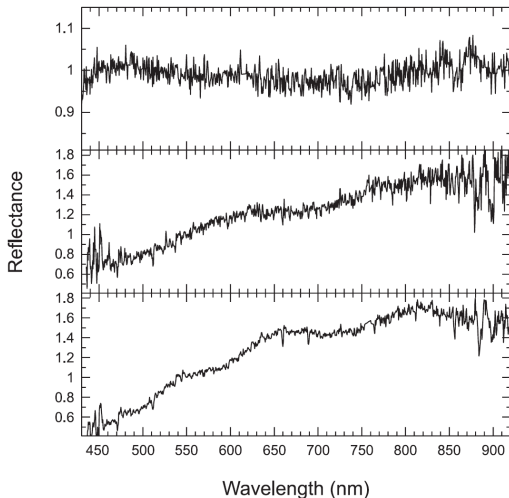
Figure 1.7: Visible spectra of three TNOs showing aqueous alteration bands. From top to bottom, the spectrum of 2003 AZ_{84} (Fornasier et al. 2004a), and the spectra of 47932 GN_{171} and 38628 Huya (Lazzarin et al. 2003) are shown. 2003 AZ_{84} presents an absorption band centered at 700 nm, while 47932 GN_{171} exhibits an absorption feature around 725 nm. 38628 Huya displays two absorptions centered at 600 and 730 nm. Source: Barucci et al. (2008).

present CH_4 absorption bands, deeper in 2005 FY_9 than in Pluto's spectrum. A detailed discussion of the spectra of these large TNOs is given in Section 1.5.1.

1.4.2 Water-ice-dominated spectra

Several TNOs present water ice absorption bands. Charon is considered representative of all KBOs characterized by H_2O absorptions (Cook et al. 2007). All TNOs with spectra showing water ice absorptions measured with sufficiently high signal precision present the 1.65-μm feature linked to the presence of crystalline water ice. Hence, high quality spectra are necessary to distinguish the objects with amorphous water ice, presenting reflectance spectra characterized by the 1.5- and 2.0-μm features, from those presenting the 1.65-μm feature, characteristic for crystalline water ice. Figure 1.9 shows the albedo (quantity directly connected with the reflectance, see Section 2.4) spectrum of Quaoar displaying clearly the absorption band at 1.65 μm characteristic of crystalline water ice.

Crystalline water ice is important for the understanding of the physical processes occurring on TNOs. Several studies have been performed in order to explain how it could be produced at temperatures of 40-50 K and survive in spite of space weathering. Indeed at
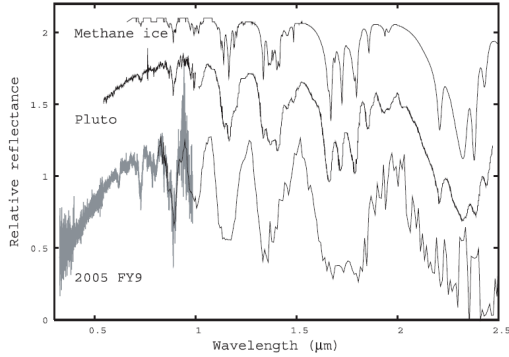
Figure 1.8: Visible (grey) and near-infrared (black) reflectance spectra of 2005 FY$_9$ over the wavelength range (0.4-2.5) μm. The spectrum of Pluto (Grundy and Fink 1996), normalized at 0.6 μm and the spectrum of pure CH_4, both shifted vertically for clarity, are plotted for comparison. Source: Licandro et al. (2006b).
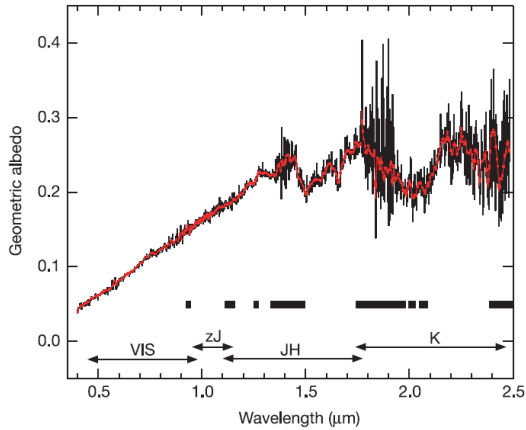
Figure 1.9: The albedo spectrum of Quaoar (Jewitt and Luu 2004) presenting a red optical continuum and distinct absorption bands at 1.5, 1.65, and 2.0 μm. The unsmoothed spectrum is shown as black line. Superimposed in red is a smoothed version of the spectrum. Source: Jewitt and Luu (2004).

these low temperatures, the thermodynamically preferred form of water ice is amorphous (meaning "structureless"). Crystalline ice, with the water molecules arranged in a regular lattice-like pattern, indicates formation temperatures in excess of 110 K, the critical temperature for transformation from amorphous to crystalline. Jewitt and Luu (2004) suggested a possible formation mechanism of crystalline water ice at 50 K: warm ice could be excavated by impact from deeper layers, or blown onto the surface by low-level cryovolcanic outgassing. Another explanation is that the ice on the surface could be heated above 110 K by micrometeorite impact. In addition to the mystery of how crystalline ice is created, there is the question of how it survives. Bombardment by energetic particles from the solar wind and by cosmic rays breaks the bonds between molecules in the crystalline lattice producing amorphous ice. The timescale for the amorphization of crystalline water ice is about 10 My, a short timescale compared to the 4500 My age of the Solar System. This means that whatever process creates crystalline ice, either impact gardening or cryovolcanic outgassing, it must have been active in the immediate past and, indeed, probably still active. A systematic experimental study to investigate the amorphization of crystalline ice by irradiation in the 10-50 K temperature range has been performed by Zheng et al. (2008). It has been found that crystalline water ice can be converted partially to amorphous ice by electron irradiation. Indeed the experiments showed that some of the 1.65-μm band survived the irradiation, to a degree that depends on the temperature, demonstrating that there is a balance between thermal recrystallization and irradiation induced amorphization, with thermal recrystallization dominant at higher temperatures. At 50 K, recrystallization due to thermal effects is strong and most of the crystalline ice survives. This might explain why water ice detected on some KBOs is crystalline in spite of space weathering.

Also the large TNO 2003 EL_{61} (diameter equals to $2000 \times 1500 \times 1000$ km) presents deep water ice absorption bands (Trujillo et al. 2007). Infrared spectroscopy of the satellite revealed in fact the deepest water ice absorption features of any body detected in the outer Solar System (Barkume et al. 2006), which effectively ruled out a capture origin, as capture of a spectrally unique body appears implausible. The rapid rotation, high density, the unusual satellite spectrum, and discovery of a second inner satellite (Brown et al. 2006) strongly point at a collisional origin for this system. A large infrared survey showed that a small number of KBOs have deep water ice absorptions similar to that of 2003 EL_{61} and almost as deep as its satellite. These KBOs are all dynamically clustered near the dynamical position of 2003 EL_{61} itself. According to Brown et al. (2007b), 2003 EL_{61} experienced a giant impact that created its multiple satellite system, stripped away much of an overlying ice mantle, and left it with a rapid rotation.

1.4.3 Water-ice spectra with the presence of methanol-like features

A small number of TNOs show spectra characterized by the 1.5 and 2.0-μm absorptions, which implies the detection of H_2O, together with the 2.27-μm band characteristic of methanol (CH_3OH), or a similar molecule. An example is 55638 2002 VE_{95} (Barucci et al. 2006). This detection indicates a chemically primitive surface, since heating and other processes removed the light hydrocarbons in favour of macromolecular carbon.

As in the case of the 1.65-μm feature of crystalline water ice, the detection of the 2.27-μm band of CH_3OH requires spectroscopic measurements with high signal-to-noise

ratio (∼15). Indeed, many objects show a decreasing slope after 2.2 μm, implying the possible presence of CH_3OH (or a similar molecule), but the low signal precision of the spectroscopic measurements does not allow any firm detection. Nonetheless, the high signal-to-noise ratio in many spectra rules out the presence of this 2.27-μm absorption.

1.4.4 Featureless spectra

Several TNOs present featureless spectra in the near-infrared wavelength range. The featureless appearance is actually due to superficial characteristics or it is due to observational biases. Nonetheless, many spectra have sufficient signal-to-noise to rule out absorptions due to water ice (Barucci et al. 2008).

1.5 Special Transneptunian populations

In this section the two special Transneptunian populations of the largest KBOs and of the binary systems in the Kuiper Belt are described in detail. For more details the reader is referred to the review papers by Brown (2008) and Noll et al. (2008).

1.5.1 Pluto and the large Transneptunian Objects

As anticipated in Section 1.4.1, all TNOs with diameter larger than 1300 km, with the exception of 2003 EL_{61}, present infrared spectra dominated by CH_4 absorption bands. Figure 1.10 shows the visible to infrared spectra of four CH_4 covered objects: Eris, 2005 FY_9, Sedna, and Pluto. In this section the main surface characteristics of the large TNOs are given, focusing the attention on Pluto, the most prominent representative of the large TNOs population and subject of this thesis work.

The first identification of CH_4 ice on Pluto's surface is by Cruikshank et al. (1976). While CH_4 is the most spectroscopically active molecule found in Pluto's spectrum, the detection of N_2 at 2.148 μm, which has an absorption coefficient ∼10^5 less than CH_4, demonstrated that molecular nitrogen is the dominant ice on the surface of the dwarf planet (Owen et al. 1993). Solid nitrogen exhibits two phases: below 35.6 K, the cubic α-phase is stable; above this temperature is the domain of the hexagonal β-phase (de Bergh et al. 2008). The α-phase displays very narrow absorptions, the main ones peaking at 2.148 μm and in the range between 4.15 and 4.30 μm, requiring high spectral resolution and signal-to-noise ratio for detection, while the β-phase has broad bands around 2.15, 4.18, and 4.29 μm. The spectral shape of the bands can be used as a surface thermometer (Grundy et al. 1993). The analysis of the profile of the 2.15-μm band of nitrogen led Tryka et al. (1994) to propose a value of 40±2 K for the temperature of nitrogen ice on Pluto.

Several important issues have emerged from the quantitative modeling of Pluto's spectrum (Cruikshank et al. 1993). The first concerns the state of CH_4 ice on Pluto's surface (Douté et al. 1999). Seen at high spectral resolution, the CH_4 bands in Pluto's spectrum are shifted toward shorter wavelengths compared to the central wavelengths of pure CH_4 obtained in the laboratory. This shift, discovered by Schmitt and Quirico (1992), occurs when CH_4 is dissolved at low concentrations in a matrix of solid N_2, and the magnitude of the shift varies from one CH_4 band to another. In particular, the complex structure of
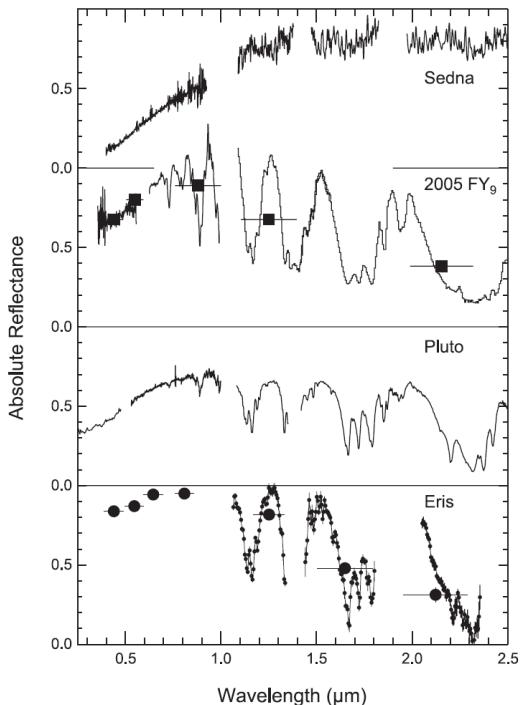
Figure 1.10: The reflectance spectra of Sedna, 2005 FY$_9$, Pluto, and Eris, four large TNOs characterized by volatile-rich surface composition along the wavelength range between 0.4 and 2.5 μm. Source: Brown (2008).

the CH$_4$ bands in Pluto's spectrum indicates that there are two components contributing to the absorption. One component is formed by CH$_4$ dissolved in N$_2$, with shifted wavelengths as described above, and another arising from pure CH$_4$ without the wavelength shifts. Indeed, using the laboratory data of Quirico and Schmitt (1997b), Douté et al. (1999) compared the methane bands in the Pluto spectra with those of pure solid methane around 40 K and those of CH$_4$ diluted in solid β-N$_2$ around the same temperature. It has been found that the absorption band visible in all the observations around 1.69 μm (see Figure 1.11) is related to pure solid methane. Indeed, this band has never been observed in any sample of CH$_4$ diluted in N$_2$ (neither in α- or β-N$_2$ phases) at any temperature. This band is clearly a witness of the presence of pure methane at the surface of Pluto. Solid CO is also identified on Pluto by the detection of the band at 2.35 μm and the weaker band at 1.58 μm. From thermodynamic considerations and observations of the band at
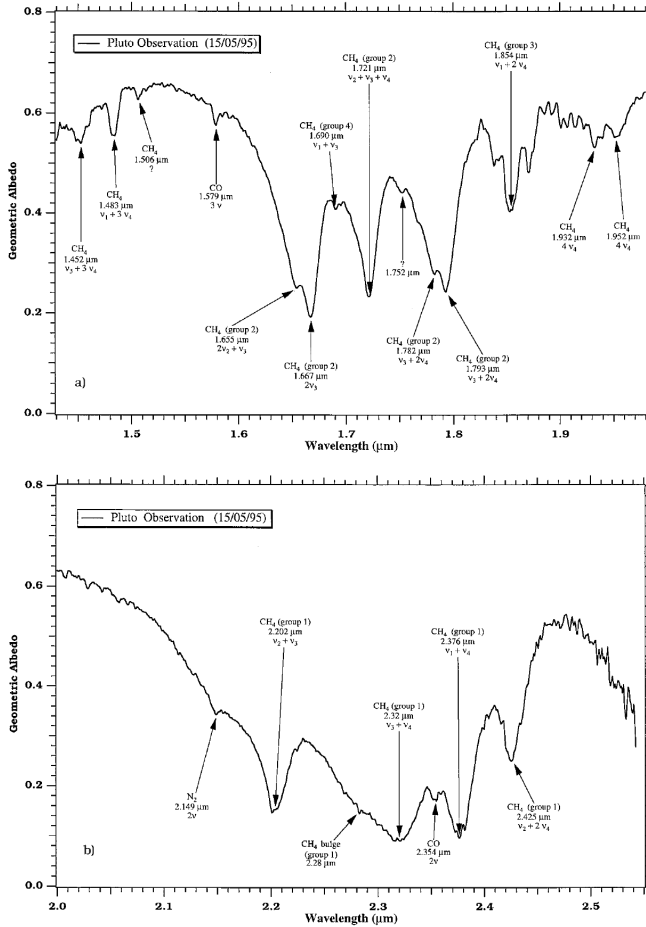
Figure 1.11: The infrared spectrum of Pluto obtained by Douté et al. (1999) in H- (top panel) and K- (bottom panel) bands with the identification of the ice absorption bands. Source: Douté et al. (1999).

2.35 μm, CO is thought to be dissolved as a minor constituent in Pluto's N_2 ice (Quirico and Schmitt 1997a; Douté et al. 1999). The other obvious spectral feature on Pluto is the red slope in the visible region of the spectrum (see Figure 1.8) (Grundy and Fink 1996). All of the ices described above are essentially transparent in the visible, so an additional

absorber is required. A persistent hypothesis for the reddening agent on the surface is the existence of tholin compounds (Brown 2002, Section 1.4).

Like Pluto, the infrared spectra of Eris and 2005 FY_9 are dominated by CH_4 absorptions (see Figure 1.10). However, the infrared spectra of both objects show no evidence for the small wavelength shifts of the CH_4 absorption bands associated with CH_4 being dissolved in N_2 ice. Compared to Pluto and Eris, 2005 FY_9 presents significantly deeper and broader CH_4 absorption features. The depth and breadth of solid-state absorption features is a function of optical path length through the absorbing material, so the features on 2005 FY_9 can be interpreted as being due to extremely large (~1 cm) methane grains on 2005 FY_9 (Brown 2008). Unlike Pluto, the moderately high signal-to-noise spectrum of 2005 FY_9 shows no evidence for the presence of the 2.15-μm N_2 absorption feature (Brown et al. 2007a). The N_2 absorption feature has also not been identified on the surface spectra of Eris. However, the detection may be extremely difficult because of the expected α form of N_2 on the surface of Eris that makes the absorption even weaker than that of the β form observed on Pluto (Grundy et al. 1993). Visible spectroscopy of Eris (Licandro et al. 2006a; Dumas et al. 2007) and 2005 FY_9 (Tegler et al. 2007, 2008) shows evidence for slight shifts in the wavelengths of the methane absorption features that could be indicative of a small amount of surface coverage of methane dissolved in nitrogen. In the case of Eris, Licandro et al. (2006a) consider the possibility that methane and nitrogen are layered, with decreasing nitrogen abundance with increasing depth (see Section 3.4). Finally, 2005 FY_9 shows a clear signature for the presence of small grains of ethane, in addition to those of methane (Brown et al. 2007a). Ethane is one of the expected dissociation products of both gaseous- and solid-state methane. Like Pluto, Eris, and 2005 FY_9, the moderate signal-to-noise ratio spectrum of Sedna, one of the reddest KBOs, appears to contain methane and perhaps nitrogen (Barucci et al. 2005).

1.5.1.1 Volatile loss and retention on Transneptunian Objects

The transition from small objects with volatile-free surfaces (such as Charon or Quaoar, see Section 1.4) to large objects with volatile-rich ones (such as Pluto) can be explained with a simple model of atmospheric escape formulated by Schaller and Brown (2007a). This model allows us to predict which bodies should be capable of retaining which surface volatile ices to the present day. In particular, Schaller and Brown (2007a) calculated for a body of given size and surface temperature the minimum total volatile loss from Jeans escape over the age of the Solar System assuming all volatiles (CH_4, CO, N_2) located at the surface. For a surface in radiative equilibrium, the Jeans escape flux of CH_4, CO, N_2 from a body with radius R has been modeled in the following way

$$\frac{dM_{vol}}{dt} = 4\pi R^2 \frac{P_{vap}(T)}{2\sqrt{\pi}kT} \sqrt{\frac{2kT}{m}}(1+\lambda)e^{-\lambda} , \qquad (1.5)$$

where

$$\lambda = \frac{GMm}{kTR} . \qquad (1.6)$$

In eq. (1.5), $\frac{dM_{vol}}{dt}$ is the rate of loss of a given volatile in molecules per second, $P_{vap}(T)$ is the vapour pressure of a given volatile compound at the radiative equilibrium temperature T, k is the Boltzmann constant, m is the molecular mass of a given volatile species, G is
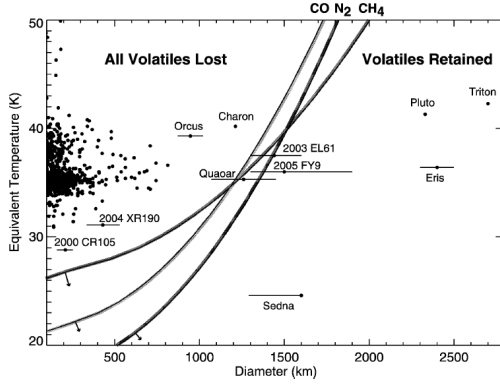
Figure 1.12: Minimum volatile loss in the outer Solar System as a function of temperature and diameter. The lines show the temperatures as a function of diameter at which the initial inventories of CH_4, N_2, and CO are lost over the age of the Solar System. Source: Schaller and Brown (2007a).

the gravitational constant, and M is the mass of the body. Figure 1.12 shows the minimum volatile loss in the outer Solar System as a function of temperature and diameter. It has been assumed by Schaller and Brown (2007a) that all bodies began as volatile-rich, high-albedo objects similar to Pluto with all volatiles at the surface equilibrium temperature and accessible to the surface. For each of the known KBOs, the volatile loss has been calculated by dividing the object's orbit into small segments and integrating the total loss of volatile over the age of the Solar System. Finally, the total mass loss has been translated into a volatile loss equivalent temperature corresponding to the temperature of a body with identical mass in a circular orbit that would have experienced the same loss over the age of the Solar System. The equivalent volatile loss temperature for most bodies is very close to the perihelion temperature since most of the loss occurs near perihelion. However, for objects with extremely eccentric orbits the equivalent temperature can be somewhat lower.

The model formulated by Schaller and Brown (2007a) predicts the presence of three TNOs categories: most KBOs are too small and too hot to be able to retain volatiles against atmospheric escape over the life of the Solar System; a few objects, however, are so large or so cold that they easily retain volatiles, and a small number of them are in the potential transition region between volatile-free and volatile-rich surfaces. The first two categories predicted by the atmospheric escape model perfectly reflect measured KBO surface compositions (see Section 1.4). Three objects 2003 EL$_{61}$, Quaoar, and 2005 FY$_9$ appear to be close the transition region between possible volatile retention and volatile loss. In particular, 2003 EL$_{61}$ is sufficiently large that it could retain volatiles, but it seems likely that the hypothesized giant impact that could have removed much of its water ice, would have removed much of the volatile mass as well, either through direct ejection or

31

heating (Brown et al. 2006). 2005 FY_9 and Quaoar are both sufficiently hot that the low-vapour-pressure nitrogen should all have escaped, but the lower-vapour-pressure methane could still be retained. This depletion of nitrogen relative to methane is precisely what is observed on 2005 FY_9. Quaoar has a water ice dominated spectrum with an additional absorption feature at 2.2 μm. The feature, that was previously interpreted as an absorption due to non-volatile ammonia ices by Jewitt and Luu (2004), has recently been clearly attributed to methane by Schaller and Brown (2007b), in agreement with Quaoar being an object that may still retain some initial volatiles.

To summarize, atmospheric escape appears to provide a first-order explanation of the range of surface spectra seen on bodies in the outer Solar System. It reproduces the existence of volatile-rich objects, the lack of volatiles on most Kuiper Belt objects, and even the peculiar surface TNOs.

1.5.2 Transneptunian binaries

The discovery of binaries among the population of TNOs is a landmark advance in the study of this remote region of the Solar System. The characterization of binary orbits enables direct determination of system masses, fundamental for the calculation of density, internal structure, and bulk composition. The first discovery of Transneptunian binary (TNB) occurred with the identification of Charon, Pluto's moon, by Christy and Harrington (1978). This is the first example of a binary system, that means two objects orbiting a barycenter located outside the two components (Noll et al. 2008). Recently two additional moons of Pluto, Nix and Hydra, have been discovered (Weaver et al. 2006). Less than a decade after the detection of 1992 QB_1, Veillet et al. (2001) announced the discovery of a second TNB, a companion to 1998 WW_{31}. This discovery provided immediately a context for Pluto/Charon as a member of a group of similar systems rather than as a peculiar body in the Transneptunian region. Successive discoveries have followed rapidly so that 48 binary or multiple systems are now known, like (80806) 2000 CM_{105}, 2000 OJ_{67}, (79360) 1997 CS_{29} (Stephens and Noll 2006).

As mentioned above, a particularly valuable information that can be derived from the mutual orbit of a binary system is the total mass, M_{sys}, according to the Kepler's third law. The critical derived quantity M_{sys} depends on the cube of the semimajor axis a and the square of the period T, both quantities known from positional information. Once this parameter is known, it is possible to determine other important physical parameters such as the bulk volume, the individual radii of the primary and secondary components, and the geometric albedo of the system.

Determining the surface composition of TNBs is fundamental for the understanding of the origin and evolution of the outer Solar System. Indeed, differences in color or surface composition could be due either to mixing of different composition populations in the protoplanetary disk before the bound systems were formed or different collisional and evolutionary histories of components after they were bound. It has been found that the components of the analysed systems have colors that are consistent with each other within the uncertainties of the measurements. This similarity could imply that they are composed of similar material at least on the surface. However, as discussed in Section 1.4, spectroscopic measurements are more diagnostic for the composition than color data. Separate spectra of binary components are available for the Pluto/Charon system and for

2003 EL$_{61}$ (Barkume et al. 2006) only. In the case of Pluto/Charon, mutual events allowed to distinguish the surface composition of the dwarf planet and its moon by comparing reflectance spectra of the two objects blended together with spectra of Pluto alone, when Charon was completely hidden from view (Buie et al. 1987; Young et al. 1999). Observations performed by Brown and Calvin (2000) and Buie and Grundy (2000) without the aid of mutual events, have resolved the satellite Charon from Pluto, giving separate spectra of the two objects from 1.0 to 2.5 μm, revealing the well-known spectral differences between Pluto and Charon (see Section 1.4). As discussed in Section 1.5.1.1, this spectral difference is primarily related to the size threshold for retaining the very volatile CH$_4$, CO, and N$_2$ ices found on Pluto and not on Charon. Both 2003 EL$_{61}$ and its large satellite, by contrast, have spectra that are dominated by water ice (see Section 1.4.2).

Capture and/or collisions are the models that have been best exploited to explain the formation of TNBs. Goldreich et al. (2002) offer a scenario in which two large bodies penetrate one another's Hill sphere. The loss of energy needed to stabilize the binary orbit can occur either through dynamical friction from surrounding small bodies or through the gravitational scattering of a third large body. This dynamical capture is a possible formation scenario for most known TNBs. The small satellites of the largest Transneptunian objects, in contrast, are more likely formed from collisions. This is the case of Pluto's satellites, Nix and Hydra, (Stern et al. 2006) and the small satellites of 2003 EL$_{61}$ and Eris (Noll et al. 2008).

1.6   Perspectives: New Horizons-NASA's Pluto-Kuiper Belt Mission

The discovery of large TNOs (see Section 1.5.1), multiple systems (Section 1.5.2) and Plutinos (see Section 1.1) has emphasized that Pluto is not the smallest, most peculiar planet of the Solar System moving on the most eccentric and most inclined orbit, but instead is a rather typical KBO. This is the reason why Pluto is the target of New Horizons (NH), the first mission to explore the world of an ice dwarf planet in the Solar System. NH had a successful launch on January 19, 2006 and will encounter the Pluto/Charon system in July 2015. If NASA approves an extended mission phase, the NH spacecraft will be targeted toward flyby encounters at one or more small (~50 km diameter) KBOs after the Pluto flyby.

The primary science goals for which the NH mission has been designed are: 1) characterization of the global geology and morphology of Pluto and Charon; 2) mapping the surface composition of Pluto and Charon; 3) characterizing the neutral atmosphere of Pluto and its escape rate. For more details on the scientific investigations that the NH science team intends to perform at the Pluto system, the reader is referred to the paper by Young et al. (2008).

The NH science payload includes seven instruments:

- ALICE: Ultraviolet imaging spectrometer; analyses composition and structure of Pluto's atmosphere and looks for atmospheres around Charon and KBOs.

- LORRI: (Long Range Reconnaissance Imager) Telescopic camera; obtains encounter data at long distances, maps Pluto's farside, and provides high resolution geologic
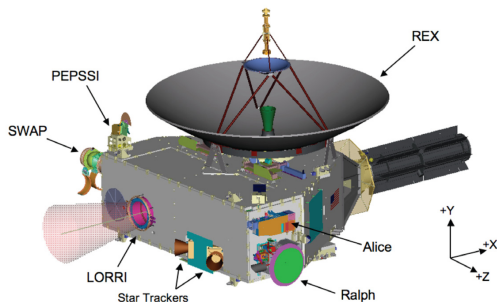
Figure 1.13: This drawing shows the locations of the instruments on the New Horizons spacecraft. Source: Weaver et al. (2008).

data.

- PEPSSI: (Pluto Energetic Particle Spectrometer Science Investigation) Energetic particle spectrometer; measures the composition and density of plasma (ions) escaping from Pluto's atmosphere.

- RALPH: Visible and infrared imager/spectrometer; provides color, composition and thermal maps.

- REX: (Radio Science EXperiment) Passive radiometer; measures atmospheric composition and temperature.

- SDC: (Student Dust Counter) Built and operated by students; measures the space dust peppering NH during its voyage across the Solar System.

- SWAP: (Solar Wind Around Pluto) Solar wind and plasma spectrometer; measures atmospheric "escape rate" and observes Pluto's interaction with solar wind.

The best suited instrument for the characterization of the surface composition of Pluto and Charon is the infrared spectral imager Ralph-LEISA (Linear Etalon Imaging Spectral Array). This instrument will map the distributions of N_2, CO, CH_4, and H_2O, as well as other species yet to be discovered, on the sunlit surfaces of Pluto and Charon at a best resolution of 10 km/pixel. Spatially resolved spectra will allow a more sensitive search for additional surface species. On Pluto, for example, exposed H_2O ice can be more easily identified without the interference of CH_4 bands (Grundy et al. 2002b). On Charon, NH_3 may be confirmed in spatially resolved spectra by the detection of the 1.99-μm band of NH_3, which may be suppressed by the presence of the broad H_2O band at 2.0 μm at disk-averaged spectra of terrestrial telescopes (Buie and Grundy 2000). Ralph-LEISA is an infrared spectral imager covering the wavelength range between 1.25 and 2.5 μm with a spectral resolution of ~250. A higher resolution of ~550 in the range 2.10-2.25 μm will be

used to discern between pure vs solid-solution abundances but also for taking advantage of the temperature sensitive N_2 bands (see Section 1.5.1). Long wavelength region (L- and M-bands) is not covered by LEISA nor another NH instrument.

1.7   Motivation and Goals of the Thesis

The topics presented in the previous sections intend to highlight the importance of TNOs as "fossil remnants" of the formation of our planetary system. We focused in particular on the characterization of the surface composition of these objects, in order to show the importance of visible and infrared spectroscopy as a tool to better understand the formation and evolution of this population. Studies of the physical properties of these objects are still limited by their faintness, and particularly lacking is the information on the compositional properties of their surfaces.

The work presented in this thesis intends to characterize with high accuracy the spectral properties of two TNO binaries: Pluto/Charon and (47171) 1999 TC$_{36}$. Both are multiple systems in MMR with Neptune 3:2. We intend to quantify the nature and properties of the compounds present on the surface of our targets by applying a Hapke radiative transfer model to spectra measured at the ESO Very Large Telescope, the 8.2 m telescope in Paranal, Chile, that guarantees high quality measurements.

In the case of Pluto/Charon, we aim at resolving the binary system and to obtain, for the first time, spectra up to 5 μm and 4 μm for Pluto and Charon, respectively. Extending the wavelength coverage of the surface spectroscopy beyond the K-band (2.5 μm) gives the possibility:

- To detect further surface ice absorption bands predicted from the models that are based on the available JHK spectra.

- To search for signatures of yet unknown ices.

- To support and complement NASA's Pluto-Kuiper Belt Mission (NH), exploring wavelengths not accessible to it.

- To obtain more information on the family of large TNOs as a whole.

- To quantify the contribution of Charon to the unresolved Pluto/Charon system.

- To compute a standard spectroscopic model for Charon that can be used to subtract Charon light from ground-based spectra of the combined Pluto/Charon system up to 4 μm.

Regarding (47171) 1999 TC$_{36}$, we intend to obtain spectroscopic measurements in the visible and near-infrared wavelength range with an higher signal-to-noise ratio with respect to previous measurements. This would allow us

- To detect and quantify the ice compounds present on the surface.

- To search for signatures of hydrated minerals.

- To compare these observations with previous ones in order to investigate the surface homogeneity of the target.

The investigated objects give also the possibility to compare surface properties of TNOs belonging to the same dynamical group. This allows a better understanding of the correlation between surface composition and dynamical properties.

2 Quantitative modeling of the spectral reflectance of Transneptunian Objects

2.1 Introduction

Several methods have been developed to calculate synthetic reflectance spectra for comparison with the spectroscopic observational data of Solar System bodies. The objective of such modeling is to determine the composition (ices, minerals, organic solids), the type of mixture (intimate, areal), the relative abundance of the components together with their grain sizes, and the approximate surface characteristics (e.g. mean roughness slope, compaction parameter) of the layer that reflects or scatters the incident sunlight in the visible and near-infrared. Real planetary surfaces are composed of different elements. Obtaining the single elements abundance from a reflectance spectrum in an unambiguous way is a difficult task since the spectra are complex nonlinear functions of several physical parameters, such as grain size and abundance. Multiple scattering models can provide approximate solutions to the radiative transfer in a particulate medium.

The scattering theories of Hapke (1981, 1993) and Shkuratov et al. (1999) are the most widely used for modeling the reflectance spectra and color data of Kuiper Belt objects, Centaurs, and other bodies in the Solar System. These models, which are based on geometric optics, are applicable in the visible and near-infrared regions of the spectrum because the typical size range of the components of planetary regolith are significantly larger (tens of micrometers) than the considered wavelengths. The main difference between the two approaches is the role of the phase function of individual particles of regolith (see Section 2.2.1), which is predicted in the case of the Shkuratov model instead of being a free parameter as formulated in the Hapke model (Poulet et al. 2002). In order to compare the two theories, the modeling of the visible and near-infrared reflectance spectra of several targets has been obtained using both of them. In several cases both theories yield good models of the reflectance spectrum of the target, although the derived abundances differ significantly (Poulet et al. 2002; Cruikshank et al. 2003; Barucci et al. 2008). Figure 2.1 presents as example the case of the Plutino 55638 2002 VE$_{95}$. Both models give a satisfactory fit, although the retrieved information about the surface composition of the target are not in agreement (Barucci et al. 2006).

In this thesis the Hapke radiative transfer model has been used with the goal to retrieve information about the surface composition of Pluto, Charon and (47171) 1999 TC$_{36}$, three different examples of Transneptunian Objects (TNOs). The choice of using Hapke (1993)
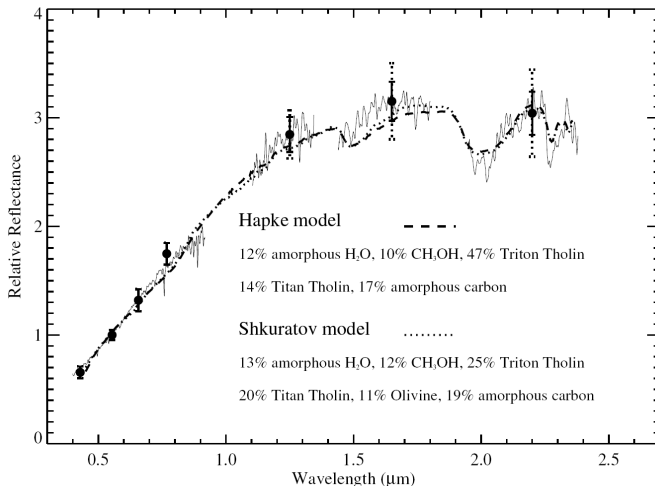
Figure 2.1: Spectral reflectance of 55638 2002 VE$_{95}$ obtained in V, J, H, and K ranges (solid line) and adjusted using photometric colors, which are represented by dots with the relative errors. The obtained intimate models (dashed and dotted lines, according to the legend) have also been reported. Source: Barucci et al. (2006).

instead of Shkuratov et al. (1999) theory is based on the fact that the surface composition of the targets analysed in this thesis have been investigated by other studies using Hapke theory (Olkin et al. 2007; Buie and Grundy 2000; Dotto et al. 2003). Since one of the goals of the presented work is to look for possible temporal changes of the surface composition of the considered TNOs, it is fundamental to use the same modeling approach as previous studies, in order to perform a consistent comparison between the time dependent modeling outputs.

The purpose of this chapter is to describe the radiative transfer algorithm used in this work for the quantitative analysis of the reflectance spectra of the considered TNOs.

2.2   Reflectance spectroscopy: Hapke Theory

Hapke's model is based on a two-stream approximation to the equations of radiative transfer, and enables the calculation of the reflectance of a particulate surface, knowing the physical nature of the surface elements (Hapke 1993). The term *reflectance* refers to the fraction of incident radiation scattered into many directions by a material. There are several kinds of reflectance according to the degree of collimation of the source and the detector (or observer, in case for example of ground based observations). Generally the term *reflectance* is preceded by two adjectives, the first describing the degree of collima-

tion of the source and the second that of the detector. The usual adjectives are *directional*, *conical*, or *hemispherical*. For example, the *directional hemispherical reflectance* is the total fraction of radiation scattered into the upward hemisphere by a surface illuminated from above by a highly collimated source. In this chapter we will consider *bidirectional reflectance* (r) only, that is the total fraction of radiation scattered into a single direction by a surface illuminated from above by a highly collimated source. The bidirectional reflectance is a physically idealized concept. In reality, the solid angles for both collimated source and detector are finite, and what we can measure is actually biconical reflectance. However, in most cases of remote sensing, both the angular sizes of source and detector are very small as seen from the object. The bidirectional reflectance is therefore a good approximation, and an important simplification in theoretical analysis. Spectral modeling of several TNOs has been usually performed considering the bidirectional reflectance approximation, for example in the case of Pluto (Douté et al. 1999), Charon (Roush 1994), Pholus (Cruikshank et al. 2003), Quaoar (Schaller and Brown 2007b).

The geometry is illustrated schematically in Figure 2.2. A plane surface $z = 0$ separates an empty half-space $z > 0$ from a half-space $z < 0$ containing irregular, randomly oriented, absorbing particles which are large compared with the incident wavelength. The medium is illuminated by collimated irradiance J travelling into a direction Ω_0, at an angle $\pi - i$ with respect to the upward z-direction, and has an azimuth angle $\phi = 0$; that is, the incident radiation is coming from a direction which makes an angle $\theta = i$ with the z-axis. The medium is observed by a detector with sensitive area Δa, which accepts radiation within a solid angle $\Delta\omega$ about a direction Ω_D making an angle $\theta = e$ with the z-axis, with azimuth angle $\phi = \psi$. The radiance at the detector comes from radiation scattered or emitted by all the particles in the medium within the detector field of view $\Delta\omega$. The angle between the directions to the source and detector as seen from the surface is the phase angle g. Let

$$\mu = cos\,e\,,\tag{2.1}$$

$$\mu_0 = cos\,i\,.\tag{2.2}$$

In general, three angles are needed to specify the geometry. The angles usually used in planetary applications are i, e, and g.

Let us consider a volume element $dV = R^2\Delta\omega dR$ located within $\Delta\omega$ at an altitude z in the medium and a distance R from the detector. The volume element dV is illuminated by both the collimated incident irradiance J attenuated by extinction by the particles between the source and dV, and by diffuse radiance[1] $I(z, \Omega')$ travelling within the solid angle $d\Omega'$ which has been scattered one or more times by other particles. Thus, the amount of power scattered by the particles in dV into unit solid angle about the direction Ω_D between dV and the detector, is given by

$$\frac{dV}{4\pi}\int_{4\pi} G(z, \Omega', \Omega_D)I(z, \Omega')d\Omega'\,,\tag{2.3}$$

---

[1]In a radiation field where the radiation is uncollimated, the power at position **r** crossing unit area perpendicular to the direction of propagation Ω, travelling into unit solid angle about Ω, is called *radiance* and will be denoted by $I(\mathbf{r}, \Omega)$. Note the difference between irradiance J, which refers to power per unit area of a collimated beam, and radiance I, which is uncollimated power per unit area per unit solid angle. The irradiance may be considered to be the limit of a highly collimated radiance, $J(\mathbf{r}, \Omega_0) = I(\mathbf{r}, \Omega)\delta(\Omega - \Omega_0)$.
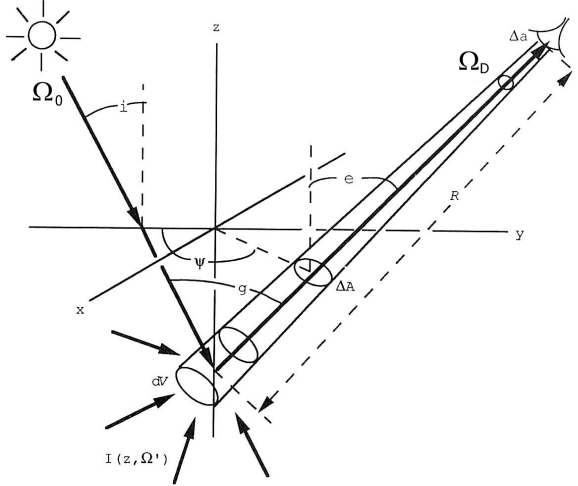
Figure 2.2: Geometry of scattering from within a particulate medium. Adapted from Hapke (1993).

where $G(z, \Omega', \Omega_D)$ is the *volume angular scattering coefficient* of the medium, which represents the probability that a photon travelling in direction Ω' will be scattered in direction Ω_D. The volume angular scattering coefficient of the medium is defined such that the power ΔP_S passing through the volume element dV into a cone of solid angle $d\Omega'$ about direction Ω' that is scattered into a cone $d\Omega$ about direction Ω is $\Delta P_s = \frac{1}{4\pi} G(z, \Omega', \Omega) I(z, \Omega') dV d\Omega' d\Omega$.

In addition, an amount of power

$$F(z, \Omega_D) dV \qquad (2.4)$$

is emitted from dV per unit solid angle toward the detector, where $F(z, \Omega_D)$ is the *volume emission coefficient*, defined as the power emitted per unit volume by the element at position z into unit solid angle about direction Ω_D. There are at least four processes that may contribute to the volume emission: single scattering, thermal emission, fluorescence and luminescence, and stimulated emission. Fluorescence and luminescence will not be considered further in this chapter. Stimulated emission is important in gaseous media that are not in thermodynamic equilibrium, but not in particulate media. Thermal emission in the case of TNOs ($T \sim 40K$) has its maximum flux around 70 μm, and in the wavelength range analysed in this thesis work, (0.4-5.0) μm, its contribution is completely negligible. Hence, only single scattering will be considered as responsible for the emission process;

its volume coefficient will be denoted by $F_S(z, \Omega_D)$. Then

$$F(z, \Omega_D) = F_S(z, \Omega_D) \,. \tag{2.5}$$

As mentioned before, the irradiance that illuminates the medium is attenuated by extinction by the particles between the source and dV, hence the irradiance emitted by the source reaching the volume element dV is

$$J \, \delta(\Omega' - \Omega_0) \, \exp[- \int_{\tilde{s}'}^{\tilde{s}'} E(s', \Omega')ds'] \,, \tag{2.6}$$

where ds' is the length element along the direction Ω_0 and $\tilde{s}'$ and $\overline{s}'$ are the position of the source and of the volume element dV, respectively (the intersection of Ω_0 with the plane xy has been chosen as origin). In the previous relation δ is the Dirac function and E is the *volume extinction coefficient* of the medium. E is defined such that the decrease in power ΔP_E due to extinction as the beam propagates through the volume element dV is $\Delta P_E = -E(z, \Omega)I(z, \Omega)dVd\Omega$. The extinction coefficient includes any process which removes photons from the beam of radiation and includes both scattering and absorption so that $E(z, \Omega) = S(z, \Omega) + K(z, \Omega)$, where $K(z, \Omega)$ is the *volume absorption coefficient* and $S(z, \Omega)$ the *volume scattering coefficient*. According to what has been discussed above, we have the following relation for $F_S(z, \Omega_D)$

$$
\begin{aligned}
F_S(z, \Omega_D) &= \frac{1}{4\pi} \int_{4\pi} J\delta(\Omega' - \Omega_0) \exp\left[- \int_{\tilde{s}'}^{\tilde{s}'} E(s', \Omega')ds'\right] G(z, \Omega', \Omega_D)d\Omega' = \\
&= \frac{1}{4\pi} JG(z, \Omega_0, \Omega_D) \exp\left[- \int_{\tilde{s}'}^{\tilde{s}'} E(s', \Omega_0)ds'\right] \,.
\end{aligned}
\tag{2.7}
$$

The radiance scattered and emitted from dV toward the detector is attenuated by extinction due to the particles between dV and the detector, before emerging from the medium, by a factor $e^{-\tau/\mu}$, where τ is the optical depth of the volume element dV, defined as $d\tau = -E(z)dz$. Hence, the power from dV reaching the detector is

$$dP_D = \left[\frac{1}{4\pi} \int_{4\pi} G(z, \Omega', \Omega_D)I(z, \Omega')d\Omega' + F_S(z, \Omega_D)\right] \Delta\omega \frac{dz}{\mu} \Delta a \, e^{-\frac{\tau}{\mu}} \,, \tag{2.8}$$

where we have put $dz = \mu dR$ (dR is the length element along the direction Ω_D). The previous relation can be written in the following way

$$dP_D = -\Delta\omega\Delta a \left[\frac{w(\tau)}{4\pi} \int_{4\pi} P(\tau, \Omega', \Omega_D)I(\tau, \Omega')d\Omega' + \mathcal{F}(\tau, \Omega_D)\right] e^{-\frac{\tau}{\mu}} \frac{d\tau}{\mu} \,, \tag{2.9}$$

where

$$P(z, \Omega', \Omega_D) = \frac{G(z, \Omega', \Omega_D)}{S(z)} \,, \tag{2.10}$$

$$w(z) = \frac{S(z)}{E(z)} \,, \tag{2.11}$$

and

$$\mathcal{F}(z, \Omega_D) = \frac{F_S(z, \Omega_D)}{E(z)} = \frac{1}{4\pi} J w(\tau) P(\tau, \Omega_0, \Omega_D) e^{-\frac{\tau}{\mu_0}} \quad (2.12)$$

are *volume phase function*, *volume single-scattering albedo*, and *source function*, respectively.

The total power reaching the detector is the integral of dP_D over all volume elements within $\Delta\omega$ between $z = -\infty$ and $z = \infty$, or, equivalently, between $\tau = \infty$ and $\tau = 0$ (in correspondence of $z \geq 0$ is $\tau = 0$). The radiance I_D at the detector is the power per unit area per unit solid angle. Thus

$$I_D = \frac{1}{\Delta\omega\Delta a} \int_{z=-\infty}^{\infty} dP_D =$$

$$= \int_0^{\infty} \left[\frac{w(\tau)}{4\pi} \int_{4\pi} P(\tau, \Omega', \Omega_D) I(\tau, \Omega') d\Omega' + \mathcal{F}(\tau, \Omega_D) \right] e^{-\frac{\tau}{\mu}} \frac{d\tau}{\mu} .$$

$$(2.13)$$

The radiance reaching the detector can be written in the following way

$$I_D = I_{Ds} + I_{Dm} , \quad (2.14)$$

where I_{Ds} is the *singly scattered radiance*

$$I_{Ds} = \int_0^{\infty} \mathcal{F}(\tau, \Omega_D) e^{-\frac{\tau}{\mu}} \frac{d\tau}{\mu} , \quad (2.15)$$

and I_{Dm} is the *multiply scattered radiance*

$$I_{Dm} = \int_0^{\infty} \frac{w(\tau)}{4\pi} \int_{4\pi} P(\tau, \Omega', \Omega_D) I(\tau, \Omega') d\Omega' e^{-\frac{\tau}{\mu}} \frac{d\tau}{\mu} . \quad (2.16)$$

Assuming w and P are independent from z or τ, as it is often the case, the singly scattered radiance can be evaluated for any arbitrary phase function, obtaining

$$I_{Ds} = \frac{J}{4\pi} \frac{1}{\mu} w P(\Omega_0, \Omega_D) \int_0^{\infty} e^{-\frac{\tau}{\mu_0}} e^{-\frac{\tau}{\mu}} d\tau , \quad (2.17)$$

where eq. (2.12) has been taken into account. The total radiance reaching the detector due to single scattering I_{Ds} is then

$$I_{Ds} = J \frac{w}{4\pi} \frac{\mu_0}{\mu + \mu_0} P(g) . \quad (2.18)$$

Therefore, I_{Ds} represents the contribution to the radiance at the detector of a semiinfinite, particulate medium by radiation that has been scattered only once. When $P(g) = 1$, that is, when the scatterers are isotropic, eq. (2.18) is the *Lommel-Seeliger law*. Except close to zero phase, this expression is a good description of the radiation scattered by low-albedo

bodies of the Solar System, such as the Moon and Mercury, for which only radiation that has been scattered once contributes significantly to the radiance at the detector.

To evaluate I_{Dm}, the two stream approximation for isotropic scattering is used to solve the equation of radiative transfer (see Appendix A for details). If thermal emission is negligible, the contribution of multiple scattering from isotropic scatterers is

$$I_{Dm} = \frac{Jw}{4\pi} \frac{\mu_0}{\mu + \mu_0} \left[H(\mu)H(\mu_0) - 1\right] , \qquad (2.19)$$

with

$$H(x) = \frac{1 + 2x}{1 + 2\gamma x} , \qquad (2.20)$$

where

$$\gamma = \sqrt{1 - w} . \qquad (2.21)$$

Thus, for isotropic scatterers, the total radiance scattered at the detector from the surface is

$$I_D(\mu, \mu_0, g) = J \frac{w}{4\pi} \frac{\mu_0}{\mu + \mu_0} H(\mu)H(\mu_0) , \qquad (2.22)$$

obtained summing eq. (2.18) – with $P(g) = 1$ – and eq. (2.19). The bidirectional reflectance, $r(i, e, g)$ (or $r(\mu, \mu_0, g)$), of a planar, semiinfinite, particulate medium illuminated by collimated radiation from zenith angle i, observed at zenith angle e, and phase angle g is given, for isotropic scatterers, by

$$r(\mu, \mu_0, g) = \frac{w}{4\pi} \frac{\mu_0}{\mu + \mu_0} H(\mu)H(\mu_0) . \qquad (2.23)$$

The previous relation has been obtained dividing the radiance at the detector I_D and the irradiance incident on the medium J.

Chandrasekhar (1960) obtained the exact solution of the isotropic scattering problem. His solution has the same form as eq. (2.22), expect that his H-functions are solutions of the integral equation

$$H(x) = 1 + \frac{w}{2} xH(x) \int_0^1 \frac{H(x')}{x + x'} dx' , \qquad (2.24)$$

which must be evaluated numerically. The approximate evaluation of the H-function in eq. (2.20) and the exact solution are compared in Figure 2.3, where it is shown that the two solutions differ by less than 4%. A better approximation for the H-function (Hapke 2002) is the following

$$H(x) \simeq \left[1 - w x \left(r_0 + \frac{1 - 2r_0 x}{2} ln \frac{1 + x}{x}\right)\right]^{-1} , \qquad (2.25)$$

with

$$r_0 = \frac{1 - \gamma}{1 + \gamma} . \qquad (2.26)$$
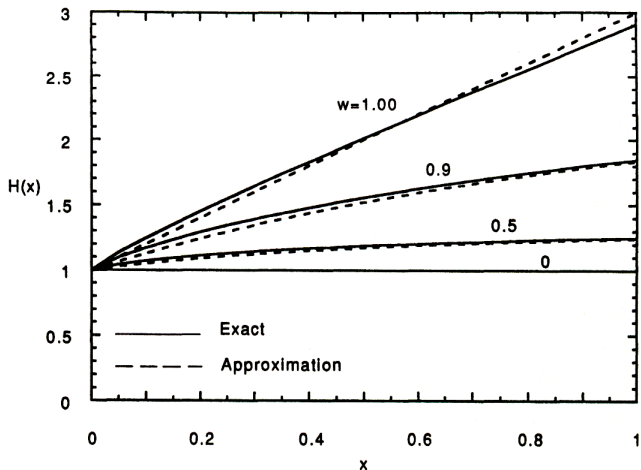
Figure 2.3: The function $H(x)$ versus x for several values of w is shown. Solid lines represent the exact solution; dashed line shows the approximation given by eq. (2.20). Source: Hapke (1993).
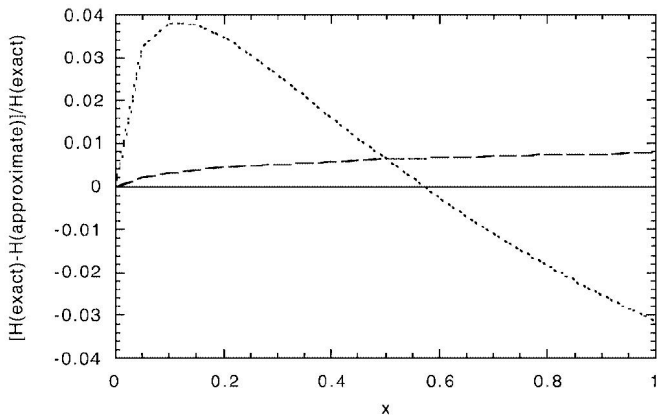
Figure 2.4: The relative difference between the approximate expressions and the exact values of the H-functions for $w = 1$ is plotted against the argument of the H-function. Dashed line refers to the approximation given by eq. (2.25), while dotted line is relative to the approximation given by eq. (2.20). Adapted from Hapke (2002).

The relative difference between approximate and exact values is shown in Figure 2.4 for both the approximation given by eq. (2.20) and the improved one, given by eq. (2.25), for the case $w = 1$. The improved expression deviates from the exact solution less than 1%. The relative differences are smaller for $w < 1$.

Chandrasekhar (1960) has emphasized that for a semiinfinite medium, the multiply scattered portion I_{Dm} of I_D is much less sensitive to the volume phase function than the singly scattered fraction I_{Ds}. Since the single-scattering term can be evaluated exactly for an arbitrary volume phase function and the multiply scattered term is relatively insensitive to phase function, a first order expression of I_D for nonisotropic scatterers can be obtained by using the exact expression for I_{Ds} given in eq. (2.18) but retaining the isotropic solution for I_{Dm} expressed in eq. (2.19). Then

$$I_D = J \frac{w}{4\pi} \frac{\mu_0}{\mu + \mu_0} \left[P(g) + H(\mu)H(\mu_0) - 1 \right] . \tag{2.27}$$

Hence, the bidirectional reflectance may be approximated by

$$r(\mu, \mu_0, g) = \frac{w}{4\pi} \frac{\mu_0}{\mu + \mu_0} [P(g) + H(\mu)H(\mu_0) - 1] . \tag{2.28}$$

2.2.1 The Henyey-Greenstein function

The volume phase function $P(g)$ describes the angular pattern into which the radiation is scattered by the medium. Henyey and Greenstein (1941) introduced the empirical phase function

$$P(g) = \frac{1 - \xi^2}{(1 + 2\,\xi \cos g + \xi^2)^{3/2}} , \tag{2.29}$$

where ξ is the *cosine asymmetry factor* which is the average value of the cosine of the scattering angle $\pi - g$. This versatile function has the following useful properties. It is normalized such that

$$\frac{1}{4\pi} \int_{4\pi} \frac{1 - \xi^2}{(1 + 2\,\xi \cos g + \xi^2)^{3/2}} d\Omega = 1 . \tag{2.30}$$

It is isotropic ($P(g) = 1$) when $\xi = 0$. If $\xi > 0$, $P(g)$ increases monotonically between 0 and π, and decreases monotonically if $\xi < 0$. Figure 2.5 shows the Henyey-Greenstein phase function for several values of the asymmetry parameter ξ. For example, in the case of Pluto, Olkin et al. (2007) performed the modeling adopting $\xi = -0.3$, which is close to the global value found for Triton from Voyager measurements (Hillier et al. 1994).

Sometimes a double Henyey-Greenstein function is used, with one term describing the back-scattering lobe, and another term the forward scattering lobe. In particular, the double Henyey-Greenstein phase function is the sum of two Henyey-Greenstein phase functions, one being forward scattering, and the other being backward scattering. It is parameterized by ξ, which is the cosine asymmetry factor, and c, which indicates the amount of forward or backward scattering. The double Henyey-Greenstein function has the form (Domingue and Hapke 1992)

$$P(g) = cP(g, \xi) + (1 - c)P(g, -\xi) . \tag{2.31}$$
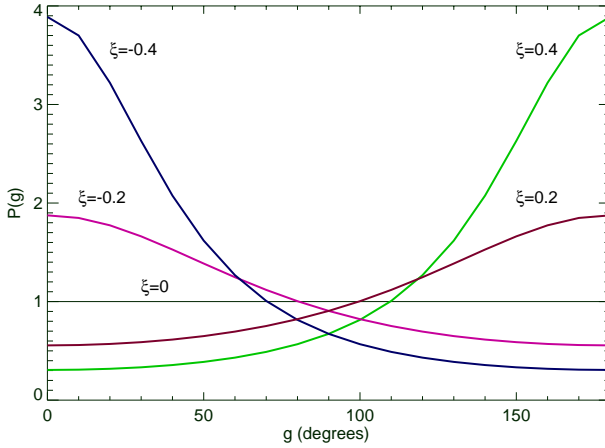
Figure 2.5: Henyey-Greenstein phase function for several values of the asymmetry parameter ξ is shown.

For example, Buie and Grundy (2000) performed the modeling of Charon's spectrum using a two-parameter double Henyey-Greenstein function with $\xi = 0.615$ and forward weight 80%. Indeed, this configuration fits the Buie et al. (1997) photometry and is comparable with parameters reported for other icy satellites.

2.2.2   Opposition effect

For many Solar System bodies and laboratory samples, the reflectance shows a nonlinear increase at small phase angles close to opposition. This nonlinear peak is usually called *opposition surge* or *opposition effect*. The effect has been studied by Hapke (1993), and an approximate analytic correction is added to eq. (2.28) to take this effect into account. Two "mechanisms" are considered to contribute to the opposition effect: *shadow-hiding opposition effect* (SHOE) and *coherent backscatter opposition effect* (CBOE).

SHOE is due to the fact that the shadow cast by one particle of the medium on another can be seen at all angles except zero phase, when each particle hides its own shadow, causing a relatively broad surge in brightness at small phase angles. It is possible to understand this effect in the following way. The factor $exp(Ez/\mu_0)$ represents the probability that a portion of the surface of a particle at depth z will be directly illuminated by radiation of intensity J which has penetrated to that particular point without being blocked by another particle. Likewise, the other factor $exp(Ez/\mu)$ can be regarded as the probability that the radiation emerging from the same area on the surface of the particle in the direction of the detector will reach the $z = 0$ plane without encountering another particle. However, near zero phase the two probabilities are not independent because the incident light preselects a preferential escape path. That is, if the source happens to be located in a
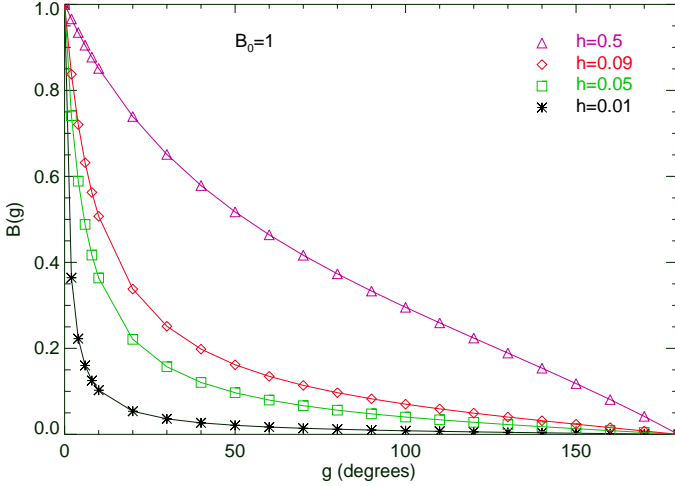
Figure 2.6: The backscatter function for several values of compaction parameter h, in correspondence of $B_0 = 1$ is shown.

way that the incident radiation can penetrate to a certain place without being blocked, then the radiation which happens to be scattered directly back within a small angle about the source direction will reach the $z = 0$ plane without attenuation. Thus, for radiation within this small angle the escape probability is unity rather than $exp(Ez/\mu)$ (Hapke 1981). The preferential escape applies only to the unscattered illuminating radiation J, because the multiply scattered radiation $I(z, \Omega')$ bathes all the particles in a volume element uniformly and does not preselect an escape path. Thus, the SHOE involves only the singly scattered rays.

The CBOE results from the fact that portions of waves travelling in opposite directions along the same multiply scattered paths within a scattering medium interfere constructively with each other as they exit the medium near zero phase and cause a relative peak in brightness (Hapke 2002). Contrary to SHOE, CBOE is caused by particles with comparable or smaller size than wavelength. This is the reason for which we neglect CBOE as mechanism contributing to the opposition effect and we will consider SHOE only.

SHOE involves only the singly scattered rays. Therefore, this model leads to a modified form for I_{Ds}

$$I_{Ds} = J \frac{w}{4\pi} \frac{\mu_0}{\mu + \mu_0} P(g)[1 + B(g)] \ . \tag{2.32}$$

The function $B(g)$ is the *backscatter function*

$$B(g) = \frac{B_0}{1 + (1/h)tan(g/2)} \ , \tag{2.33}$$

where h is called *compaction parameter* and characterizes the width of the nonlinear increase in the reflectance phase curve with decreasing phase angle (the opposition surge)
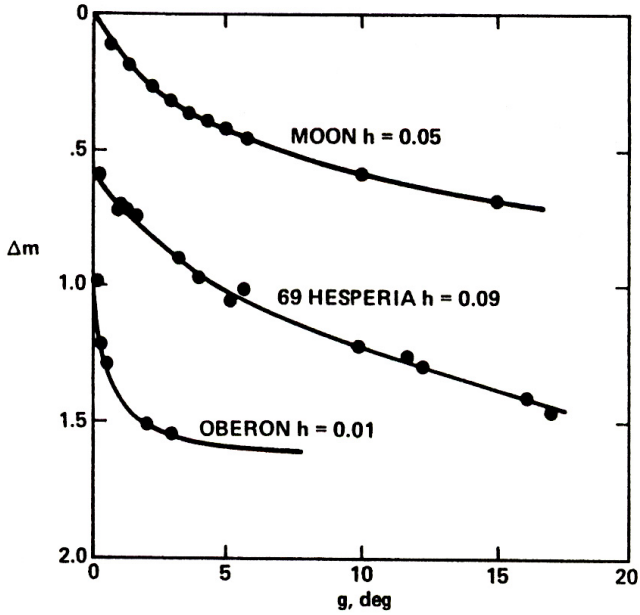
Figure 2.7: The opposition effect in magnitudes versus phase angle g for three bodies of the Solar System. The dots are data and the lines are the theoretical function, with the values of the parameter h for which a good fit has been obtained. Source: Hapke (1986).

in terms of surface properties. It is essentially equal to the ratio of the mean size of the openings between soil particles ($< a_e >$) to the extinction mean free path ($1/E$):

$$h = \frac{1}{2}E < a_e > \ .$$ (2.34)

The derivation of the SHOE will not be reported here. Readers are referred to Hapke (1993). B_0 is an empirical factor and represents the amplitude of the opposition effect. Theoretically, in a perfect case (particles behaving as points), the SHOE will give a unity amplitude parameter. But for real cases, this parameter is usually smaller than unity because of the finite size of particles. Indeed, the finite size of the particle makes the point at which the ray is scattered by a particle in the medium different from the point at which it enters. If the ray is scattered by specular reflection directly from the particle surface, or after penetrating only a short distance into the particle and being scattered back out by subsurface scatterers, then the amplitude of the opposition effect will be close to its theoretical value of 1. However, the refracted rays and the internally reflected, backscattered rays may enter and leave the particle at points that are separated by up to

48

nearly the entire particle diameter, and for this light the opposition effect is negligible. For a true shadow-hiding opposition effect we have $0 \leq B_0 \leq 1$, and B_0 is the ratio of the light scattered from near the illuminated surface of the particle to the total amount of light scattered at zero phase

$$B_0 = \frac{S(0)}{wP(0)} \, ,$$ (2.35)

where $S(0)$ is the light scattered at or close to the part of the surface of the particle facing the source, and $wP(0)$ is the total amount of light scattered by the particle at zero phase. Figure 2.6 shows the backscatter function B(g), in the ideal case $B_0 = 1$, for several values of the compaction parameter h. Taking into account the SHOE, the bidirectional reflectance $r(\mu, \mu_0, g)$ of a planar, semiinfinite, particulate medium illuminated by collimated radiation from zenith angle i, observed at zenith angle e, and phase angle g, is given to a good approximation by

$$r(\mu, \mu_0, g) = \frac{w}{4\pi} \frac{\mu_0}{\mu + \mu_0} [(1 + B(g))P(g) + H(\mu)H(\mu_0) - 1] \, .$$ (2.36)

Hapke (1986) verified the SHOE theory by fitting eq. (2.36) to photometric measurements of several Solar System bodies. The observations are those of Whitaker (1969) for the Moon, Bowell and Lumme (1979) for the asteroid 69 Hesperia, and Brown and Cruikshank (1983) for Uranus satellite Oberon. The results of this analysis are shown in Figure 2.7, along with the values of h for which the theory gave a good fit.

2.2.3 Macroscopic Roughness

The theory described in the previous sections is based on the implicit assumption that the apparent surface of the particulate medium is smooth on scales large compared with the particle size. In (Hapke 1984) the expression for the bidirectional reflectance in eq. (2.36) of a smooth surface has been corrected to include effects of general macroscopic roughness. The correction involves only one arbitrary parameter, the *mean slope angle* $(\bar{\theta})$, and it is applicable to surfaces of any albedo. The actual surface is supposed to consist of an assemblage of smooth, unresolved facets of area A_f of a particulate material, where A_f is large compared with the cross-sectional areas of the particles, but small compared with the area viewed by the detector. The normals to the facets are described by a two dimensional slope distribution function $a(\theta, \xi)d\theta d\xi$, where θ is the zenith angle between the normal to a facet and the vertical, and ξ is the azimuth angle of the facet normal. Assuming that the distribution function of the facet orientation is independent from the azimuth angle, it is possible to write the slope distribution as $a(\theta)$. This hypothesis is reasonable on the average for surfaces covered by craters, boulders, and similar features. The mean slope angle $(\bar{\theta})$ that characterizes the problem is defined in the following way

$$tan\bar{\theta} = \frac{2}{\pi} \int_0^{\pi/2} a(\theta) tan\,\theta d\theta \, .$$ (2.37)

Considering macroscopic roughness means taking into account the mutual shadow that the facets produce, which have the effect of decreasing the reflectance. The facets that are tilted away with respect to the source or the detector do not contribute to the reflectance, so

that the surfaces that are visible by the detector and illuminated by the source will be those that are tilted preferentially toward the detector or the source. This two effects are taken into account by Hapke (1984) writing the bidirectional reflectance $r(i, e, g)$ as the product of the *shadowing function* $S(i, e, g)$ and the bidirectional reflectance of a smooth surface $r(i_e, e_e, g)$ tilted in order to have effective angle of incidence i_e and angle of emergence e_e, in the following way

$$r(\mu_0, \mu, g) = r(\mu_{0e}, \mu_e, g) S(\mu_0, \mu, g) , \qquad (2.38)$$

where

$$\mu_{0e} = cos\, i_e , \qquad (2.39)$$

and

$$\mu_e = cos\, e_e . \qquad (2.40)$$

The expressions of the cosines of i_e, e_e, and S are listed here, without giving the details of derivation and the involved assumptions. Readers are referred to Hapke (1984, 1993). If $i \le e$,

$$\mu_{0e} \simeq \chi(\bar\theta) \left[cos\, i + sin\, i\, tan\, \bar\theta\, \frac{cos\, \psi\, E_2(e) + sin^2 (\psi/2) E_2(i)}{2 - E_1(e) - (\psi/\pi) E_1(i)} \right] , \qquad (2.41)$$

$$\mu_e \simeq \chi(\bar\theta) \left[cos\, e + sin\, e\, tan\, \bar\theta\, \frac{E_2(e) - sin^2 (\psi/2) E_2(i)}{2 - E_1(e) - (\psi/\pi) E_1(i)} \right] , \qquad (2.42)$$

$$S(i, e, \psi) \simeq \frac{\mu_e}{\mu_e(0)} \frac{\mu_0}{\mu_{0e}(0)} \frac{\chi(\bar\theta)}{1 - f(\psi) + f(\psi) \chi(\bar\theta) [\mu_0/\mu_{0e}(0)]} . \qquad (2.43)$$

If $e \le i$,

$$\mu_{0e} \simeq \chi(\bar\theta) \left[cos\, i + sin\, i\, tan\, \bar\theta\, \frac{E_2(i) - sin^2 (\psi/2) E_2(e)}{2 - E_1(i) - (\psi/\pi) E_1(e)} \right] , \qquad (2.44)$$

$$\mu_e \simeq \chi(\bar\theta) \left[cos\, e + sin\, e\, tan\, \bar\theta\, \frac{cos\, \psi E_2(i) + sin^2 (\psi/2) E_2(e)}{2 - E_1(i) - (\psi/\pi) E_1(e)} \right] , \qquad (2.45)$$

$$S(i, e, \psi) \simeq \frac{\mu_e}{\mu_e(0)} \frac{\mu_0}{\mu_{0e}(0)} \frac{\chi(\bar\theta)}{1 - f(\psi) + f(\psi) \chi(\bar\theta) [\mu/\mu_e(0)]} , \qquad (2.46)$$

where

$$\chi(\bar\theta) = 1/(1 + \pi\, tan^2\bar\theta)^{1/2} , \qquad (2.47)$$

$$E_1(x) = \exp \left(-\frac{2}{\pi} cot\, \bar\theta\, cot\, x \right), \qquad (2.48)$$

$$E_2(x) = \exp \left(-\frac{1}{\pi} cot^2\, \bar\theta\, cot^2\, x \right), \qquad (2.49)$$

$$f(\psi) = \exp \left(-2tan\, \frac{\psi}{2} \right). \qquad (2.50)$$

Thus the bidirectional reflectance function of a rough surface is

$$r(i, e, g) = \frac{w}{4\pi} \frac{\mu_{0e}}{\mu_e + \mu_{0e}} \{ [1 + B(g)] P(g) + H(\mu_e) H(\mu_{0e}) - 1 \} S(i, e, g) . \qquad (2.51)$$

2.3 Mixing Formulas

The previous relation – see eq. (2.51) – can be used to compute the bidirectional reflectance of a medium composed of closely packed particles of a single component. Few materials encountered in nature consist of only one type of particle. Hence, in order to calculate synthetic reflectance spectra for comparison with the observational data for planetary surfaces, it is necessary to be able to compute the reflectance of mixtures of different types of particle. In remote sensing two kind of mixtures are of interest: areal and intimate.

2.3.1 Areal mixtures

One kind of surface configuration consists of materials of different composition and/or microphysical properties that are spatially isolated from one another. For example, the spectra of (63252) 2001 BL_{41}, (26181) 1996 GQ_{21} (Doressoundiram et al. 2003), and (8405) Asbolus (Romon-Martin et al. 2002) are modeled with geographical mixtures of tholins, ice tholin, amorphous carbon. With this configuration the emergent flux of scattered sunlight integrated over the whole illuminated surface includes light scattered from each kind of surface, weighted by the fraction of the surface covered with each kind. These areal, or geographically segregated surfaces are expected to be more typical for a real body in the Solar System, in contrast to a homogenous surface. For areal mixtures, the reflectance of the individual components is calculated and then combined at each wavelength to give the total reflectance r of the spatially mixed surface

$$r = \sum_j F_j r_j \, , \qquad (2.52)$$

where r_j is the reflectance of the j-th area and F_j represents the fractional areal extent or spatial coverage of each component, such that $\sum_j F_j = 1$. Areal mixtures are the simplest to treat. Thus, spectra are first modeled with an areal mixture configuration. If the synthetic spectrum does not fit satisfactorily the data, intimate mixtures are considered.

2.3.2 Intimate mixtures

In an intimate mixture the surface consists of different types of particles mixed homogeneously together in close proximity (Hapke 1993). For example, the spectrum of 2005 FY_9 has been modeled using an intimate mixture of ethane, methane and tholin (Brown et al. 2007a). In the case of intimate mixture the averaging process is on the level of the individual particle and the parameters that enter in the reflectance equation are averages of the properties of the various types of particles in mixture weighted by cross-sectional area. To model an intimate mixture of different compositions, we need to modify the parameters of the particles that enter in the bidirectional reflectance equation (Hapke 1993). Specifically, the volume single-scattering albedo becomes the average single-scattering albedo weighted by cross-sectional area. Similarly, the opposition effect term, B_0 is also the weighted average of the individual B_0 values. The cross-sectional area is the fractional volume V divided by the size of the grains D. We have the following relation for

the bidirectional reflectance of an intimate mixture

$$r(i, e, g) = \frac{\overline{w}}{4\pi} \frac{\mu_{0e}}{\mu_e + \mu_{0e}} \{[1 + \overline{B}(g)]P(g) + \overline{H}(\mu_e)\overline{H}(\mu_{0e}) - 1\}S(i, e, g) , \qquad (2.53)$$

where

$$\overline{w} = \left[\sum_j \frac{V_j}{D_j} w_j\right]\left[\sum_j \frac{V_j}{D_j}\right]^{-1} , \qquad (2.54)$$

$$\overline{B}(g) = \frac{\overline{B}_0}{1 + (1/h)tan(g/2)} , \qquad (2.55)$$

$$\overline{H}(x) \simeq \left[1 - \overline{w}\, x \left(\overline{r}_0 + \frac{1 - 2\overline{r}_0 x}{2} ln\frac{1 + x}{x}\right)\right]^{-1} , \qquad (2.56)$$

with

$$\overline{B}_0 = \left[\sum_j \frac{V_j}{D_j} B_{0j}\right]\left[\sum_j \frac{V_j}{D_j}\right]^{-1} , \qquad (2.57)$$

$$\overline{r}_0 = \frac{1 - \sqrt{(1 - \overline{w})}}{1 + \sqrt{(1 - \overline{w})}} , \qquad (2.58)$$

in which the subscript j represents the different particle species.

2.4 Modeling algorithm

In this thesis we intend to perform surface characterization of three Transneptunian objects (TNOs) – Pluto, Charon, and (47171) 1999 TC$_{36}$ – by applying the scattering radiative transfer model of Hapke (1993). In order to model the observed reflectance spectra of the studied TNOs and to extract, in this way, information about their surface composition, an IDL (Interactive Data Language) routine has been developed. This routine computes the bidirectional reflectance of a geographical or an intimate mixture $r(i, e, g)$ given the optical constants of the assumed surface ices of the mixture together with the geometry of the system (incident angle i, emission angle e, and phase angle g). Anisotropic scattering (Section 2.2.1) is considered, together with opposition effect (Section 2.2.2), and large scale roughness (Section 2.2.3).

The first step in the modeling algorithm is the computation of the volume single-scattering albedo w for each element in the mixture. This is possible only if the optical constants n and k, the real and imaginary part of the refractive index, respectively, of each element in the mixture, as function of the wavelength λ, are known. Indeed, following Hapke (1993), it is possible to express w, the ratio between the scattering and the extinction volume coefficients – see eq. (2.11) –, in the following way

$$w = S_e + (1 - S_e)\frac{1 - S_i}{1 - S_i\Theta}\Theta , \qquad (2.59)$$

where S_e and S_i are given by the following approximations

$$S_e \simeq \frac{(n - 1)^2 + k^2}{(n + 1)^2 + k^2} + 0.05 , \qquad (2.60)$$

$$S_i \simeq 1 - \frac{4}{n(n+1)^2} ,$$ (2.61)

and Θ, internal transmission factor, is function of the particles diameter D

$$\Theta = e^{-\alpha D} ,$$ (2.62)

with the absorption coefficient α equals to $4\pi k/\lambda$. After computing the volume single-scattering coefficient w for each element in the mixture, it is possible to determine the bidirectional reflectance of a geographic or an intimate mixture as function of:

- **the optical constants n and k of each element in the mixture**

    This dependence appears in w – see eq. (2.59) – and in the amplitude of the opposition effect B_0 – see eq. (2.35). It is possible to express $S(0)$, that represents the light scattered at or close to the part of the surface of the particle facing the source, as

    $$S(0) = \frac{(n-1)^2 + k^2}{(n+1)^2 + k^2} .$$ (2.63)

    Also the H-function – see eq. (2.25) – depends from n and k, since it depends from w.

- **the concentration of each surface terrain in the mixture**

    In the case of areal mixture, the spatial coverage of each component F_j is the factor by which the bidirectional reflectance of each element in the mixture is multiplied – see eq. (2.52). In the case of an intimate mixture the mean volume single-scattering albedo – see eq. (2.54) – and the mean opposition effect amplitude – see eq. (2.57) – will be functions of the fractional volume of each component, consequently also the H-function – see eq. (2.56).

- **the grain size of each surface terrain in the mixture**

    The volume single scattering albedo w, and consequently the H-function and the opposition effect amplitude, depends from the grain size D of each element in the mixture – see eq. (2.59-2.62). In the case of an intimate mixture the mean volume single-scattering albedo – see eq. (2.54) – and the mean opposition effect amplitude – see eq. (2.57) – will be functions of the grain size of each component, indeed they will be weighted by the cross-sectional area, that is the fractional volume divided by the size of the grains.

- **the compaction parameter h**

    The backscatter function $B(g)$ depends from h – see eq. (2.33).

- **the cosine asymmetry factor ξ**

    The particle phase function $P(g)$, that describes the angular pattern into which the radiation is scattered, depends from ξ – see eq. (2.29).

- **the mean roughness slope $\bar{\theta}$**

    The shadowing function S depends from $\bar{\theta}$ – see eq. (2.43) and eq. (2.46) –, but also the H-function because of the dependence of μ_e and μ_{0e} – see eq. (2.41,2.42,2.44,2.45) – from $\bar{\theta}$.

Once the bidirectional reflectance of a geographic or an intimate mixture is known, the next and final step in the modeling algorithm is the computation of the geometric albedo of the target, A_p, that will be compared with the observations. The geometric albedo is defined as the ratio of the brightness of a body at $g = 0$ to the brightness of a perfect Lambert disk[2] of the same radius and at the same distance as the body, but illuminated and observed perpendicularly. It can be demonstrated that A_p is equal to the bidirectional reflectance multiplied by the cosine of the emergent angle e and π.

In the particular case of Pluto we have followed the approach by Olkin et al. (2007). The spherical body of the target has been approximated by a 30×30 bi-dimensional grid of surface elements, and for each surface element incident angle and emission angle (i_l, e_l) are computed. In this case the geometric albedo is computed using the following relation

$$A_p = \frac{\pi \sum_{l=1}^{N} r(i_l, e_l, g) cose_l}{N} \ ,$$

$$(2.64)$$

where N is the total number of surface elements covering the visible disk of the body.

The free parameters in our model are grain size and contribution of each surface terrain to the mixture. They are iteratively modified by means of a χ^2 minimization algorithm (Levenberg-Marquardt least-squares minimization) until a best-fit to the observations is achieved. For the cosine asymmetry parameter (ξ), the compaction parameter (h) and the mean roughness slope ($\overline{\theta}$) we considered values known from previous studies, that will be stressed in the description of the modeling analysis of each target studied in this thesis.

We can anticipate that, in the case of Pluto (see Section 3.3.1.1), we have considered values of ξ and $\overline{\theta}$ equal to -0.3 and 14°, respectively, based on analogy to Triton (Hillier et al. 1994). We have assumed a value for the compaction parameter, h, of 0.5 in analogy with Olkin et al. (2007).

For Charon (see Section 3.3.2.1) we have adopted the same parameters as in Buie and Grundy (2000). In particular we have assumed: $h = 0.01$, $B_0 = 0.06$, and $\overline{\theta} = 20°$. For $P(g)$ a two-parameter double Henyey-Greenstein function with asymmetry 0.615 and forward weight equals to 80% has been used. This configuration fits the Buie et al. (1997) photometry.

(47171) 1999 TC_{36} does not present strong absorptions as in the case of Pluto and Charon. Hence, the most simple model needs to be used. This is the reason for which we have considered isotropical scattering, zero surface roughness, and compaction parameter (h) equals to 0.05 (a lunar-like surface, see Figure 2.7).

2.5   Sensitivity of the modeling algorithm to the free parameters

Although Hapke's model is generally able to describe the spectral properties of the analysed objects quite well, it is important to note that it is only indicative for our and most of the applications to Solar System bodies. Mixtures with different grain sizes or different mixing ratios of the constituents can give very similar fits to the data. Therefore,

---

[2]A Lambert surface appears equally bright when viewed from any angle and reflects all the light incident on it.
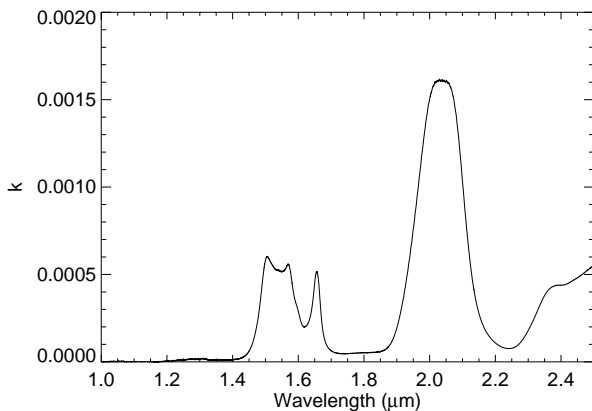
Figure 2.8: The imaginary part of the refractive index k of crystalline water ice is shown in the wavelength range (1-2.5) μm.

the accurate and realistic determination of the surface composition may be difficult. The sensitivity of the modeling to each of the free parameters (grain size and contribution of each surface terrain in the mixture) considered is analysed in the next sections.

2.5.1 Grain size

The grain size affects directly the optical depth of the radiation. A larger grain has a greater internal path where photons may be absorbed. This contributes to the attenuation of the reflectance. Let's consider as example the case of crystalline water ice. The optical constants of H_2O have been obtained from Grundy and Schmitt (1998) in the range (0.96-2.74) μm at 40K. Figure 2.8 shows the imaginary part of the refractive index of H_2O, while the real part n is constant, equal to 1.2, in the range (1-2.5) μm. As mentioned above, in the case of an homogeneous surface, the dependence from the grain size D of the particles appears only in the volume single scattering albedo w – see eq. (2.59-2.62) –, and consequently in the H-function – see eq. (2.25) – and in the opposition effect amplitude B_0 – see eq. (2.35). Figure 2.9 shows the volume single scattering albedo of H_2O in the range (1-2.5) μm for different values of grain size D. It is possible to verify that w decreases with increasing grain size. Thus, the reflectance r, and consequently the geometric albedo A_p, decreases with increasing D (Figure 2.10). Also the absorption band contrast varies with particle size. In particular, the absorption depth is directly proportional to the grain size. This effect starts to be absent when the absorptions are saturated (green dash-dot line in Figure 2.10). There are not variations in the position of the absorption features.
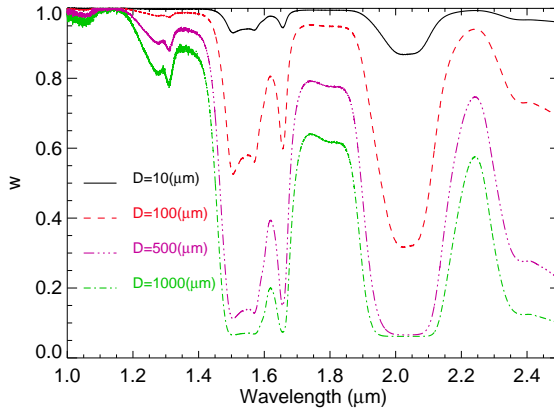
Figure 2.9: The volume single scattering albedo *w* of H_2O in the wavelength range (1-2.5) *μm* for different grain size *D*.
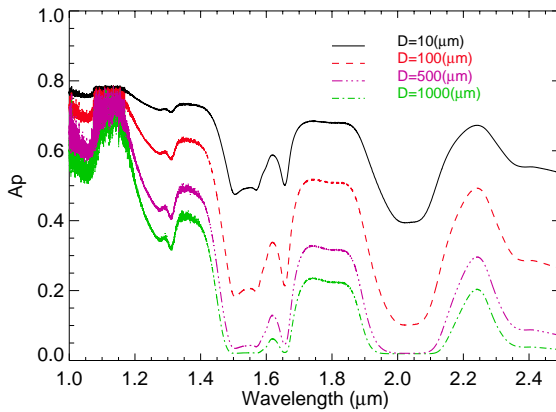
Figure 2.10: The geometric albedo A_p of H_2O in the wavelength range (1-2.5) *μm* for different grain size *D*.
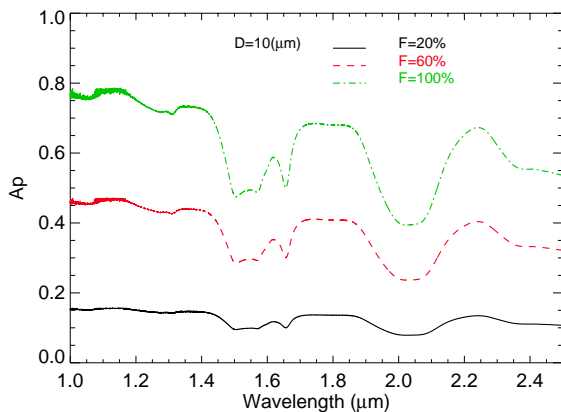
Figure 2.11: The geometric albedo A_p of H_2O in the wavelength range (1-2.5) μm for different abundance F.
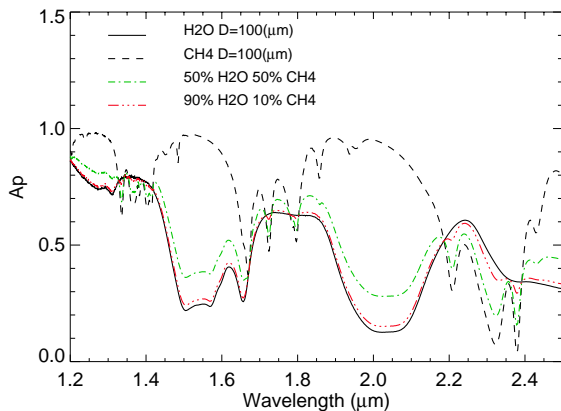
Figure 2.12: The geometric albedo consisting of pure 100 μm grains CH_4 (black dashed line) and pure H_2O (black solid line) at 100 μm grains is shown in the range (1.2-2.5) μm. The sensitivity of the geometric albedo of an intimate mixture to changes in the abundance of the end-members is shown in the figure by two mixing examples.

2.5.2   Concentration

In order to understand the effect of concentration or abundance of a material on the geometric albedo of a mixture we have to distinguish between areal and intimate mixture. Indeed it has been already shown that in the case of areal mixture, the geometric albedo is a linear function of the spatial coverage of each component. The dependence in the case of intimate mixture is more complicated.

Let's start considering the case of areal mixture. Figure 2.11 shows the geometric albedo of H_2O ice of 10 μm grains obtained for different concentration values. It is clear that the reflectance increases with increasing abundance as well as absorption depth. We can conclude that concentration and grain size are linked. Indeed, very similar model results can often be obtained for large grain size + weak concentration and small grain size + large concentration.

The case of intimate mixture is more complicated. As an example, we consider an intimate mixture of H_2O ice and methane ice CH_4 (optical constants at 60K from Grundy et al. (2002b)). The geometric albedo of pure CH_4 (black dashed line) and pure H_2O (black solid line) with 100 μm grains in the range (1.2-2.5) μm is shown in Figure 2.12. Comparing the geometric albedo of the intimate mixture (green dash-dot line) obtained with 50% of H_2O (100 μm grains) and 50% of CH_4 (100 μm grains) and that relative to the intimate mixture of 90% of H_2O and 10% CH_4 (red dash-dot-dot-dot line), it is possible to conclude that in the case of intimate mixture the increasing abundance of an element results in the increasing depth of its absorption bands. For example, reducing the abundance of CH_4 from 50% to 10% makes the absorption bands at 2.2 μm and 2.4 μm almost disappearing.

3 Surface characterization of Pluto and Charon by L- and M-band spectra

Most of what is currently known about the surface compositions of Pluto and Charon has been derived from spectroscopic observations at wavelengths ranging from the visible to 2.5 μm, where ices such as N_2, CH_4, CO_2, CO, and H_2O exhibit distinctive patterns of vibrational overtone absorption bands (Cruikshank et al. 1993; Owen et al. 1993; Douté et al. 1999; Buie and Grundy 2000). Up to now, the L- and M-band regions have been under-exploited for outer Solar System studies, because of the weak solar flux, the presence of strong telluric absorptions, and lack of adequate instrumentation. However, longer wavelengths offer several potential advantages since the fundamental vibrational transitions of many ice species (such as H_2O, CH_4, CO, CO_2) are located in this region and the absorptions are much stronger than those observed shortward of 2.5 μm.

The first attempt to investigate Pluto's L-band was done by Spencer et al. (1990), obtaining photometric observations of Pluto through four filters spanning the 2.8-4 μm range. Spencer et al. (1990) found a strong absorption around 3.2 μm, consistent with the ν_3 absorption band of CH_4 ice, but the spectral resolution of the data was insufficient to yield additional compositional constraints beyond what had already been ascertained from shorter wavelength observations (see Section 1.5.1). The first albedo spectrum of the unresolved Pluto/Charon system in the wavelength range (2.8-4.1) μm has been published by Grundy et al. (2002a). These data, broadly consistent with earlier observations from Spencer et al. (1990), exhibit strong absorption bands near 3.3, 3.5, and 3.8 μm corresponding to the methane's ν_3, $\nu_2 + \nu_4$, and $2\nu_4$ vibrational transitions, respectively. Comparing the observations with a synthetic spectrum computed using parameters from near-infrared models of the surfaces of Pluto (Douté et al. 1999) and Charon (Buie and Grundy 2000), Grundy et al. (2002a) identified the presence of absorptions, not predicted from the existing models, around 2.9 and 4.1 μm, attributed to H_2O ice, along with CO_2 and/or SO_2 ices. Since the contribution of Charon to the unresolved Pluto/Charon system is expected to be minimal in the L-band, the identified absorptions have been attributed to Pluto. The investigation of the L-band spectrum of Pluto/Charon system is further carried on by Olkin et al. (2007), who combined spectra of the unresolved Pluto/Charon system obtained from the Keck and Subaru telescopes from 2.8 to 4.2 μm with 0.8-2.4 μm spectra from the NASA Infrared Telescope Facility. Olkin et al. (2007) proposed as a possible surface scenario for Pluto a geographic mixture of pure CH_4, CH_4 diluted in N_2, and tholin. This result was obtained after modeling and removing the contribution

of Charon from the measured reflectance spectra. Since there were no measured Charon-only spectra beyond 2.5 μm, it was assumed that the same H_2O ice and spectrally neutral continuum absorber that dominates Charon's spectrum at shorter wavelengths (Buie and Grundy 2000) is dominant beyond 3 μm as well. The work of Olkin et al. (2007) highlights the importance of performing modeling analysis of the spectroscopic observations simultaneously in the near- and medium-infrared wavelength ranges. Indeed, following this approach, Olkin et al. (2007) does not confirm the presence of H_2O ice, CO_2 and/or SO_2 on Pluto's surface, predicted by Grundy et al. (2002a). The main limit is the lack of spectroscopic observations of Pluto and Charon resolved.

In this chapter, spectroscopic observations of the Pluto/Charon system, performed at the European Southern Observatory (ESO) Chile, are presented. In particular, we aim to resolve the binary system and to obtain, for the first time, spectra up to 5 μm for Pluto and up to 4 μm for Charon. These observations have been analysed, using the radiative transfer model of Hapke (1993) (described in detail in Chapter 2), in order to retrieve information on the composition, properties, and distribution of the ices present on the surface of Pluto and its moon Charon. The present work extends the wavelength coverage of the surface spectroscopy beyond the K-band, with the goal to detect further surface ice absorption bands predicted from the models that are based on the available JHK spectra, and to search for signatures of yet unknown ices. Pluto's M-band has never been explored before and the results presented in this chapter will complement the information coming from New Horizons that will perform spectroscopy of Pluto's surface in the JHK bands only (see Section 1.6).

3.1   Observations and data reduction

In this section we present the Pluto/Charon spectroscopic measurements. The attention is focused first on the instrument set-up and observing procedure. A detailed description of the data reduction steps follows.

3.1.1   Telescope and instrument set-up

The Pluto/Charon spectroscopic observations have been acquired with the NACO instrument (http://www.eso.org/sci/facilities/paranal/instruments/naco/) at the ESO Very Large Telescope (VLT) during the period 3-7 August 2005. An 8-meter class telescope like the VLT was required in order to obtain significant improvement over the existing L-band spectra (Grundy et al. 2002a; Olkin et al. 2007). Also, at the time of the observing application, VLT was the only instrumentation in the world to perform M-band spectroscopy of medium bright objects like Pluto/Charon.

NACO, at the VLT Unit Telescope 4 (Yepun), consists of the Nasmyth Adaptive Optics System (NAOS; AO for adaptive optics) and the High Resolution infrared Camera and Spectrometer (CONICA). The AO system resolved Pluto/Charon (separation was variable along the orbit from 0.5″ to 0.9″) and enabled us to benefit from considerable signal-to-noise improvements for the spectroscopy. Moreover, NACO allowed to cover the full wavelength range 1-5 μm at once using the prism L27_P1. The prism gives the advantage of having the target spectrum in the complete wavelength range (1-5) μm, without

introducing uncertainties related with the adjustment, by photometric measurements, of separate spectra taken in different wavelength bands. A spectral resolution of 35 in J-band and 200 in M-band has been obtained.

The ESO Phase 2 Proposal Preparation Tool (http://www.eso.org/observing/p2pp/), called P2PP, has been used to define the observations, that have been performed in visitor mode. P2PP is a tool designed to provide astronomers the interface needed to define observing sequences (Observations Blocks or OBs) that can then be executed at the telescope with minimum human interaction. All the information necessary to execute an observation like the target position, the instrument and exposure setup parameters are specified in the OB. The exposure parameters, that are mentioned in the next subsection, have been computed using the NACO Exposure Time Calculator (ETC). Since the prism L27_P1 is not included among the spectroscopic modes of the ETC, the L27_1_LP grism has been used as reference, taking into account proper scaling factors (like dispersion).

3.1.2 Observing procedure

The Pluto/Charon binary was used as a reference source for the visible AO sensor of NACO. The slit (width 172 mas) was set along the orbital position angle of the system, in order to acquire Pluto and Charon simultaneously (see Figure 3.1). The S27 camera with a field of view of $28'' \times 28''$ and a scale of 27.15 mas/pixel has been used for the slit acquisition with a detector integration time (DIT) of 10 sec. The slit acquisition was performed
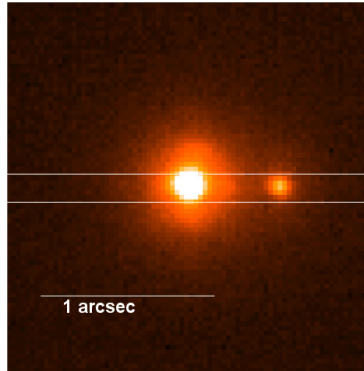
Figure 3.1: Median averaged slit acquisition image of Pluto (on the left in the image) and Charon (on the right in the image) in the night 4 August 2005. The NACO slit is indicated in the figure by two horizontal white lines.

in K-band, and a suitable offset correction, depending on the zenith distance, was applied in order to achieve the optimum slit centering of the objects for L- and M-bands. The offset correction has been computed using the following atmospheric differential refraction formula

$$\Delta R(\lambda) \equiv R(\lambda) - R(\lambda_0) = (n(\lambda) - n(\lambda_0)) \tan z_a \, , \tag{3.1}$$

that gives the differential refraction $\Delta R(\lambda)$ as a function of wavelength, relative to the alignment/guiding wavelength λ_0 (Szokoly 2005). In the case of our measurements λ_0 is equal to 2.18 μm, the central wavelength of K-band. In the previous relation R is the atmospheric dispersion, defined as the difference between the true (z_t) and apparent zenith distance (z_a), and n is the refractive index of the atmosphere. The most general form of the refractive index is given by Cauchy's equation, an empirical relationship between n and the wavelength λ

$$n(\lambda) = A + \frac{B}{\lambda^2} + \frac{C}{\lambda^4} \dots , \qquad (3.2)$$

where A, B, and C are coefficients that have been determined by fitting the equation to measured differential atmospheric refraction at Paranal. The described approach for the slit acquisition slightly sacrificed the JHK signal of the objects, at least for higher airmasses, because of slit losses due to differential atmospheric refraction. Indeed, $\Delta R(\lambda)$ increases with the airmass (AM), defined as the secant of the apparent zenith distance, and with decreasing wavelength (see Figure 3.2). More details on the differential atmospheric refraction are given in the data reduction description (see Section 3.1.3.4).
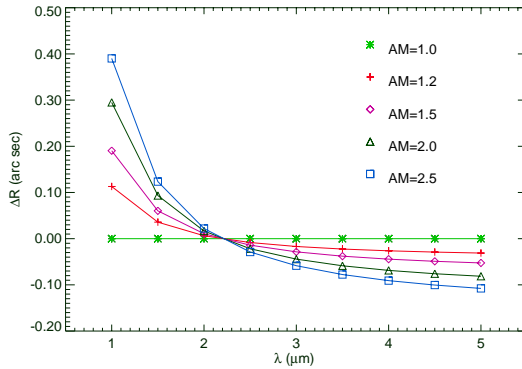
Figure 3.2: Differential refraction as a function of wavelength at different airmass. The values are in arcsec with respect to a wavelength of 2.18 μm.

The observations were performed using the usual A-B-B-A nodding (with some jitter) along the slit. In particular the NACO_Spec_obs_AutoNodOnSlit template that nods the telescope between two positions (A and B) along the slit has been used. The mean size of the nod is defined by the Nod Throw parameter. Hence, the first exposure (A) is taken after offsetting the object along the slit by $\frac{Nodthrow}{2}$ arcsec. The second exposure (B) is therefore $-\frac{Nodthrow}{2}$ from the initial position along the slit. In addition to nodding, random offsets in slit direction called jitter, and defined by the Jitter Box Width parameter, have been added. Offsets are randomly distributed between $\frac{JitterBoxWidth}{2}$ and $-\frac{JitterBoxWidth}{2}$ (see Figure 3.3). For the Pluto/Charon observations the values used for Nod Throw and Jitter Box Width parameters are 5″and 2″, respectively. After the slit acquisition, 5 AB cycles have been obtained. A sequence of 5 cycles with jittering results in the following sequence

$$A(B + \varepsilon_1)(B + \varepsilon_1)(A + \varepsilon_2)(A + \varepsilon_2)(B + \varepsilon_3)(B + \varepsilon_3)(A + \varepsilon_4)(A + \varepsilon_4)(B + \varepsilon_5) , \qquad (3.3)$$

where ε_n are the random jitter offsets along the slit. Each offset position has been acquired with a DIT of 0.8 sec and a number of DITs (NDIT) equals to 150, resulting in a total integration time of 120 sec per slit position. The L27 camera with a field of view of 28″×

NACO_spec_obs_AutoNodOnSlit
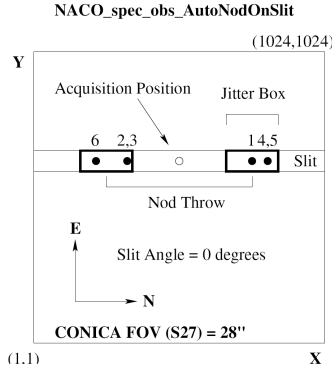
Figure 3.3: An illustration of how the NACO_Spec_obs_AutoNodOnSlit template works. Source: NAOS-CONICA user manual.

28″and a scale of 27.19 mas/pixel is associated to the L27_P1 prism.

In order to remove at once the telluric and solar features from Pluto/Charon spectra, observations of the nearby solar analogue star HD 162341, recorded approximately once per 1.5 hour, have been performed (see Section 3.1.3). In this way every Pluto/Charon observation had an associated "before" and "after" set of calibration star observations, made with similar sky conditions and identical instrument and AO settings. Lamp Flats needed for the data reduction have been observed after the end of each night with the same instrument settings adopted for the target. These Lamp Flats are taken by pairs, lamp "on" and "off".

The observations have been performed during the interval 3-7 August 2005. However, the first night has been used to optimize the observing technique that requested particular care in the slit acquisition. Hence, the measurements recorded in the first night are affected by operational problems. Moreover, the measurements obtained in the third night present electronic noise in the L- and M-range of the detector. Thus, only the second and fourth night of observations have been used for our analysis.

The observational circumstances are listed in Table 3.1, while Table 3.2 summarizes the observing parameters adopted for the Pluto/Charon and solar analogue observations.

UT$_{start}$	UT$_{end}$	α (deg)	Ob-lon (deg)	Ob-lat (deg)	AM	PA (deg)	PARANG (deg)	seeing ('')
2005 August 04 02:07	2005 August 04 05:55	1.44	7÷16	-34	1.03÷2.44	173÷-173	131÷111	0.8-2.2
2005 August 04 23:40	2005 August 05 04:55	1.46	58÷70	-34	1.09÷1.66	-129÷-121	-117÷-110	0.6-1.2
2005 August 05 23:46	2005 August 06 05:46	1.48	114÷128	-34	1.07÷2.43	-94÷-85	-120÷111	0.5-1.2
2005 August 06 23:28	2005 August 07 05:54	1.50	170÷185	-34	1.10÷2.70	-37÷-11	-116÷111	0.6-1.0

Table 3.1: Observing geometry of the Pluto/Charon system for our VLT/NACO measurements in August 2005. The UT time corresponding to the first (UT$_{start}$) and last (UT$_{end}$) Pluto/Charon spectrum is reported. α is the Sun-(Pluto/Charon) barycenter-Earth (phase) angle. Ob-lon and Ob-lat are the apparent planetographic longitude and latitude of the center of Pluto's disk seen by the observer. In particular the apparent planetographic longitude of the first and last Pluto spectrum acquired in the same night are given. Light travel-time target-observer is taken into account. AM is the airmass interval between the first and last Pluto spectrum acquired in the same night. PA and PARANG are position angle and parallactic angle, respectively. The table lists the interval between the values of PA and PARANG of the first and last Pluto spectrum acquired in the same night.

	Pluto/Charon	Solar Analogue
DIT (sec)	0.8	0.5
NDIT (sec)	150	30
Readout mode	Double_RdRstRd	Double_RdRstRd
Jitter Box Width (arcsec)	2	2
Number of AB cycles	5	4
Number of exposures per offset position	1	1
Nod Throw (arcsec)	5	8
Slit	Slit_172mas	Slit_172mas
Spectroscopic Mode	L27_P1	L27_P1

Table 3.2: Observing parameters of the Pluto/Charon and solar analogue spectroscopic measurements. The table lists the detector integration time (DIT) and the number of DITs (NDIT), both given in seconds. The values of the Jitter Box Width and Nod Throw parameters are given together with the number of AB cycles and the number of frames stored per A or B position (see Section 3.1.2). The width of the slit and the spectroscopic mode are specified. Double_RdRstRd is the readout mode used for long wavelength spectroscopy. The array is read, reset and read again.

3.1.3   Data reduction

In this section we describe the data delivered by NACO for the Pluto/Charon observing run and the data reduction steps. Because of the accuracy needed to reduce spectroscopic data acquired with the prism, we have preferred to not use the ECLIPSE data reduction package provided by ESO, but to develop our own reduction pipeline. MIDAS and IDL packages have been used. A scheme of the data reduction procedure follows. Each point is covered in more detail in the next subsections.

Besides the usual data reduction for IR spectroscopy (background subtraction, flat-fielding, ABBA spectra coaddition), special attention was paid to wavelength calibration and spectrum curvature removal of the NACO data (not supported by ECLIPSE). The former has been difficult since arc lamp spectra are not available to calibrate the strongly nonlinear dispersion of the prism. Indeed, at long wavelengths there are no useful arc lines, while at short wavelengths the lines are severely blended. Hence, atmospheric emission and absorption features were used as wavelength reference. The spectrum curvature results from differential atmospheric refraction over the large wavelength range, and was corrected by pixel shifts of the spectra applying the atmospheric refraction formula. Thereafter, we used optimum extraction of the spectra to improve the signal-to-noise ratio over the aperture extraction. Telluric and solar features removal has been applied.

The data reduction has been performed in an iterative loop. In order to improve the signal-to-noise ratio of our spectra, it is necessary to apply the extraction procedure after spectrum rectification. The curvature correction requests the dispersion relation for the wavelength calibration, which can be retrieved only from the extracted spectrum. In order to avoid this difficulty we have determined the dispersion relation from spectra acquired at low values of AM (AM~1.1). Indeed, as explained in the previous section, the differential atmospheric refraction increases with the AM. Hence at low values of AM the spectrum is approximately straight.

An example of the raw bidimensional spectrum image of Pluto/Charon is shown in Figure 3.4 (panel a). The object spectra of Pluto and Charon are the two vertical lines indicated by two arrows. The two spectra are really faint in the raw frame. The basic steps of the data reduction are detailed hereafter.

3.1.3.1   Sky Subtraction

The subtraction between two consecutive frames with the object of interest, offset to distinct regions on the detector, removes the bias (the signal that is registered by the detector in the absence of exposure to light) and the sky signal, and results in an image with two spectra, a positive and a negative one (see Figure 3.4, panel b).

3.1.3.2   Flat-fielding

In order to correct for the pixel-to-pixel sensitivity variations of the detector, it is necessary to normalize the difference frame, obtained in the previous step, by the flat-field. Every morning, after the end of the night and with the telescope closed, (halogen) lamp flats are taken in each combination of spectroscopic mode, slit, camera, and readout mode of the detector used during the night. These flats are internal to CONICA and do not include any effect coming from the telescope or NAOS. The flat-field is the normalized difference of two images, one with the lamp "on" and another with the lamp "off". Three pairs of image-fields are taken. In particular the flat-field is obtained as follows:

- subtract the "off" frame from the "on" one.

- normalize the result frame with the computed mean of the center part of the difference frame. The box chosen for the normalization has to be without "hot" and "cold" pixels. "Hot" and "cold" pixels are defective pixels in the detector. "Hot" pixels have a maximum value, they are filled with charge even if they are not truly gathering that many photons. They appear as pure white in the final image. "Cold" pixels, or dead pixels, register no charge from the photons that strike them, making them pure black in the final image.

- median the results obtained for each "on"-"off" pair.

3.1.3.3   Combining 2d spectra

The difference between frames taken at different slit positions leaves an image with two spectra, one positive (A) and one negative (B). In order to increase the signal-to-noise ratio, alignment and coaddition of the two spectra is performed. The coaddition is done after multiplying the negative spectrum by -1. This method of combining data is often called double sky subtraction as it effectively removes any residual sky that remains after the first subtraction. It results in an image that has one positive spectrum and two negative spectra on either side of the positive spectrum (see Figure 3.4, panel c).
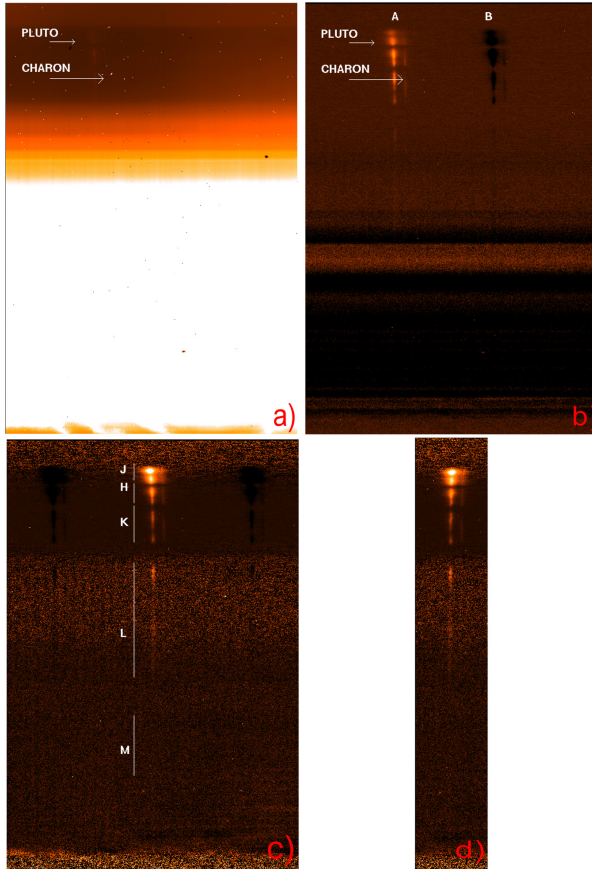
Figure 3.4: The main steps of the spectroscopic data reduction are shown. In each image the along-slit position is on the x-axis and the wavelength along the y-axis, increasing from top to the bottom. Panel a: Raw bidimensional spectrum of Pluto/Charon system acquired in the night 7 August 2006 at airmass 1.85. In the image, the spectra of Pluto (on the left) and Charon (on the right) are the two faint vertical lines indicated by two arrows. Panel b: Difference between two consecutive frames in which the Pluto/Charon system is offset to distinct regions of the detector: the A and B positions along the slit. Panel c: Alignment and coaddition of the positive and negative spectra in the difference frame shown in panel b. The wavelength bands are indicated along the y axis. Panel d: Positive spectrum shown in panel c after rectification.

3.1.3.4   Curvature correction

The differential atmospheric refraction makes the spectra strongly curved (see Figure 3.4, panels b and c) in the short wavelength region, in particular for high values of airmass (see Figure 3.2). The spectra have been straightened using eq. (3.1) for the differential atmospheric refraction. In particular, the following formula has been used

$$\Delta R(\lambda) = \frac{1}{27.19} \left[0.70337(n(\lambda) - 60.58) \tan \left(\arccos \left(\frac{1}{AM} \right) \right) 1000 \right] , \qquad (3.4)$$

that gives the shift ΔR in pixels (27.19 mas/pixel is the scale of the L27 camera, see Section 3.1.2) between a point of the spectrum at wavelength λ and the one corresponding to the wavelength $\lambda_0 = 1\mu m$. The constant 0.70337 takes into account the low temperature (T=11.5°C) and the low pressure (P=743.0 mbar) at Paranal. The expression for $n(\lambda)$ is

$$n(\lambda) = \frac{0.24}{\lambda^2} + \frac{0.10}{\lambda} + 60.24 , \qquad (3.5)$$

where λ is the wavelength in μm. Clearly, the curvature correction can be applied only after the dispersion relation for the wavelength calibration (see later, Section 3.1.3.6) is known. Panel d of Figure 3.4 presents the same Pluto/Charon spectra shown in panel c after curvature correction.

Another approach that we have used for the spectrum rectification consisted in the calculation, row by row, of the pixel shift between the peak position of the spatial profile of the spectrum at wavelength λ (x_λ) and that at wavelength $\lambda_0 = 1\mu m$ (x_{λ_0}). This means that we have assumed $\Delta R(\lambda) = x_\lambda - x_{\lambda_0}$. The peak position of the spatial profile has been determined by fitting for each row a Gaussian to the spectrum profile along the x-axis. This approach has been less successful than the previous one, because of the low accuracy in the determination of the peak position. This is may be due to the photon noise variation in the maximum per image row. The first method we have described does not request the calculation of x_λ since it consists in a translation by ΔR – see eq. (3.4) – of all the pixels at wavelength λ.

3.1.3.5   Spectrum Extraction

With the image processing steps completed up to now, the object spectrum can be extracted from the image by summing the target flux along the spatial dimension (x-axis in Figure 3.4), between the pixel limits x_1 and x_2. If the spatial profile were Gaussian, object limits separated by three times the full-width-half-maximum should enclose over 99% of the target radiation (Horne 1986). However, the AO profile is not exactly a Gaussian but a radially symmetric function with a central core, that can be approximated by a Gaussian, and extended wings that depend on the AO correction. This complicates the choice of the extraction limits. Indeed, if narrow object limits were used, the photometric accuracy of the spectrum would be sacrificed since an appreciable fraction of the target radiation is not counted. On the contrary, with wide object limits, the extracted spectrum becomes unnecessarily noisy as numerous pixels that contain very little target radiation and lots of sky background (the sky background flux has been subtracted but its noise amplitude remains in the result frame) are included in the extraction sum. An empirical test by changing

the extraction width has been performed. The object limits have been selected as those limits beyond which the object's signal does not improve and only the noise increases. This means that the choice of the target limits has been done by a compromise between statistical noise and photometric accuracy.

We used optimum extraction of the spectra (Horne 1986) to improve the signal-to-noise ratio over the aperture extraction using the algorithm EXTRACT/LONG implemented by MIDAS (http://www.eso.org/sci/data-processing/software/esomidas/doc/user/-98NOV/volb/node120.html). In this method two background signal windows, usually located to the left and right of the target spectrum, and one extraction window are selected in the spatial direction of the spectra. The algorithm calculates the background correction and performs the extraction assigning different weights to each line where the spectrum is extracted, following the method described by Horne (1986). This means that the flux target has not been summed along the spatial dimension, but added with weights that are lower for pixels farther from the peak of the spatial profile. This approach allowed us to consider the same object limits along the full wavelength range 1-5 μm. Indeed, once the spectrum is rectified (see Figure 3.4, panel d) in order to have the same peak position of the spatial profile along the full wavelength range (1-5) μm, the spatial range that needs to be considered to enclose the target flux in J-band is wider than that necessary for longer wavelengths. The behaviour observed in Figure 3.5, which has flux width inversely proportional to the wavelength, seems to contradict the Airy formula. Such behaviour is due to the high sky background in L- and M-bands. Adopting the same objects limits along the full wavelength range makes the target spectrum noisy. This effect is however balanced by the extraction method of Horne (1986). Using the same extraction window along the full wavelength range avoids uncertainties related with the adjustment of the spectra taken in separate bands.

Figure 3.5 shows the extraction widths chosen for the spectra observed in the night 5 August 2005. The extraction limits are the same for all spectra acquired in the same night, after aligning all of them in the same point. Table 3.3 lists the values adopted for the extraction limits of the spectra acquired in the second and last night of observations.
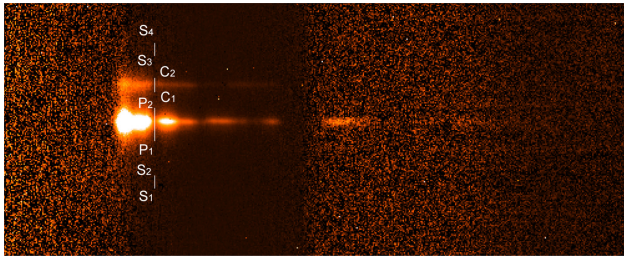

Figure 3.5: Extraction limits adopted for the spectra acquired in the night 5 August 2005. P_1 (C_1) and P_2 (C_2) are the Pluto (Charon) limits, while S_1, S_2, S_3 and S_4 delimit the two background signal windows. Wavelength increases from left (J-band) to the right (M-band).

Extraction limits	Night 5 August 2005	Night 7 August 2005
S_1	53	61
S_2	43	51
S_3	-53	-38
S_4	-63	-48
P_1	15	13
P_2	-11	-13
C_1	-24	-12
C_2	-35	-22

Table 3.3: The table lists the extraction limits adopted for the spectra acquired in the nights 5 and 7 August 2005 given in world coordiantes. P_1 (C_1) and P_2 (C_2) are the Pluto (Charon) limits, while S_1, S_2, S_3 and S_4 delimit the two background signal windows (see Figure 3.5).

3.1.3.6   Wavelength calibration

Once the spectrum is extracted from the bidimensional frame it is given in pixel units, so we have counts versus pixel position. A very important step in data reduction is the conversion of the pixel positions in wavelength units. This calibration is generally achieved using arc lamp calibration frames. Every morning, after the end of the night and with the telescope closed, spectroscopic lamp arcs are taken in each spectroscopic setup used during the night. These arcs are internal to CONICA and taken with an Argon lamp. The spectrum of such a lamp is a set of emission lines. The emission lines have known wavelengths and their positions in the calibration spectra can be measured. It is then possible to fit the relation between pixel position and wavelength using low-order polynomials. This relation, called *dispersion relation* $\lambda = p_x(y)$, is applied to the target spectra in order to calibrate them in wavelength space.

The wavelength calibration of the Pluto/Charon NACO data was particularly difficult since arc lamp spectra are not available to calibrate the strongly nonlinear dispersion of the prism. Indeed, at long wavelengths there are no visible arc lines, while at short wavelengths the lines are severely blended. Hence, atmospheric emission and absorption features were used as wavelength reference. In the top panel of Figure 3.6 the sky spectrum in counts versus pixel position is shown. This was obtained by subtracting the median filtered object frame along the y-axis from the original target frame. The L27 camera (see Section 3.1.2), with which the observations were performed, consists of 1024×1024 pixels and the range from 700 to 1024 pixels in the plot corresponds to the bottom part (long wavelength region) of the bidimensional spectrum shown in Figure 3.4. The sky emission spectrum in the M-band is shown in the bottom panel of Figure 3.6. In order to perform a comparison between the sky spectrum extracted from the NACO frames and the sky emission spectrum, calibrated in wavelength, it is necessary to convolve the former to the corresponding spectral resolution of NACO prism. In the figure the common features between the two spectra have been labelled. These are only some of the features chosen for the wavelength calibration of the NACO prism. The dispersion relation we have determined is the following

$$\lambda = 0.0001950999\,x^3 - 0.4337617231\,x^2 + 370.8366383889\,x - 72240.648299725 \ , \quad (3.6)$$

where λ is the wavelength in Å and x is the pixel position. In Appendix B the reference wavelengths and the associated pixel positions used to determine the dispersion solution of the NACO prism L27_P1 are listed.
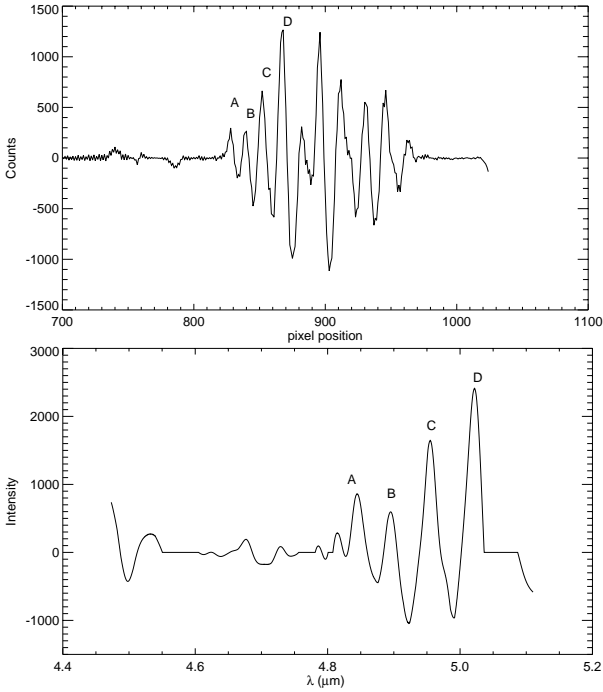
Figure 3.6: The sky spectrum obtained from the NACO frames in counts versus pixel position is shown in the top panel. In the bottom panel the sky-emission spectrum in the M-band is presented. The features common to the two spectra have been labelled.

3.1.3.7 Removing telluric and solar features

The aim is to remove the large number of telluric and solar features that appear in the target spectra. This is done by dividing the object spectrum with that of a solar analogue star. The solar analogue and the object have to be observed in the same night, with the same instrument setup, with roughly the same airmass and position angle and, if possible, consecutively. This is because the telluric features are variable with time, and are wavelength and airmass dependent. The position angle is required to be roughly the same to the one of the target in order to have the same light losses at the slit blades (due to atmospheric refraction). Secondly, the object and solar analogue data should be reduced in the same way and with the same calibration frames. In our case, spectra of the nearby

solar analogue star HD 162341 (G2/G3V), recorded approximately every 1.5 hour, were obtained in order to remove simultaneously both the telluric and solar features from the Pluto and Charon spectra. In this way, each Pluto/Charon observation had an associated set of "before" and "after" calibration star observations acquired under similar sky and airmass conditions and for identical instrument and AO settings.

Figure 3.7: Example of a Pluto/Charon observation affected by electronic noise in the L- and M-band of the detector.
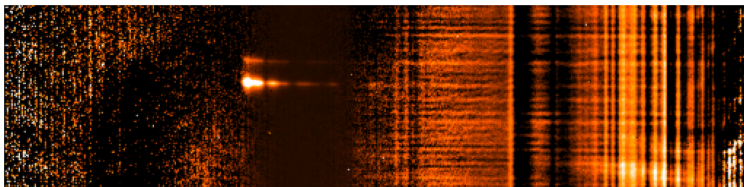
Finally, the spectra acquired in the second and last night of observations were averaged, due to their better quality, especially in the L- and M-bands, compared to those of the other two nights. Indeed, the spectroscopic measurements acquired in the first night of observations suffer from bad seeing conditions, with seeing up to 2.2″(see Table 3.1), and operational problems. Most of the observations obtained in the third night are affected by electronic noise in the L- and M-range of the detector. Figure 3.7 shows an example of electronic noise in L- and M-band range, the reason for which is unknown.

In order to minimize the light losses in the short wavelength region (due to atmospheric refraction), we obtained the final spectra of Pluto and Charon by averaging the JHK spectra obtained at low values of airmass ($AM \leq 1.23$). The upper limit of 1.23 for the airmass has been determined taking into account the diffraction limit of the telescope and the differential atmospheric refraction in J- and H-bands. In the L- and M-bands we averaged all of the useful spectra taken up to a maximum airmass of 2.47 in the L-band and 1.25 in M-band. Useful spectra are those not affected by the noise pattern described above. This pattern is sometimes only present in the M-band range of the detector and does not affect the L-band range. In this case only the M-band has been cut out.

3.1.3.8   Albedo calibration

The extracted spectra were normalized using published values for the geometric albedo at fixed wavelengths. Specifically, Pluto's spectrum was normalized in the wavelength range (1.9-2.1) μm to 0.57, a value extracted from the Pluto IRTF spectrum of Olkin et al. (2007). The IRTF spectrum was scaled to the HST spectrum of Pluto (Grundy and Buie 2002), measured separately from its satellite Charon and obtained averaging the NICMOS spectra taken at different Pluto longitudes. It is important to stress that in the range (1.9-2.1) μm Pluto's spectrum does not present any absorptions but shows continuum level. The normalization to published values of geometric albedo should not be done in a wavelength range where the spectrum presents deep absorption. Indeed there are several physical effects, such as grain size of the absorbing element and its abundance, but also instrumental effects, like spectral resolution, that contribute to modify the absorption

depth. Using this normalization, the averaged L- and M-band geometric albedo of Pluto are in agreement with Spitzer Space Telescope (formerly known as the Space Infrared Telescope Facility, or SIRTF) results obtained by J. Emery (priv. comm.). These are geometric albedo measurements of Pluto obtained by the Infrared Array Camera (IRAC) at 3.6 and 4.5 μm. The geometric albedo retrieved with IRAC at 3.6 μm is equal to 0.16-0.17 while the one at 4.5 μm varies with the rotational phase of Pluto from 0.27 to 0.38. Averaging the geometric albedo of the NACO Pluto spectrum along the IRAC L- and M-band windows, we obtain a value of 0.16 and 0.29 at 3.6 and 4.5 μm, respectively. The choice of this normalization resides on the guarantee that at low values of airmass (AM less than 1.23) we do not have light losses in K-band due to the slit acquisition technique (see Section 3.1.2).

We have tried to perform the normalization of NACO spectrum in L-band according to the photometry of Spencer et al. (1990) at 2.94 μm. Spencer et al. (1990) present photometry of the Pluto/Charon system unresolved. Charon's contribution in the range between 2.9 and 3.2 μm to the Pluto/Charon system is almost zero (see Section 3.3.2.3), making this normalization acceptable. However, in this case the averaged L-band geometric albedo of Pluto is not in agreement with the SPITZER albedo value. Also, we have a good agreement between NACO and Keck (Olkin et al. 2007) spectra in the range from 2.8 to 3.2 μm, but a huge difference between the IRTF and NACO spectrum in K-band. This difference does not correspond to a plausible light loss of NACO since the slit acquisition has been performed in the K-band.

Charon was normalized in the range (2.2-2.3) μm to 0.31, in agreement with the HST/NICMOS Charon spectrum by Buie and Grundy (2000).

The spectra were binned using a wavelength step $\delta\lambda = 0.005$ μm. In Figures 3.8 and 3.9 we present the NACO reflectance spectra obtained for Pluto and Charon, respectively.

The standard deviation (STD) of Pluto's and Charon's spectra as function of wavelength has been computed using the method described below.

JHK-bands After selecting only the spectra with low values of AM (AM $\leq$ 1.23), we have averaged those with similar values of AM and position angle (PA). Each spectrum has been median filtered and normalized in the K-band as described above. These spectra were averaged in order to obtain the final target spectrum in the JHK range. The standard deviation (STD) has been computed as

$$STD = \sqrt{\frac{1}{N-1} \sum_{j=0}^{N-1} (y_j - \bar{y})^2} \,, \qquad (3.7)$$

where N is the total number of spectra considered, j identifies each spectrum considered (y_j) to obtain the averaged ($\bar{y}$) one. In this way we obtain the STD as function of wavelength.

L- and M-bands After selecting the useful spectra in the L-band (as described in the previous subsection), we have averaged those with similar AM and PA. After filtering each spectrum, we have overlapped each of them with the averaged JHK spectrum obtained at
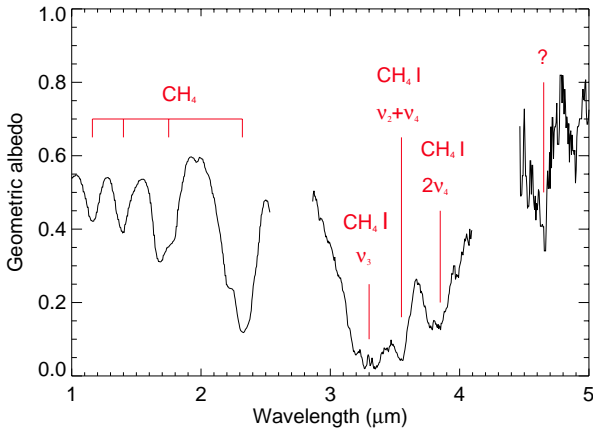
Figure 3.8: Pluto's spectrum in the wavelength range (1-5) μm. The species responsible for the absorption bands detected in Pluto's spectrum are marked. No object flux is measured in the atmospheric absorption bands at 2.50-2.86 and 4.10-4.46 μm.

Figure 3.9: Charon's spectrum in the wavelength range (1.0-4.1) μm. No object flux is measured in the atmospheric abso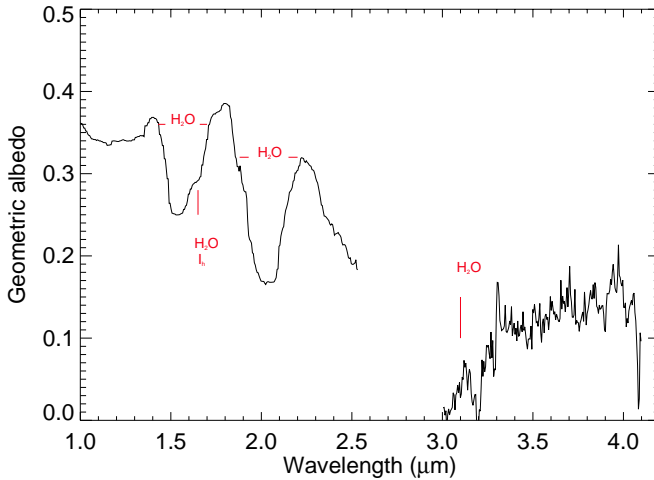rption bands at 2.5-3.0 μm. The species responsible for the absorption bands detected in Charon's spectrum are marked.

low values of airmass. This allows us to avoid uncertainties related with the normalization. After normalizing each spectrum, we have computed the averaged spectrum and the STD – see eq. (3.7). In the wavelength range (1.0-2.5) μm the standard deviation (STD) of Pluto's and Charon's spectra is around 0.04 and 0.01, respectively, while it increases in the range 1.80-1.95 μm due to the presence of strong lines of telluric H_2O. In the L-band, from 3.1 to 4.0 μm, the STD is about 0.05 for Pluto and 0.09 for Charon. These values increase at the atmospheric band edges due to the strong telluric absorptions. In the M-band, between 4.6 and 4.7 μm, the STD of Pluto has values around 0.15, much smaller than at the edges of the band.

3.2 Spectroscopic Analysis

In this section we present a qualitative description of the Pluto and Charon spectra, focusing the attention on both the known compounds and the unknown features. The quantitative analysis of the spectra will be described in the modeling section (Section 3.3).

3.2.1 Pluto

Published spectra of Pluto in the wavelength range (1.0-4.2) μm have established the presence of CH_4 ice on Pluto's surface, identified first by Cruikshank et al. (1976). This is confirmed by our NACO results. Indeed, in the wavelength range (1.0-2.5) μm our spectrum is dominated by prominent CH_4 features at 1.16, 1.40, 1.67, 1.79, 2.20, and 2.32 μm (Figure 3.8). The geometric albedo of pure CH_4 in the range (1.2-2.5) μm is shown in Figure 2.12 for comparison. Also the L-band spectrum (2.9-4.1) μm is characterized by CH_4 absorption bands around 3.30, 3.55, and 3.80 μm corresponding to ν_3, $\nu_2 + \nu_4$, and $2\nu_4$ vibrational transitions, respectively (Grundy et al. 2002a). Because of the low spectral resolution of the NACO prism, it is not possible to detect the CO ice absorption bands at 1.579 and 2.354 μm (Owen et al. 1993; Douté et al. 1999) and the N_2 feature at 2.149 μm first seen by Owen et al. (1993) (see Figure 1.11). Our low spectral resolution in the JHK bands does not allow differentiation between pure CH_4 and CH_4 diluted in N_2, which can be distinguished spectroscopically by a small shift in the peak frequencies of the bands, first seen in the spectrum of Triton (Cruikshank et al. 1993). From laboratory measurements by Quirico and Schmitt (1997b) of CH_4 diluted in β-N_2 at 44K compared with those of pure CH_4 at 43.5K, this shift varies, in the wavelength range (1-2.5) μm, from 0.003 to 0.005 μm. A shift of this magnitude is smaller than or comparable with the wavelength bin (selected to match the minimum resolution of the prism), so it is undistinguishable in our data.

Regarding the M-band, our NACO spectrum reveals the presence of a previously unknown and thus unidentified absorption band around 4.6 μm, indicated by a question mark in Figure 3.8. This absorption, a first detection at the limit of the instrumental capability that must be confirmed by further observations, could be related to the presence of CO ice on Pluto's surface. Indeed, CO ice displays an absorption band around 4.67 μm in laboratory spectra (Palumbo and Strazzulla 1993). Also, CO ice is known to be present on the surface of the dwarf planet from the short wavelength region (Douté

et al. 1999), with highest abundance on the anti-Charon hemisphere[1] (Grundy and Buie 2001). Another possible explanation for the 4.6-μm feature is the presence of nitriles on Pluto. Nitriles are organic compounds characterized by a triple bond connecting carbon and nitrogen. They are predicted to precipitate to the surface in photochemical models of Pluto's atmosphere (Krasnopolsky and Cruikshank 1999). The nitrile band near 4.6 μm varies somewhat in position, depending on the environment in which the molecule occurs and the other atom or functional groups attached to the C-atom on the side opposite the N-atom (Cruikshank et al. 1991). Several nitriles, in pure form, have been studied in laboratory like acetonitrile (CH_3CN), propionitrile (CH_3CH_2CN), acrylonitrile (CH_2CHCN), hydrogen cyanide (HCN), cyanogen (C_2N_2), cyanoacetylene (HC_3N), dicyanoacetylene (C_4N_2), and cyanopropyne (CH_3C_3N), presenting (at 35K) absorption bands at 4.450 μm, 4.506 μm, 4.488 μm, 4.843 μm, 4.619 μm, 4.405 μm, 4.454 μm, 4.396 μm, respectively (Masterson and Khanna 1990; dello Russo and Khanna 1996). The 4.6-μm absorption band in Pluto's spectrum could be a blend of more than one individual molecular species. Moreover, we do not have any information about the form in which nitriles might occur on Pluto's surface, whether in pure form or diluted in a nitrogen matrix.

3.2.2   Charon

Figure 3.9 shows the NACO spectrum of Charon, the first one measured also in the L-band. The spectrum confirms the presence on Charon's surface of H_2O ice, by the absorption bands at 1.5 and 2.0 μm, together with the 1.65-μm feature diagnostic of crystalline water ice (Brown and Calvin 2000). For comparison the geometric albedo of crystalline water ice in the range (1-2.5) μm is shown in Figure 2.10. Because of the low spectral resolution it is not possible to detect in the NACO spectrum the 2.21-μm feature attributed to hydrated ammonia (Cook et al. 2007).

From the presence of strong absorption bands of H_2O ice in the short wavelength region, it is not surprising that a very broad water ice signature is found in the L-band part of Charon's surface spectrum.

3.3   Modeling

A quantitative analysis of the Pluto and Charon spectra was performed using the routine based on the scattering radiative transfer model of Hapke (1993) described in Chapter 2. Sections 3.3.1 and 3.3.2 describe the results obtained from modeling the Pluto and Charon spectra, respectively.

3.3.1   Pluto

3.3.1.1   The best-fitting model

Because of the low spectral resolution of NACO spectrum in JHK bands and the light losses due to differential atmospheric refraction in J- and H-bands (see Section 3.1), IRTF

---

[1]The heterogeneity of Pluto's surface has been investigated first by Buie and Fink (1987), by comparing spectra obtained at different rotational phases of the dwarf planet.
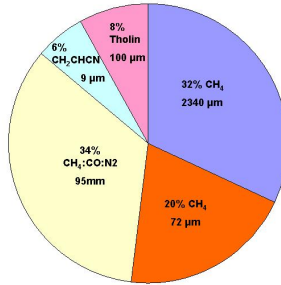
Figure 3.10: Geographical terrain units in our best-fit model.

observations of Pluto obtained in 2002 at high spectral resolution over the wavelength range (1.0-2.4) μm (Olkin et al. 2007) were combined with our NACO spectrum of Pluto in the L- and M-bands to be used as input for the modeling. The best-fitting model of this composite Pluto spectrum was obtained with an areal mixture of five-terrains consisting of CH_4 with two different grain sizes, CH_4 and CO ice diluted in N_2 (CH_4:CO:N_2), CH_2CHCN, and Titan tholin (see Figure 3.10). The abundance and grain size of each component in the mixture are free parameters but for the CH_4:CO:N_2, which are based on the wavelength shift of the methane ice bands of high resolution Pluto's spectra. For more details on the abundance and grain size of each element in the mixture the reader is reported to Table 3.4 while details on the optical constants used for each element in the modeling are reported in Table 3.5. The optical constants of CH_4:CO:N_2 were obtained as described by Douté et al. (1999). Since it is not possible to experimentally obtain the optical index spectra corresponding to all the potential values for the concentrations of CH_4 (C_{CH4}) and CO (C_{CO}) in solid nitrogen, Douté et al. (1999) consider three "pure" reference components. The first one is identified with pure N_2 ice, and the second and the third ones with methane and carbon monoxide initially diluted in the nitrogen matrix, but artificially normalized to unit concentration (Quirico et al. 1999). Douté et al. (1999) assume that, for each wavelength, the scalar product of the complex indices of N_2, of the diluted CH_4, and of the diluted CO by the vector [(1-C_{CH_4} -C_{CO}); C_{CH_4} ; C_{CO}] gives the optical constants of the mixture. Since there are no optical constants of carbon monoxide diluted in N_2 in the far-infrared wavelength range, we have considered pure CO, for which we do not have uniform coverage of optical constants in the range between 1 and 5 μm (see Table 3.5). In the short wavelength range the difference between pure CO and CO diluted in N_2 is a light shift of the 2ν band peaking around 2.352 μm, amounting to 0.3 nm for CO isolated in β-N_2, the phase at which N_2 is expected on Pluto's surface (see Section 1.5.1). A shift of this magnitude is not detectable at the spectral resolution of NACO measurements. Moreover, no effect of CO concentration was observed in the β-phase of N_2 ice for a CO concentration lower than 4.2% (Quirico and Schmitt 1997a).

Following the approach of Olkin et al. (2007), we assumed a cosine asymmetry factor ξ equal to -0.3. Buie et al. (1997) showed Pluto's phase coefficient to be nearly identical to that of Triton, and -0.3 is the ξ value found by Voyager for Triton (Hillier et al. 1994). The

Model	Abundance(%)	Grain size (μm)
CH$_4$	32^{+3}_{-2}	2340^{+770}_{-240}
CH$_4$	20^{+1}_{-4}	72^{+67}_{-17}
CH$_4$:CO:N$_2$	34^{+1}_{-9}	95000^{+25500}_{-13000}
CH$_2$CHCN	6^{+0}_{-2}	9
Titan Tholin	8^{+2}_{-0}	100^{+135}_{-35}

Table 3.4: Units in the best-fit model of the IRTF+NACO data.

Element	Optical constants	Wavelength range
CH$_4$	Grundy et al. (2002b)	(0.65-4.91) μm
CH$_2$CHCN	dello Russo and Khanna (1996)	(2-5) μm
Titan Tholin	Khare et al. (1984)	(0.02-4.88) μm
N$_2$	Quirico et al. (1996)	(2.06-2.19) μm
CH$_4$:N$_2$	Quirico and Schmitt (1997b)	(1.00-5.00) μm
CO	Schmitt et al. (1992)	(1.43-2.50) μm
	Ehrenfreund et al. (1996)	(4.55-5.00) μm
C$_2$N$_2$	dello Russo and Khanna (1996)	(2-5) μm

Table 3.5: Optical constants of the materials used to perform Pluto's modeling.

values assumed for surface roughness and compaction parameter are 14°, by analogy with Triton, and 0.5 (Olkin et al. 2007), respectively. The contribution to Pluto's geometric albedo of each single terrain considered in the modeling is shown in Figure 3.11. In the range between 1 and 2 μm we assumed the reflectance spectrum of CH$_2$CHCN to be flat, since the optical constants of dello Russo and Khanna (1996) cover the wavelength range 2-5 μm only (see Table 3.5). Figure 3.12 shows the comparison between Pluto's spectrum (solid line) and our best-fit model (dashed line). This model may not be a unique solution and depends on the considered surface components. Figure 3.13 shows the comparison between the averaged NACO spectrum (solid line) together with its standard deviation (STD) as function of wavelength (dash-dot-dot-dot lines) in the range (1-2.5) μm and the best-fit model (dashed line) degraded to the same spectral resolution as the NACO observations. This was done by convolving the high spectral resolution model shown in Figure 3.12 with a gaussian profile with FWHM of 0.05 μm in the (1-2.5) μm wavelength range, corresponding to a spectral resolution of 35.

The synthetic spectrum reproduces all the main features of the observed spectrum. The deviation of the model from the observed spectrum is within the errors, although the model deviates from the observations in the continuum regions around 1.0, 1.3, and 1.5 μm. The reason for this deviation is the light loss of the NACO spectrum due to atmospheric refraction (see Section 3.1). The comparison between the IRTF observations of
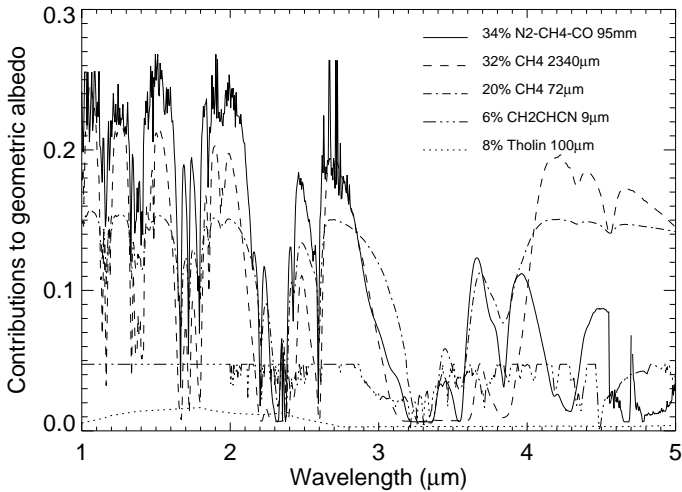
Figure 3.11: Contributions of each model terrain to Pluto's geometric albedo spectrum.
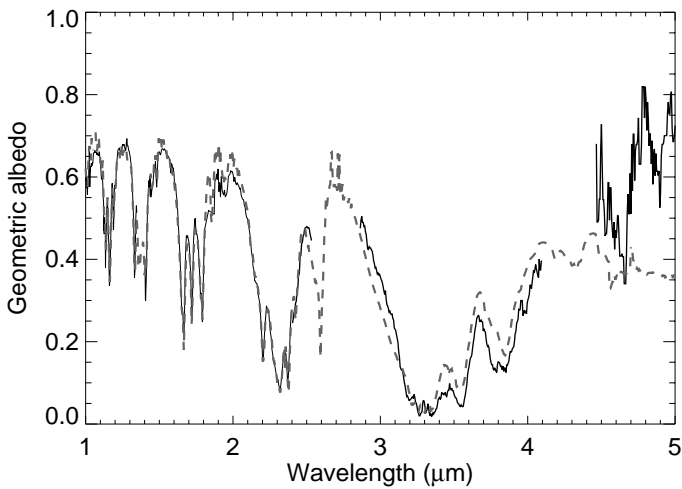
Figure 3.12: Pluto's spectrum (solid line) obtained by combining the 2002 IRTF observations (Olkin et al. 2007) at high spectral resolution over the wavelength range (1.0-2.4) μm and the NACO spectrum in L- and M-band is shown. Overplotted is the best-fitting model (dashed curve).
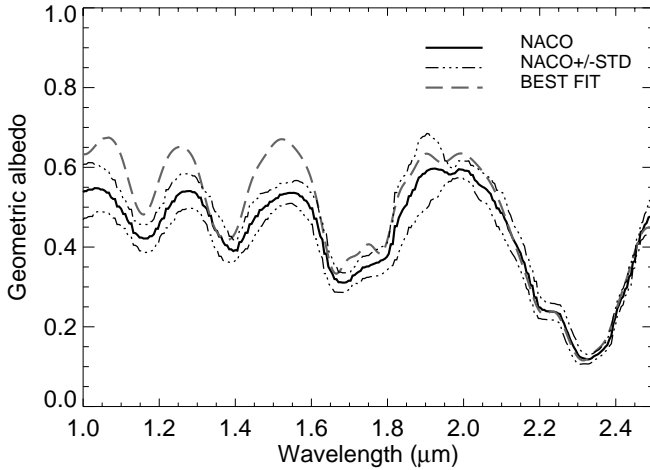
Figure 3.13: Comparison between the averaged NACO spectrum of Pluto (solid line), including STD (dash-dot-dot-dot line), and the best-fitting model (dashed line) degraded to the same spectral resolution as the NACO observations over the wavelength range (1-2.5) μm.
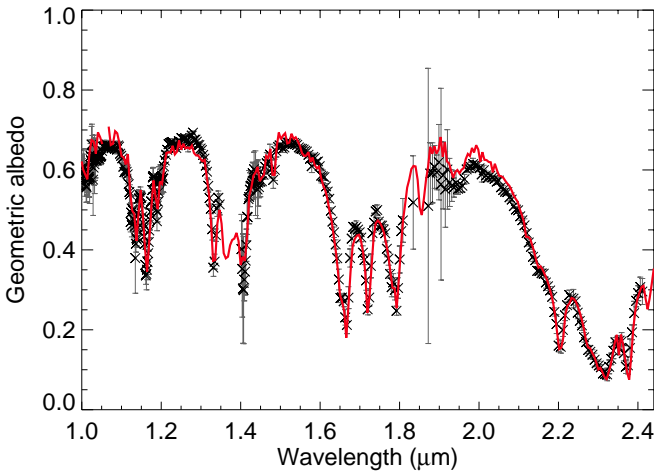
Figure 3.14: IRTF observations (black crosses) (Olkin et al. 2007) compared with the our best-fitting model (red solid line) over the wavelength range (1.0-2.4) μm.
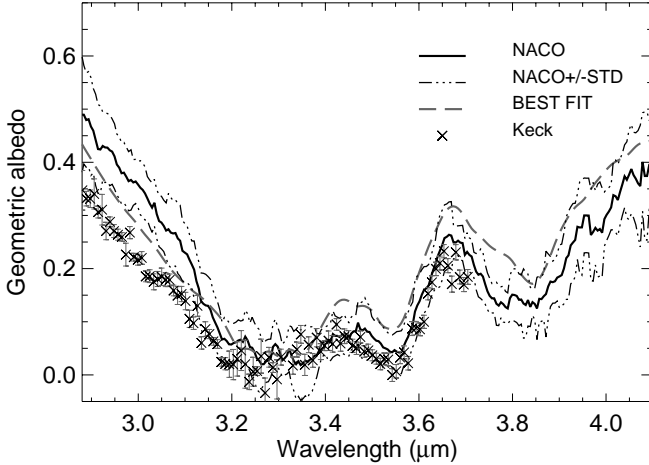
Figure 3.15: Comparison between the averaged NACO spectrum of Pluto (solid line), including STD (dash-dot-dot-dot line), and the best-fitting model (dashed line) over the wavelength range (2.9-4.1) μm. Pluto's measurements obtained with the Keck telescope in 2001 (crosses) (Olkin et al. 2007) are overplotted.

Pluto obtained in 2002 (Olkin et al. 2007) at high spectral resolution (see Figure 3.14) and the modeled spectrum shows that our model reproduces correctly the measured depths of the CH_4 absorption bands. The presence of CH_4 diluted in N_2 reproduces the nitrogen absorption band at 2.149 μm and takes into account the coexistence of pure and diluted methane on the surface of Pluto (Douté et al. 1999). Difficulties in fitting the albedo at 2.32 and 2.37 μm arise because of the saturation of the CH_4 absorption bands at these wavelengths. This problem was solved by including CH_2CHCN and Titan tholin as continuum scatterers. In the short wavelength region acrylonitrile, as well as Titan tholin, displays a high, almost neutral geometric albedo which increases the reflectance around 2.32 and 2.37 μm. Figure 3.15 shows the averaged NACO spectrum (solid line) together with its standard deviation (STD) as function of wavelength (dash-dot-dot-dot lines) compared with our best-fit model (dashed line) in the range (2.9-4.1) μm. It is possible to verify that the deviation of the model from the observed spectrum in the L-band is within the errors, although with systematic deviations depending on wavelength.

3.3.1.2 Model sensitivity

In order to determine the uncertainties of the retrieved best-fitting model, we have performed a systematic study on the sensitivity of Pluto's synthetic spectrum to variations in the concentration and grain size of each element in the mixture. Because of the high STD of the NACO spectrum in the M-band, we have considered Pluto's spectrum, obtained combining IRTF and NACO observations, in the wavelength range between 1 and 4.1 μm.

First we have analysed the uncertainties on the abundances. The purpose is to see how the χ^2, that characterizes the goodness-of-fit, varies with changes in concentration ratios. This has been done for each element in the mixture using 1% step, and redistributing this percentage in equal parts to the other elements of the mixture. We consider as reference the χ^2 of the best-fitting model ($\bar{\chi}^2$) of Pluto's spectrum presented in the previous section (see Figure 3.10). The uncertainty for each concentration is given by the range of values within which the χ^2 differs from $\bar{\chi}^2$ by 4%. For example, in the case of C_{CH_4} (grain size equals to 72 μm), we have found that these limits are reached when we subtract or add 4% and 1%, respectively. Hence the uncertainty on C_{CH_4} is $^{+1\%}_{-4\%}$. Figure 3.16 shows the comparison between Pluto's observations and the best-fit model (gray dashed line) over the wavelength range (1-2.5) μm (top panel) and (2.8-4.1) μm (bottom panel). Overplotted are the synthetic spectra obtained considering in the mixture instead of 20% of pure methane with 72 μm grains, as in the best-fit, 16% (green dotted line) and 21% (violet dash-dot line). The three synthetic spectra do not present significant differences, representing in this way possible candidates for the best-fit of Pluto's spectrum.

The same approach has been applied for the grain size sensitivity, using 1 μm step size. It must be noted that the grain size of CH_2CHCN is not allowed to be decreased below 9 μm because of the limit imposed by the Hapke theory (since the grain size is approaching the wavelength of the radiation). The upper limit, instead, is strongly constrained by the M-band feature.

The uncertainties on the concentration and grain size of each element in the mixture are reported in Table 3.4 together with the best-fit values. It can be noticed that the abundances present few percent of uncertainty, while the grain size are less constrained. In this approach we have considered the goodness-of-fit as reference weighted with the STD of the spectroscopic measurements. We did not consider any other source of error.

3.3.1.3   Differences between 2005 and 2001 observations

Figure 3.15 shows the comparison between the NACO and Keck (Olkin et al. 2007) observations obtained in 2005 and 2001, respectively. The main difference between the two sets of data is the spectral slope between 2.9 and 3.1 μm. The NACO spectrum presents, even considering the STD, a slope that is steeper than that observed in 2001. One could hypothesize that the difference between the NACO and Keck data is due to a wrong removal of Charon's contribution from the measured reflectance spectra of Pluto/Charon system obtained with Keck (see the introduction to this chapter). This can be excluded since the new NACO observations show that the contribution of Pluto's moon to the unresolved binary system in the range between 2.9 and 3.1 μm is almost zero. This will be better discussed in Section 3.3.2.3.

This spectral difference can be due to viewing geometry since geographical regions at different longitudes and latitudes come into view. The NACO spectrum was obtained by averaging the spectra acquired in the second and last night of the observing run (see Section 3.1), corresponding to a sub-Earth longitude of 64° and 178°, respectively (see Table 3.1). The spectra of the two opposite hemispheres of Pluto do not show any significant difference (the variation is inside the STD) in the wavelength range between 2.9 and 3.7 μm (see Figure 3.17). This evidence, together with the fact that Keck spectrum refers to a sub-Earth longitude of 198°, near the one covered by NACO on 7 August 2005, makes
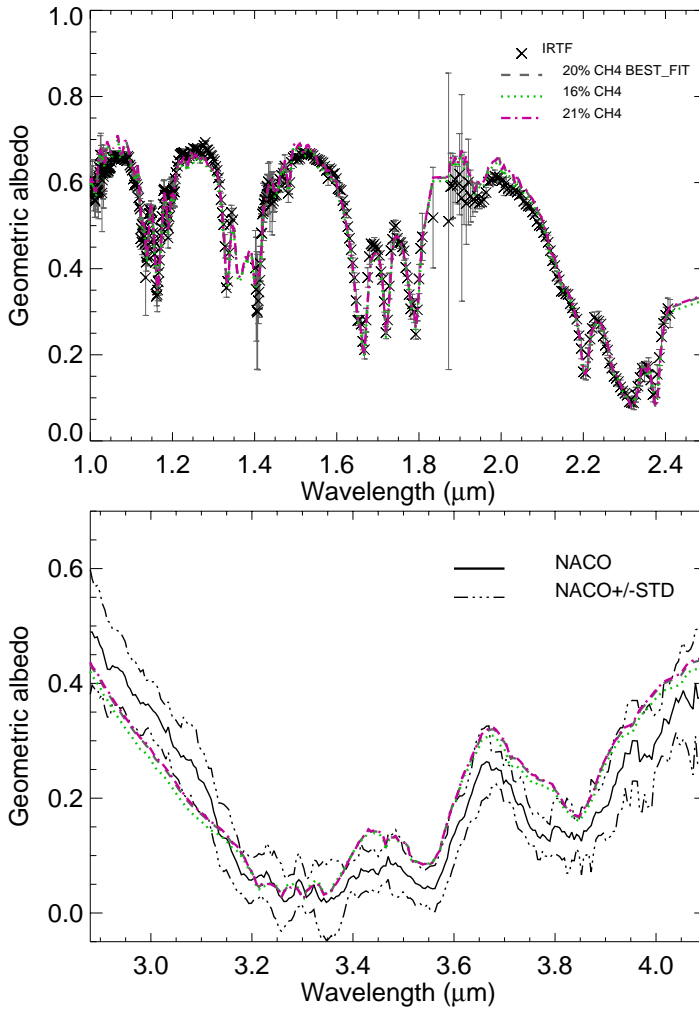
Figure 3.16: Modeling results for different concentrations of pure CH$_4$ with 72 μm grains, compared with the IRTF (top panel) and NACO (bottom panel) spectrum of Pluto. Gray dashed line represents the best-fitting model of Pluto's spectrum. Violet dash-dot line and green dotted line represent the synthetic spectra obtained from the best-fit model adding and subtracting to C_{CH_4} 1% and 4%, respectively.
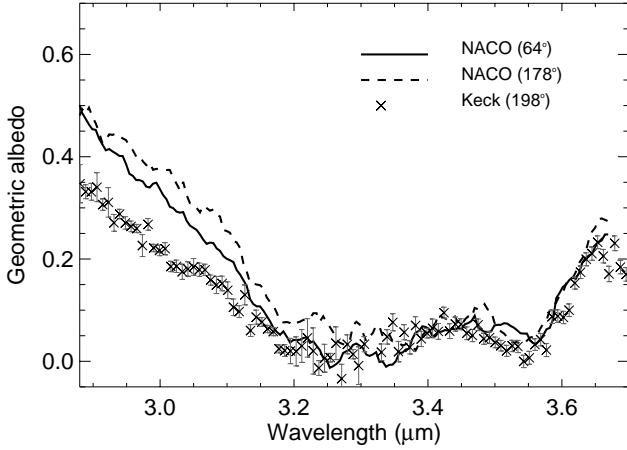
Figure 3.17: Near-infrared spectra of the two opposite hemispheres of Pluto (solid and dashed lines) obtained with NACO in 2005 compared to the observations obtained with the Keck telescope (crosses) in 2001 over the wavelength range (2.88-3.7) μm.
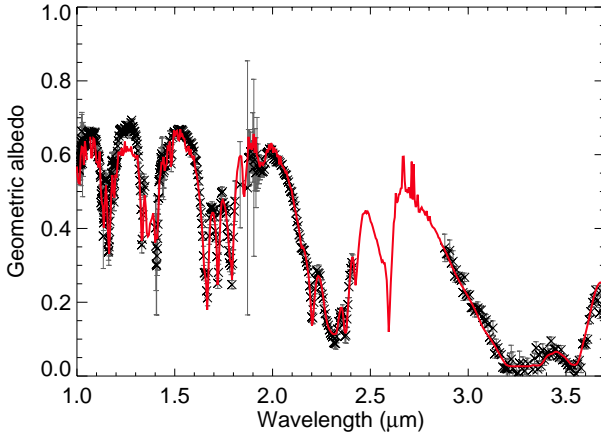
Figure 3.18: IRTF and Keck observations (Olkin et al. 2007) over the wavelength range (1.00-2.40) μm and (2.88-3.70) μm, respectively (black crosses). Overplotted (red solid line) is our model of these observations.

Model	Abundance(%)	Grain size (μm)
CH_4	37	764
CH_4:CO:N_2	34	95000
Titan Tholin	29	23

Table 3.6: Units in the best-fit model of the IRTF+KECK data.

longitudinal changes in the ice composition very unlikely to justify the slope difference between NACO and Keck spectra. The spectral change between NACO and Keck data might be compatible with variations in the observed surface latitude. Another possible explanation for the spectral difference between NACO and Keck spectra is the temporal change of Pluto's surface. These scenarios are discussed in greater detail in Section 3.4.

Another important point is the nature of the surface elements responsible for this slope variation. Many ices, such as H_2O, but also complex organics such as tholin-type radiolysis/photolysis residues, absorb strongly in the region between 2.9 and 3.1 μm (Khare et al. 1984, 1989; McDonald et al. 1994). Also, this slope is known to be diagnostic for the ratio between pure methane and methane diluted in nitrogen, since the spectrum of pure methane presents a steeper slope than methane diluted in nitrogen (Olkin et al. 2007). This implies that a higher CH_4-CH_4:N_2 ratio than the one used to model the Keck spectrum would fit better the NACO observations. This latter approach was taken into consideration for this work. The best-fit model of the IRTF and Keck data in the wavelength range (1.0-2.4) μm and (2.9-3.7) μm, respectively, was obtained with a three terrain unit model: CH_4 diluted in N_2, pure CH_4, and Titan tholin (Figure 3.18). For details on the best-fit model of the IRTF and Keck data, the reader is referred to Table 3.6. These values are different from those reported by Olkin et al. (2007) because of the use of a different phase function. Knowing of the coexistence of pure and diluted methane at the surface of Pluto (Douté et al. 1999), we tried to get a better fit of the slope of the NACO data by increasing only the abundance of pure methane in the mixture while maintaining that of diluted methane. Figure 3.19 shows the effect on the spectral model for various fractions of pure methane and using different grain sizes. In particular, it is evident that a model consisting of 34% of diluted methane and 37% of pure CH_4 (green dashed line) would not match the slope of the NACO spectrum of Pluto. Adding 15% of pure methane results in a steeper slope, which further increases when the grain sizes are reduced (see blue dash-dot and gray long dashed lines in Figure 3.19). However, Figure 3.19 shows that grain sizes smaller than 70 μm produce a synthetic spectrum (violet dash-dot-dot-dot line) that is too narrow around 3.3 μm absorption dip and at the same time, it is too high around 3.55 and 3.80 μm.

3.3.1.4   The new feature in Pluto's spectrum

As mentioned in Section 3.2.1, the compound that could contribute significantly to the absorption band at 4.6 μm is CO ice, which has an absorption band around 4.67 μm. Figure 3.20 shows the comparison between the NACO spectrum (black solid line) and the best-fitting model (gray dashed line), at the same spectral resolution as the observations. The insert box in Figure 3.20 shows the contribution of the CO ice absorption band at 4.67 μm to the 4.6-μm feature in Pluto's spectrum over the wavelength range 4.4-5 μm.
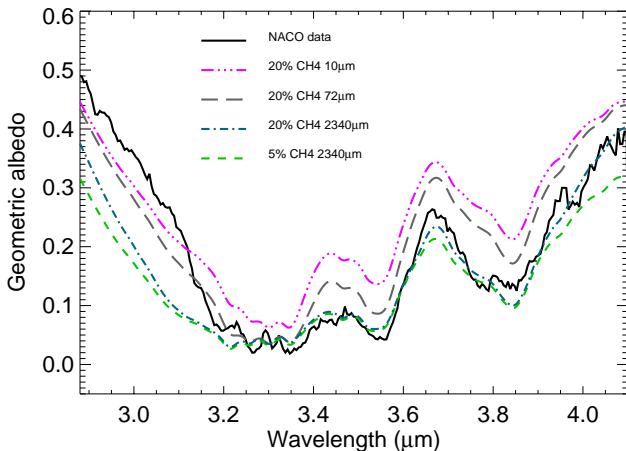
Figure 3.19: Modeling results for different concentrations of pure methane and different grain sizes, compared with the NACO L-band spectrum of Pluto. By default, all the models assume 32% of pure CH$_4$ with 2340 μm grain size, 34% of CH$_4$ and CO ice diluted in N$_2$ with 95 mm grains, 6% of CH$_2$CHCN with 9 μm grains, and 8% of Titan tholin at 100 μm grains. Only the percentage of pure methane ice and its grain sizes are varied. The sensitivity of the L-band spectrum to changes in the grain size of pure CH$_4$ is shown in the figure by some examples.

The comparison between NACO spectrum (black solid line) and the best-fitting model obtained by including (gray dashed line) and removing (red dash-dot line) the absorption band of CO ice at 4.67 μm is shown as well.

Another species that could contribute is CH$_3$D. The laboratory reflectance spectrum of pure CH$_4$ shows two absorptions, at 4.34 and 4.56 μm (see dashed and dash-dot lines in Figure 3.11). These absorptions do not correspond to any known CH$_4$ vibrational transition, and were tentatively attributed to CH$_3$D (Grundy et al. 2002b). Figure 3.20 shows the contribution of the 4.56-μm absorption of CH$_3$D to the fit of the observed 4.6-μm feature in Pluto's spectrum, presenting the comparison between the NACO spectrum (black solid line) and the best-fit model obtained by including (gray dashed line) and removing (green dotted line) the absorptions due to CH$_3$D. It is clear that the contribution of CH$_3$D to the Pluto feature in the M-band is almost negligible.

We investigated also the possibility that nitriles might explain the 4.6-μm feature in the Pluto spectrum. Among the several nitriles studied in the laboratory (see Section 3.2.1), those having absorption bands near 4.6 μm are CH$_2$CHCN, C$_2$N$_2$, and CH$_3$CH$_2$CN. In spite of the fact that the width of the Pluto's band suggests that it arises from a mixture of several different nitriles, we preferred to consider in the modeling only those having a band near 4.6 μm. This is due to the fact that it is difficult to establish a reliable continuum level around the 4.6-μm in the NACO Pluto's spectrum. Hence, the actual width of the absorption at 4.6 μm remains uncertain, while its maximum depth seems to be better de-
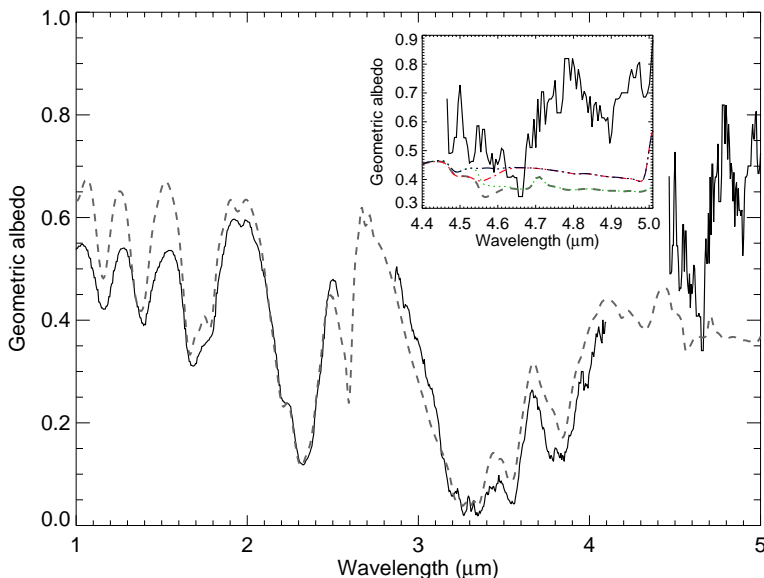
Figure 3.20: Pluto's spectrum (black solid line) obtained by NACO with the best-fitting model (dashed gray curve), at the same spectral resolution as the observations, over the wavelength range (1-5) μm. In the insert box the comparison between NACO spectrum (black solid line) and the best-fitting model obtained by including (gray dashed line) and removing (red dash-dot line) the absorption band of CO ice at 4.67 μm over the wavelength range 4.4-5 μm is shown. The best-fitting model obtained after removing the contribution of CH_3D at 4.34 and 4.56 μm (green dotted line) is also shown. The blue dash-dot-dot-dot line represents the best-fitting model considering the contribution of CH_2CHCN only.

fined. In the modeling, we have investigated the effects of the mixture of both CH_2CHCN and C_2N_2, while CH_3CH_2CN was not taken into account because of the absence of optical constants. We found that acrylonitrile (see Figure 3.11) is the only nitrile having an absorption around 4.6 μm that also gives a satisfactory fit to Pluto's spectrum in the short wavelength region. However, the introduction of CH_2CHCN results only in a weak absorption (weaker than the feature detected), and furthermore this absorption is located to the "left" (4.5 μm) of the detected 4.6-μm Pluto band (see Figure 3.20, blue dash-dot-dot-dot line in the insert box). Adding C_2N_2 in the mixture, the model diverges from the observed spectrum around 3.3 μm with albedo values higher than those observed.

3.3.2   Charon

3.3.2.1   The "standard model"

One of the best spectroscopic models proposed for Charon is the "standard model" by Buie and Grundy (2000). The model assumes an intimate mixture of 60% H_2O with 100 μm grain size and 40% of a neutral continuum absorber with 70 μm grains. The Hapke parameters adopted by Buie and Grundy (2000) are the following: $h = 0.01$, $B_0 = 0.06$ and $\theta = 20°$. For $P(g)$ (see Section 2.2.1) a two-parameter double Henyey-Greenstein function with asymmetry 0.615 and forward weight equals to 80% has been used. Any species, such as carbon black, is effectively neutral if at all wavelengths its grains have single scattering albedos considerably lower than those of the H_2O grains. The optical constants of the absorber were calculated by Buie and Grundy (2000) in the wavelength range (0.44-2.6) μm (see Table 3.7) in order to match the HST/NICMOS data from 1.4 to 2.5 μm. The necessity of computing optical constants for the spectrally neutral continuum absorber derives from the difficulty to duplicate Charon's albedo contrast between 1.8 and 2.2 μm at the same time with the water ice bands at 1.6 and 2.0 μm. This is due to the fact that the absorption coefficients of H_2O are quite similar at 1.8 and 2.2 μm (Grundy and Schmitt 1998). Only at extremely large grain sizes H_2O ice presents a lower albedo at 2.2 than at 1.8 μm, but large grains are ruled out by the shapes of the H_2O absorption bands at 1.6 and 2.0 μm. Evidently the absorption of Charon's continuum absorber must increase beyond 2 μm. These evidences brought the conclusion that in order to match Charon's spectrum, it is necessary to include together with H_2O something that is blue at near-infrared wavelengths, is abundant in the outer Solar System, and has little if any spectral activity at visible wavelengths, where spectra of icy satellites uniformly lack strong spectral features (Buie and Grundy 2000). Several materials have been found with these characteristics, such as kaolinite or montmorillonite, and approximate fits can be found using each of these material mixed with H_2O, although none is without problem. The goal of the "standard model" is to provide a model that would permit more accurate removal of Charon's contribution from combined Pluto/Charon observations (see the introduction to this chapter).

3.3.2.2   Extended "standard model" in the L-band

We extended the "standard model" beyond 2.6 μm, assuming that the neutral absorber has a flat spectrum in the range from 2.6 to 4.1 μm (with an absorption coefficient of 822 cm^{-1}). Figure 3.21 shows Charon's spectrum (solid line), normalized in the wavelength range (2.2-2.3) μm to 0.27, corresponding to Charon's reflectance at 1° phase angle, named A_1 in agreement with Buie and Grundy (2000). The figure also shows the comparison between the NACO spectrum of Charon and the "standard model" extrapolated beyond 2.6 μm (dashed line) in the wavelength range (1.0-4.1) μm. As for Pluto, the model deviates from the observations in the short wavelength region between 1.0 and 1.4 μm because of the light loss in the NACO spectrum due to the atmospheric refraction. Figure 3.22 shows the average Charon spectrum (solid line) together with its standard deviation (STD) as function of wavelength (dash-dot-dot-dot lines) compared with the model (dashed line) in the wavelength regions (1.0-2.5) μm (top panel) and (3.0-4.1) μm (bottom panel). The deviation of the extrapolated "standard model" from the NACO data

Wavelength (μm)	Absorption cm^{-1}	Imaginary index k
0.44	220	7.7×10^{-4}
0.55	157	6.9×10^{-4}
1.90	105	1.6×10^{-3}
1.93	150	2.3×10^{-3}
2.08	150	2.5×10^{-3}
2.15	280	4.8×10^{-3}
2.27	220	4.0×10^{-3}
2.35	300	5.6×10^{-3}
2.60	800	1.7×10^{-2}
2.95	822	1.9×10^{-2}
3.50	150	0.4×10^{-2}
3.95	100	0.3×10^{-2}

Table 3.7: The optical characteristics of the standard continuum absorber for Charon are reported. The optical constants have been computed by Buie and Grundy (2000) in the range (0.44-2.6) μm. Beyond 2.6 μm, the table lists the values obtained in this work to match NACO measurements for Charon in the L-band.

is still within the uncertainties of the measurements. However, the assumption that the neutral absorber is "flat" between 2.6 and 4.1 μm results in albedo values that are systematically lower than those observed, at least beyond 3.2 μm. This discrepancy in the L-band between the Charon spectrum and the extrapolated "standard model" suggests that the neutral absorber may probably absorb less beyond 3.2 μm than anticipated. Figure 3.23 shows the comparison between Charon's spectrum (solid line) and the standard model (dashed line) now with the assumption that the absorption coefficient of the neutral absorber is 822 cm^{-1} in the range (2.7-3.2) μm, 150 cm^{-1} in the range (3.3-3.7) μm, and 100 cm^{-1} from 3.8 to 4.1 μm. The optical constants of the neutral absorber are listed in Table 3.7. The match of the NACO data is improved. However, since the optical constants of the absorber are adopted and not measured, no firm conclusion can be drawn from these results.

3.3.2.3 Charon's contribution to the unresolved Pluto/Charon system

Figure 3.24 shows the comparison between the geometric albedo of Pluto/Charon ($A_{gPC}(\lambda)$) combined (solid line) and that of Pluto ($A_{gP}(\lambda)$) only (dashed line) over the wavelength range (1.0-4.1) μm. The former was calculated using the following formula

$$A_{gPC}(\lambda) = \frac{F_{PC}(\lambda)}{F_P(\lambda)} A_{gP}(\lambda) \, , \tag{3.8}$$

where $F_{PC}(\lambda)$ and $F_P(\lambda)$ indicate the relative reflectance of Pluto/Charon system and Pluto, respectively. The previous relation was obtained from the following equation

$$A_g(\lambda) = \frac{D^2 d^2 F(\lambda)}{R^2 F_S(\lambda)} \tag{3.9}$$

89
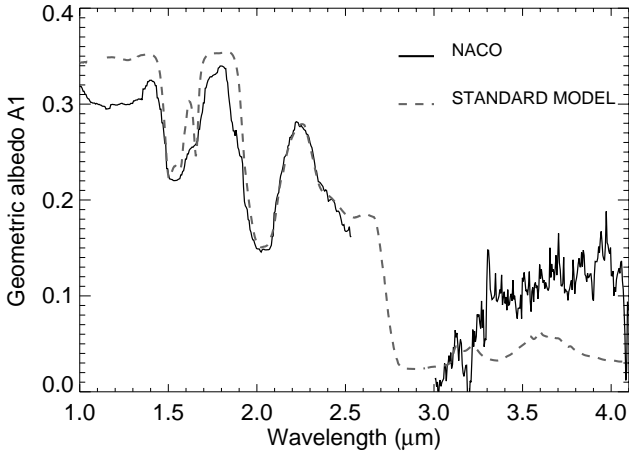
Figure 3.21: Charon's spectrum at 1° phase angle (A_1) obtained with NACO in the wavelength range (1.0-4.1) μm (solid line) compared with the "standard model" of Buie and Grundy (2000) extrapolated beyond 2.6 μm (dashed curve) as described in the text. The feature around 3.2 μm is maybe an artifact from the data reduction.

taken from Douté et al. (1999) and used to convert the flux of Pluto/Charon system as received on Earth ($F(\lambda)$) into geometric albedo ($A_g(\lambda)$). In the previous formula D and d, respectively, correspond to the heliocentric and geocentric distances of Pluto/Charon system, R is their mean quadratic radius, and F_S is the solar flux at 1AU. Assuming the heliocentric distance, geocentric distance, and mean quadratic radius of Pluto/Charon system are the same as those of Pluto, it is possible to derive eq. (3.8) from eq. (3.9). The difference between the averaged geometric albedo of the combined system and that of Pluto represents Charon's spectral contribution to the unresolved system. This results in a contribution of 7% in JHK and about 2% in the L-band.

3.4   Conclusions and discussion

We have obtained the first resolved Pluto and Charon spectra up to 5 μm and 4 μm, respectively. These data provide important tools to improve our knowledge of the surfaces of Pluto and Charon.

The M-band spectrum of Pluto reveals the presence of an absorption band around 4.6 μm not previously detected. We found that CO ice, known to be present on Pluto's surface from the short wavelength region, contributes significantly to this feature, showing an absorption band at 4.67 μm. We investigated the possibility that nitriles on Pluto might contribute to the 4.6-μm absorption. Nitriles are not unexpected because they are products of reactions between methane and nitrogen, which are both abundant on the surface of Pluto (dello Russo and Khanna 1996). In particular we found that acrylonitrile,
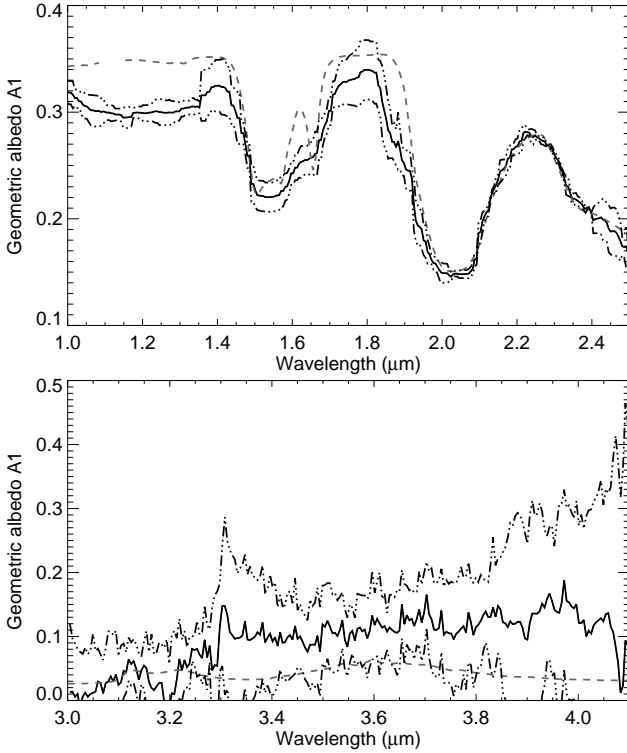
Figure 3.22: Comparison between the averaged NACO spectrum (solid) and the extended "standard model" (dashed) over the wavelength range (1.0-2.5) μm (top panel) and (3.0-4.1) μm (bottom panel). Overplotted are the NACO spectra of Charon obtained adding and subtracting the STD (dash-dot-dot-dot lines).

CH_2CHCN, is the only nitrile, measured in the laboratory, having an absorption around 4.6 μm that also gives a satisfactory fit to Pluto's spectrum in the short wavelength region. We note, however, that the introduction of CH_2CHCN in our model results only in a weak absorption (weaker than the feature detected), and furthermore that this absorption is located to the "left" (4.5 μm) of the feature detected in Pluto's spectrum. Another species that might weakly contribute to the 4.6-μm absorption in Pluto's spectrum is deuterated methane, CH_3D, that has an absorption band at 4.56 μm which, if confirmed, provides a very interesting scientific perspective, i.e. constraining the abundance of CH_3D would allow us to determine the H/D ratio on Pluto. Unfortunately, laboratory data for the optical constants of CH_4 ice with various values of the H/D ratio are lacking, and the issue of the H/D ratio in Pluto remains unsolved for the time being.
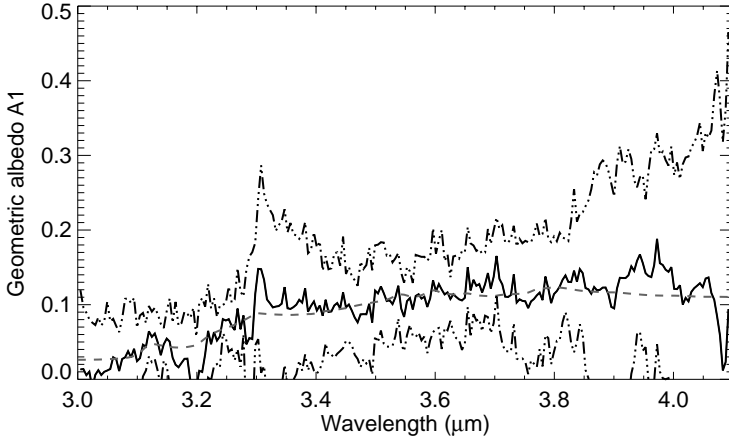
Figure 3.23: Comparison between the averaged spectrum of Charon (solid) together with its STD (dash-dot-dot-dot) and the "standard model" (dashed), now modifying the absorption coefficient of the neutral continuum absorber in the wavelength region beyond 3.2 μm (see text).
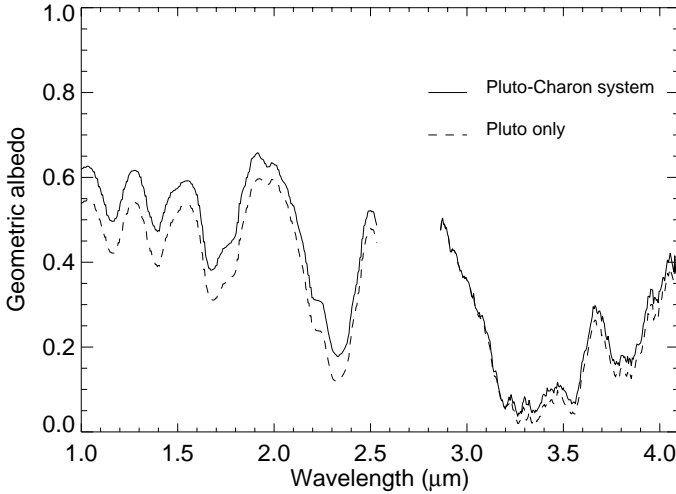
Figure 3.24: Geometric albedo of Pluto/Charon system (solid line) compared with the one of Pluto alone (dashed line) in the wavelength range (1.0-4.1) μm.

Comparing the Pluto observations obtained at VLT in 2005 with those obtained at Keck in 2001, we note a significant change of the slope between 2.9 and 3.1 μm. Since different viewing longitudes is an unlikely explanation, one could consider instead changes in the observed sub-solar latitude on Pluto or a resurfacing process on Pluto, the latter being an hypothesis that needs to be confirmed by further observations. The slope of the spectrum between 2.9 and 3.1 μm is diagnostic of the areal mixing ratio of pure to diluted CH_4, since pure CH_4 has a steeper slope than that of methane diluted in N_2. The modeling analysis of the NACO and Keck observations revealed that the concentration of pure CH_4 may have increased by 15% from 2001 to 2005. This evidence could be explained in terms of atmosphere-surface interaction. Indeed, despite its small size, implying low surface gravity, and its large distance from the Sun, implying low surface temperature, Pluto has a substantial atmosphere derived from volatile ices on its surface. The atmosphere has been directly detected from its effect on the occultation of bright stars by Pluto. Because of the high abundance and volatility of N_2, this atmosphere should be dominated by N_2. Based upon this finding, one could hypothesize that fresh pure CH_4 ice has formed on Pluto's surface recently, maybe recondensing from the weak temporary atmosphere. In fact, CH_4 is expected to freeze out first, compared to CO and N_2 (Delsemme 1982), when Pluto's atmosphere cools down while the dwarf planet is moving away from the Sun.

The same argument has been used by Licandro et al. (2006a) to explain a decreasing nitrogen abundance with increasing depth into the surface of Eris. The trend of CH_4/N_2 into the surface of Eris has been measured considering the blue shift and albedo at maximum absorption of methane ice bands in the visible wavelength range. Indeed, stronger bands in the spectrum of an icy dwarf planet give, on average, better constraints on the surface than weaker bands. Licandro et al. (2006a) speculated that as Eris moved towards aphelion during the last 200 years, and its atmosphere cooled down, volatile methane was freezing out first. As the atmosphere of Eris cooled further, it became more and more nitrogen rich, until the much more volatile N_2 could condense on top of the methane-rich ice. Abernathy et al. (2008), on the contrary, applying the same technique used by Licandro et al. (2006a), found an increasing nitrogen abundance with depth on Eris. This has been explained by Abernathy et al. (2008) with an atmosphere-surface model. Indeed, according to Abernathy et al. (2008), Eris may have a sub-solar latitude of 40° at present. This means that the pole that is visible near aphelion was in permanent winter darkness at perihelion. Near perihelion, sublimation could have built up atmospheric pressure on the sunlit hemisphere (summer pole) sufficient to drive winds towards the dark hemisphere (winter pole), where the winds would condense. Because nitrogen is more volatile and scarcer than methane (the concentration of pure CH_4 with respect to N_2 is greater on Eris than on Pluto – see (Brown et al. 2005; Dumas et al. 2007) –), it may have sublimated from the summer hemisphere relatively early in the season becoming the early season ice deposited on the winter pole. Later in the season, much of the nitrogen was exhausted from the summer pole, but there was still plenty of methane, which continued to sublimate. In this way at the winter pole methane would be more diluted with increasing depth into the surface of Eris. The wind transport described by Abernathy et al. (2008) could be applied on Pluto in the same way as in Eris, thus explaining the increasing abundance of methane on Pluto's surface, although climatological models for Pluto have not yet been developed. The increasing nitrogen abundance with depth on Eris found by Abernathy et al. (2008) apparently contradicts the Licandro et al. (2006a) result

of a decreasing nitrogen abundance with depth. The easiest explanation for the different observations obtained by Licandro et al. (2006a) and Abernathy et al. (2008) is that they are a result of surface heterogeneity. Although, since few years have passed between the two observations, it seems unlikely that significantly different surface portions have been observed. The known surface heterogeneity of Pluto (Grundy and Buie 2001) and the many similarities between Pluto and Eris (see Section 1.5.1) support the different surface coverage in latitude as explanation for the different concentration of pure CH_4 we have found between the 2001 and 2005 observations.

Charon's spectrum obtained with NACO in 2005 is not contaminated by light from Pluto and extends well beyond 2.6 μm, compared to previous work by Buie and Grundy (2000). Prior to the present study, Pluto's spectrum was isolated by removing a modeled spectrum of Charon from the ground-based spectra of the combined Pluto/Charon system. In the work by Olkin et al. (2007), because of the absence of reflectance measurements for Charon beyond 2.5 μm, it was necessary to make assumptions about Charon's L-band spectrum. We have verified that the "standard model" of Buie and Grundy (2000), extended beyond 2.6 μm assuming that the absorption coefficient of the neutral absorber is 822 cm^{-1} in the range 2.6-4.1 μm, matches Charon's spectrum within the errors, although the modeled albedo is systematically lower than the measured value beyond 3.2 μm. Using NACO measurements for Charon it was possible to calculate the hypothetical spectral properties of the unknown neutral absorber beyond 2.6 μm to compensate for this deviation. The possible presence of hydrated ammonia on Charon's surface detected by the 2.21-μm feature (Cook et al. 2007) was not taken into account, because the low spectral resolution of NACO data does not enable us to constrain the existence of this ice on Pluto's satellite.

Comparing the spectrum of Pluto/Charon combined with that of Pluto alone, we have found that Charon's contribution to the unresolved system is 7% in JHK and about 2% in the L-band. The negligible contribution of Charon in the L-band allows to conclude that the absorption bands detected by Grundy et al. (2002a) at 2.9 and 4.1 μm in the spectrum of the unresolved Pluto/Charon system (see introductory part of this chapter) were correctly attributed to Pluto's surface. For the same reason the non detection of these absorptions by Olkin et al. (2007) can not be due to a wrong removal of Charon's contribution from the Pluto/Charon spectrum. We also note that we do not detect the absorptions at 2.9 and 4.1 μm in the NACO Pluto spectrum, so we are confident to state that these features have been the result of the not simultaneous modeling in the near- and mid-infrared ranges by Grundy et al. (2002a).

These results all together highlight the importance of performing modeling analysis of the spectroscopic observations simultaneously in the near- and mid-infrared wavelength ranges. The negligible contribution of Charon to the unresolved Pluto/Charon system makes the difference between the observations obtained at VLT in 2005 and those obtained at Keck in 2001 exclusively related with Pluto.

4 Surface variations on the TNO binary (47171) 1999 TC$_{36}$: ESO Large Program on TNOs

In October 2006 a two year Large Program at the Very Large Telescope at the European Southern Observatory (VLT-ESO, Cerro Paranal, Chile) started under the leadership of M.A. Barucci (Observatoire de Paris, Meudon) for the study of the surface properties of selected Transneptunian objects (TNOs) belonging to several dynamical groups. The main goal is to perform high signal-to-noise ratio (S/N) visible and near-infrared simultaneous spectroscopic observations for almost all TNOs observable within the VLT capability (about 50) with the aim to probe the surface composition of TNOs at unprecedented accuracy. In particular, the purpose is to detect and quantify the ice compounds present on the surface of TNOs (such as H_2O, CH_4, N_2, CO, CO_2), to detect the presence of organics and silicates, and to distinguish by high S/N measurements between crystalline (1.65 μm feature) and amorphous H_2O. Indeed all TNOs with spectra showing water ice absorptions measured with high signal precision present the 1.65-μm feature diagnostic of crystalline water ice (Barucci et al. 2008). Particularly important is the detection of hydrated minerals on the surface of TNOs (see Section 1.4), which is possible only with high S/N measurements. Hydrated minerals have been already detected on the surface of three TNOs (2003 AZ$_{84}$, 47932 GN$_{171}$, 38628 Huya) by Lazzarin et al. (2003) and Fornasier et al. (2004a) using visible spectroscopy. In addition Jewitt and Luu (2001) detected weak features around 1.4 and 2.25 μm in the spectrum of 1999 DE$_9$ that have been attributed to the presence of hydrated minerals. The widespread presence of aqueously altered minerals in TNOs would be an important confirmation, since hydrous materials seem to be present in comets and hydrous silicates are detected in interplanetary dust particles and micrometeorites (de Bergh et al. 2004; Barucci et al. 2008).

Another goal of the ESO Large Program is to target a few binary systems in order to obtain high resolution imaging in J and H filters (K for the brightest) and to measure the color of the pair. For the brightest binaries, low dispersion JHK band spectra of the components resolved are performed in order to analyse the spectral differences between the two partners. Comparing the surface properties of the two components of a binary, one can constrain the origin of these frequent systems in the Kuiper Belt.

One of the binary systems observed in the framework of the ESO Large Program is (47171) 1999 TC$_{36}$ (Trujillo and Brown 2002). In order to investigate the surface composition of this Plutino, spectroscopic and photometric observations have been performed at the ESO-VLT with four instruments, FORS1, NACO, ISAAC, and SINFONI. (47171)

1999 TC$_{36}$ has already been studied spectroscopically by Dotto et al. (2003) and Merlin et al. (2005), but the new observations, presented in this chapter, are characterized by a higher S/N with respect to previous measurements. Also, the importance of this work resides on the fact that observations for (47171) 1999 TC$_{36}$ are available in different periods between 2001 and 2006, through which we can investigate the surface heterogeneity of the target. We apply the radiative transfer model of Hapke (1993) (described in detail in Chapter 2) to the measured spectra and to previous published observations. Indeed, it is necessary to treat all available observations of the binary with the same modeling algorithm, in order to allow a consistent comparison between the retrieved compositions.

4.1   Physical Properties of (47171) 1999 TC$_{36}$

(47171) 1999 TC$_{36}$, discovered to be a binary system by Trujillo and Brown (2002), has been observed by Ortiz et al. (2003) with the aim to determine its rotational period. A very low amplitude signal with a period of 6.21 ± 0.02 h has been obtained. However, this result could not be confirmed using observations taken one month earlier and in a subsequent run, which both gave inconsistent results (Ortiz et al. 2003). Peixinho et al. (2002) observed (47171) 1999 TC$_{36}$ over 8.362 h and no apparent periodic variations have been identified within this time span, which the authors consider an indication that the target could have a longer rotation period.

In the framework of an Hubble Space Telescope program on the characterization of the orbital and physical properties of six confirmed TNOs binaries, Margot et al. (2004) determined the total mass of the binary (47171) 1999 TC$_{36}$ (M = 1.44×10^{19} Kg) and the primary to secondary radius ratio (r$_1$/r$_2$=2.68). Spitzer Space Telescope measurements of the system-integrated thermal emission at wavelengths near 24 and 70 μm lead to an effective diameter of the binary of about 415 km and an effective visible geometric albedo for the system of 7.2% (Stansberry et al. 2008).

The unresolved binary system (47171) 1999 TC$_{36}$ has already been observed spectroscopically in the visible by Lazzarin et al. (2003) and in the near-infrared by Dotto et al. (2003) who also provided a model of the surface composition consisting of Titan tholin, ice tholin, amorphous carbon, and water ice. Merlin et al. (2005) confirm the results obtained by Dotto et al. (2003) for the Plutino (47171) 1999 TC$_{36}$ suggesting an homogeneous surface composition.

Multiple photometric observations of (47171) 1999 TC$_{36}$ are available (McBride et al. 2003; Doressoundiram et al. 2002; Boehnhardt et al. 2001; Delsanti et al. 2006; Dotto et al. 2003). Fulchignoni et al. (2008) list the color results obtained averaging the values reported in literature weighted with the inverse of the error (see Table 4.1). The object is "red" in the visible and neutral in the near-infrared wavelength range.

B-V	V-R	V-I	V-J	V-H	V-K
1.03±0.02	0.69±0.01	1.33±0.02	2.32±0.01	2.70±0.03	2.70±0.02

Table 4.1: Average colors of (47171) 1999 TC$_{36}$ reported by Fulchignoni et al. (2008).

4.2   Observations and data reduction

We present near-infrared photometric and spectroscopic observations of (47171) 1999 TC$_{36}$ obtained with the NACO instrument at the ESO VLT during 12 October 2006, together with ISAAC and SINFONI spectroscopic observations carried out about one month later on 9 November 2006 and 8 November 2006, respectively. On 9 November 2006, simultaneously with the ISAAC observations, photometric and spectroscopic observations of (47171) 1999 TC$_{36}$ in the visible range have been performed using FORS1. In the following sections we will describe separately the October 2006 observations obtained with the NACO instrument and the November 2006 data acquired with ISAAC, SINFONI, and FORS1. More details are given in the description of the NACO spectroscopic and photometric observations. These observations are our own contribution to the Large Program and were planned, performed, and reduced by the author of this thesis. ISAAC, SINFONI, and FORS1 observations are instead a contribution to this work from the Large Program Team.

4.2.1   October 2006 observations

In this section we describe the spectroscopic and photometric observations of (47171) 1999 TC$_{36}$ obtained during 12 October 2006 using NACO at the ESO VLT. The attention will be focused first on the observing characteristics, such as instrument settings, integration time, calibration frames. A description of the data reduction follows. Particular care has been devoted to the photometric part, since it is new compared to the Pluto/Charon observations presented in the previous chapter.

The ESO Phase 2 Proposal Preparation Tool (http://www.eso.org/observing/p2pp/P2PP-tool.html) has been used to define the observations, that have been performed in visitor mode by Gian Paolo Tozzi and Silvia Protopapa. NACO observations have been planned in order to have the target sufficiently close to a star in order to benefit from the adaptive optics (AO) correction and to resolve the binary system. This kind of observations with the target passing nearby a star are called appulse observations.

4.2.1.1   Spectroscopy

Observations   NACO spectroscopic observations have been acquired using the prism S27_P1 with the CutOff_2.5μm filter and the 172 mas slit. The prism gives the possibility to cover at once the wavelength range from 0.85 to 2.50 μm without introducing uncertainties related with the adjustment, by photometric measurements, of spectra taken in separate atmospheric bands. Star GSC 0467700763 (RA=00:57:10.442, DEC=-03:17:05.57, V=15) was the reference source used for the visible AO sensor of NACO. The minimum distance (6.71″) between the AO star and the target has been obtained around 03:00UT on 12 October 2006. Unfortunately because of the poor seeing conditions we could not close the AO loop (see Table 4.2), and had to work in the open loop instead. As a consequence, we achieved lower spatial resolution, which was insufficient to resolve the binary system, and a lower signal-to-noise ratio in the spectra, responsible for a degraded spectral quality.

The slit acquisition has been performed in H-band using the S27 camera, characterized by a field of view of 28″× 28″and a scale of 27.15 mas/pixel, with a detec-

tor integration time (DIT) of 120 sec. The usual A-B-B-A nodding (with some jitter) along the slit has been applied to acquire the observations. In particular the template NACO_spec_obs_AutoNodOnSlit, that nods the telescope between two positions (A and B) along the slit, has been used (see Section 3.1.2). In this way infrared images can be pairwise subtracted with the object of interest offset to distinct regions of the detector. Three AB cycles have been acquired using a Nod Throw parameter of 10″and a Jitter Box Width of 6″(see Section 3.1.2). Each offset position has been taken with a DIT of 600 sec.

Spectra of the nearby solar analogue star HIP008455 (G2V spectral type), recorded immediately after the target observations, were obtained in order to remove at once the telluric and solar features from the target spectra (see Table 4.2). Calibration star observations were acquired with similar sky condition and identical instrument settings with respect to those of the target. Lamp Flats needed for the data reduction have been observed after the end of the night with the same instrument settings adopted for the target. Since the prism S27_P1 with the CutOff_2.5μm is not included in the NACO Exposure Time Calculator we used as reference the Pluto/Charon spectra for the determination of the spectroscopic parameters mentioned above and listed in Table 4.3.

Data reduction   The usual data reduction for infrared spectroscopy, consisting of background subtraction, flat-fielding, ABBA spectra coaddition has been applied. Particular attention was paid to wavelength calibration because of the absence of arc lamp spectra to calibrate the strongly nonlinear dispersion of the prism. The comparison between the telluric features of the sky background and atmospheric emission and absorption features has been used and the dispersion relation obtained is the same applied to the Pluto/Charon spectra. Thereafter, we performed optimum extraction of the spectra to improve the S/N over the aperture extraction (Horne 1986) and removing of telluric and solar features. The steps for the spectroscopic data reduction have been described in detail in Section 3.1.3.

Date	UT	Telescope	Instr.	airm	Solar An. (airm)	seeing('')	Sky Condition
12 Oct. 2006	02:52	UT4 (Yepun)	NACO	1.11	HIP008455 (1.03)	1.5-1.6	CLR
8 Nov. 2006	01:20	UT4 (Yepun)	SINFONI	1.10	HD 2966 (1.06)	0.7-1.0	CLR
9 Nov. 2006	01:12	UT1 (Antu)	ISAAC	1.11	HD 2966 (1.02)	0.6-0.9	CLR
9 Nov. 2006	01:34	UT2 (Kueyen)	FORS1	1.08	HD 1368 (1.27)	0.8-1.0	CLR

Table 4.2: The table lists the characteristics of the spectroscopic observations of (47171) 1999 TC$_{36}$ obtained at the ESO VLT. The observational date, the universal time (UT corresponding to the first target spectrum acquired), the VLT unit and instrument used, the airmass (mean of the airmass values at the beginning and the end of the target observation), and the observed solar analogue star with its airmass, used to remove the solar contribution, are reported. The visible wavelength seeing is listed. The average sky condition during the night are reported (CLR=clear).

	(47171) 1999 TC$_{36}$	Solar Analogue
DIT (sec)	600	1.8
NDIT (sec)	1	1
Readout mode	FowlerNsamp	FowlerNsamp
Jitter Box Width (arcsec)	6	4
Number of AB cycles	3	4
Number of exposures per offset position	1	1
Nod Throw (arcsec)	10	10
Slit	Slit_172mas	Slit_172mas
Spectroscopic Mode	S27_P1 CutOff_2.5μm	S27_P1 CutOff_2.5μm

Table 4.3: Observing parameters of (47171) 1999 TC$_{36}$ and solar analogue HIP008455 spectroscopic measurements obtained with the NACO instrument. The table lists the detector integration time (DIT) and the number of DITs (NDIT), both given in seconds. The values of the Jitter Box Width and Nod Throw parameters are given together with the number of AB cycles and the number of frames stored per A or B position (see Section 3.1.2). The width of the slit and the spectroscopic mode are specified. FowlerNsamp is the readout mode used for short wavelength spectroscopy. The array is reset, read four times at the beginning of the integration ramp and four times at the end of the integration ramp.

4.2.1.2   Photometry

Observations   Immediately after spectroscopic acquisition, photometric measurements in J, H, and Ks filters, centered at 1.265 μm, 1.66 μm, and 2.18 μm, respectively, have been performed. In particular two imaging sets, each of them made of five frames per filter, have been acquired. The S27 camera with a field of view of 28″× 28″and a scale of 27.15 mas/pixel was used. Integration time per frame was 120 sec in all the filters. The observations were performed using the jitter imaging technique. In particular NACO_img_obs_AutoJitter template has been used. This template offsets the telescope between exposures according to random pattern of offsets automatically determined by the template (see Figure 4.1). The offsets are distributed randomly within a box whose size is defined by the parameter Jitter Box Width (in arcsec). Table 4.4 lists the parameters used to perform the photometric measurements of (47171) 1999 TC$_{36}$.

Stars S677-D and S840-F from the LCO/Palomar NICMOS list of photometric standards (Persson et al. 1998) were observed as reference stars for the determination of the flux calibration coefficients (see below). They have been observed in the J, H, and Ks filters with the same instrument settings adopted for the target. Standard stars are imaged over a grid of five positions, one just above the center of the array and one in each quadrant. After the end of the night and with the telescope closed, (halogen) lamp flats are taken in each combination of filter, camera, and readout mode of the detector used during the night. These flats are internal to CONICA and do not include any effects coming from the telescope or NAOS. These lamp flats are taken by pairs, lamp "on" and "off".

Data reduction   Figure 4.2 shows an example of raw frame of (47171) 1999 TC$_{36}$ taken in J filter (left panel). The target is at the center, while the star used for the AO correction

NACO_img_obs_AutoJitter
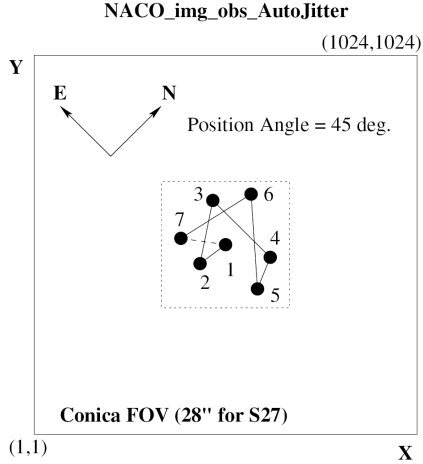
Figure 4.1: An illustration of how the NACO_img_obs_AutoJitter template works. Source: NAOS-CONICA user manual.

	(47171) 1999 TC$_{36}$
DIT (sec)	120
NDIT (sec)	1
Readout mode	FowlerNsamp
Jitter Box Width (arcsec)	4
Number of exposures per offset position	1
Number of offset positions	5
Camera	S27

Table 4.4: Observing parameters of (47171) 1999 TC$_{36}$ photometric measurements obtained with the NACO instrument. These parameters are common to all the filters J, H, and Ks. The table lists the detector integration time (DIT) and the number of DITs (NDIT), both given in seconds. The value of the Jitter Box Width is given together with the number of exposures per offset position and the number of offset positions. FowlerNsamp is the readout mode used. The array is reset, read four times at the beginning of the integration ramp and four times at the end of the integration ramp. The camera used is specified.

is on the left bottom. Now we describe the basic steps of the photometric data reduction, that need to be applied to frames taken in the same filter.

Because of the faintness of the target (V=19.8) and due to its motion we preferred not to rely on the results of the pipeline provided by ESO (ftp://ftp.eso.org/pub/dfs/pipelines/-naco/naco-pipeline-manual-1.1.pdf) but we have developed our own pipeline for the photometric data reduction. MIDAS and IDL packages have been used.

We can distinguish in the data reduction three basic steps: the basic reduction, that consists in sky subtraction, flat-fielding, alignment, and coaddition of jittered images; the object photometry; and the photometric calibration, consisting in the determination of zero-point and extinction coefficient.

Basic reduction

- *Sky subtraction* The sky frame has been estimated as the median of all individual frames in the stack after scaling each of them with the median number of counts in the image. This has been done in order to take into account sky intensity variations due to the presence of stars. The sky frame has been subtracted from each raw science frame, after proper scaling.

- *Flat-fielding and exposure time normalization* In order to correct for the pixel-to-pixel sensitivity variation and non uniform illumination in the detector, it is necessary to normalize each sky subtracted frame by the flat-field. In the morning, after the end of the observing night and with the telescope closed, (halogen) lamp flats are taken in each combination of filter, camera and readout mode of the detector used for the target observations. These lamp flats are taken by pairs, lamp "on" and "off". The flat-field is obtained in the same way in which spectroscopic lamp flats are produced (See Section 3.1.3).

  Each science frame, sky subtracted and flat-fielded, is divided by the detector integration time in order to work with frames of 1 sec exposure.

- *Alignment and coaddition of the jittered images* After sky subtraction and flat-fielding of the individual frames in the stack, the determination of the offsets between the frames is performed. This allows us to align each frame on the target and to consider the median of all individual frames in the stack.

Object photometry   The magnitude of (47171) 1999 TC$_{36}$ was measured on the median frame (see Figure 4.2, right panel) using *aperture photometry*. In order to compute the target magnitude, it is necessary to add the counts in all pixels that contain radiation from the target, to estimate the contribution to these pixels from the sky background using nearby pixels, and then to subtract the sky contribution to get the net signal from the target. The MIDAS MAGNITUDE/CIRCLE function is based on this technique. In particular three concentric circles centered in the target need to be specified. The inner circle is the one in which the target flux is measured, while the outermost annulus is for the sky background determination. The "no_man's_land", that is the annulus between the redia of the second and first circles, can be chosen in order to avoid "hot" and "cold" pixels or stars in the sky background area. Hence, the instrumental magnitude ($m_{measured}$) is given by the following relation

$$m_{measured} = -2.5 log F \text{ with } F = \sum F_{xy} - N_{pix} F_{sky} , \qquad (4.1)$$

where N_{pix} is the number of pixels in the first aperture with radius R, F_{sky} is the background sky value per pixel, F_{xy} is the flux corresponding to the pixel with coordinates
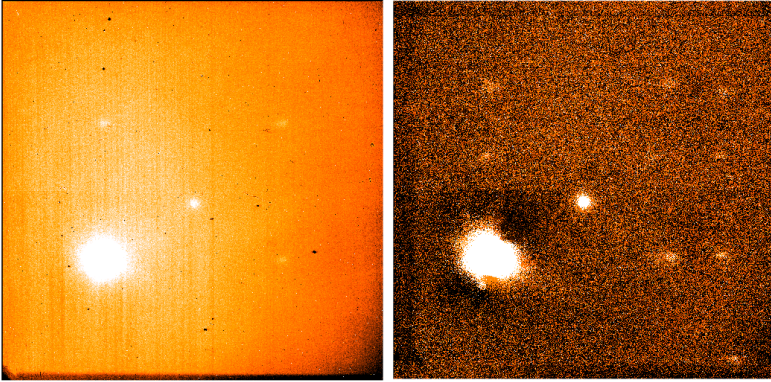
Figure 4.2: Comparison between a photometric frame of (47171) 1999 TC$_{36}$ taken with NACO instrument in J filter before (left panel) and after (right panel) data reduction. The target is at the center of the frame, while the star used for the AO correction is on the left bottom.

(x,y), and the summation is carried out over those pixels whose distance from the target center is less than R. The flux is measured in ADU (Analogic-to-Digital Unit).

The *aperture photometry* technique requires particular care in the target center determination and in the choice of the measurement apertures. Regarding the target center determination, the first step is to extract from the frame a subarea centered on an initial guess for the target center. The size of the area has to be large enough so that it contains the target radiation. From this subarea, summing the pixel intensities down the columns and across the rows we obtain two one-dimensional functions ρ_x and ρ_y along the x and y directions, respectively. Fitting a Gaussian to ρ_x and ρ_y we obtain an estimate of the target center. Even if the AO profile is characterized by a radially symmetric function with a central core and extended wings, the central core can be usually approximated by a Gaussian. In our measurements we do not resolve the binary system (47171) 1999 TC$_{36}$. Hence, the flux that we are measuring is that of the unresolved system.

For the aperture, the classical data reduction method consists of using a big aperture, one large enough to include the majority of the flux of the object, as well as a significant contribution from the sky background. For objects as faint as TNOs (V magnitude ≥ 22), the error from the sky background dominates if the classical method is used. In our case, the aperture photometry has been chosen by the construction of a growth profile (sky subtracted flux versus aperture size) of the object from its center (see Figure 4.3). The growth profile has been obtained measuring the target flux within an aperture whose radius has been increased from the center of the target, corresponding to 0, to a maximum radius chosen by the user. The growth rate is equal to the pixel step size of the frame which corresponds to 1. The sky background is evaluated in a ring aperture just outside of the maximum aperture radius. The starting point of the plateau of this profile provided the photometric aperture.

103
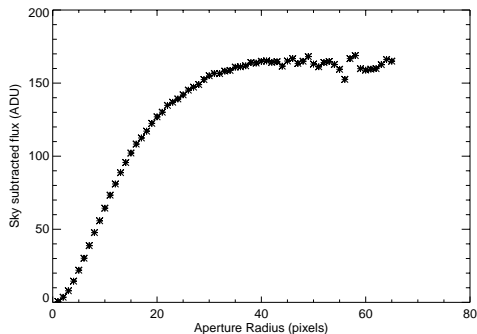
Figure 4.3: Sky subtracted flux of (47171) 1999 TC$_{36}$ as a function of aperture radius.

Photometric calibration   The magnitude of (47171) 1999 TC$_{36}$ measured on the median frame of each stack of data ($m_{measured}$) has been corrected of the zero-point (ZP) and airmass (AM) using the following relation

$$m_{apparent} = m_{measured} + ZP - kAM \ , \qquad (4.2)$$

where k is the extinction coefficient and $m_{apparent}$ is the apparent magnitude of the target. The zero-point represents the correction for the sensitivity of the detector in the bandpass in which the magnitude measurement is performed while the third term in the right side of eq. (4.2) takes into account the effects of the atmospheric extinction according to the Bouguer's law.

Zero-point and extinction coefficient, that are flux calibration coefficients, are computed using photometric standard stars observed with the same instrument configuration as the target over a wide airmass range. The same data reduction described above is applied to the standard stars frames and the instrumental magnitude of each standard star is measured using *aperture photometry* technique. For each standard star it is possible to obtain a relation similar to the eq. (4.2), where $m_{apparent}$ is the tabulated magnitude while ZP and k are determined by means of a linear fit. In our case only two standard stars, S677-D and S840-F from the LCO/Palomar NICMOS list of photometric standards (Persson et al. 1998), have been observed. Hence, the ZP for each standard star has been determined using eq. (4.2) adopting for k the values provided from the data quality control group of ESO (http://www.eso.org/sci/facilities/paranal/-instruments/naco/tools/imaging_standards/). At the end, we determined as ZP the average of the two zero-points.

The apparent magnitudes obtained for (47171) 1999 TC$_{36}$ are presented in Table 4.5. Magnitude errors were estimated as the square root of the quadratic sum of the photometric and calibration (ZP) errors. The error associated to the flat-field was not considered, in the sense that each image was assumed as being perfectly flat-fielded.

Date	UT_{VIS}	V	V-I	UT_{IR}	Instr.	J	H	K_s	J-H	H-Ks
12 Oct. 2006				04:34	NACO	18.24±0.06	17.99±0.08	17.94±0.06	0.25±0.10	0.05±0.10
12 Oct. 2006				05:14	NACO	18.31±0.06	17.99±0.09	17.96±0.05	0.32±0.11	0.03±0.10
09 Nov. 2006	00:58	20.25±0.03	1.26±0.04	00:58	ISAAC	18.17±0.07	17.85±0.07	17.79±0.08	0.32±0.10	0.06±0.11

Table 4.5: Results of the visible and infrared photometric observations of the unresolved binary system (47171) 1999 TC$_{36}$: V, J, H, and K_s. The date of the observations and the VLT instrument are reported. The table lists the UT relative to the beginning of the photometric acquisition sequence. The starting UT time of the visible and infrared observations is indicated by UT_{VIS} and UT_{IR}, respectively. The $V - I$, $J - H$, and $H - Ks$ colors are also reported. The photometric results reported in the last line of this table are discussed in detail by Demeo et al. (2009).

105

4.2.2   November 2006 observations

In this section a brief description of the November 2006 observations is given. We distinguish for clarity the spectroscopic observations obtained with SINFONI on 8 November 2006 from the spectroscopic and photometric measurements acquired with FORS1 in the visible and with ISAAC in the near-infrared wavelength range on 9 November 2006. FORS1 and ISAAC observations were performed in parallel. The November 2006 observations do not resolve the binary system (47171) 1999 TC$_{36}$. They have been performed and reduced by the Large Program Team. For more details on the data obtained for (47171) 1999 TC$_{36}$ in the November 2006 observing run, the reader is referred to the papers by Alvarez-Candal et al. (2008); Demeo et al. (2009); Protopapa et al. (2008a).

SINFONI observations   The near-infrared integral field spectrograph SINFONI is installed at the 8 m "Yepun" ESO-VLT facility at the Paranal Observatory in Chile. The observation was made with the H+K grating, with a spectral resolution of about 1500, allowing to take at once the spectrum between 1.5 and 2.4 μm (Protopapa et al. 2008a). The observations were performed in excellent sky conditions as reported in Table 4.2.

The data reduction was performed using the SINFONI pipeline version 1.6. The pipeline accounts for the whole correction procedures automatically (Alvarez-Candal et al. 2007). The target spectrum is extracted using QFitsView (developed by the Max-Planck-Institut für extraterrestrische Physik). The extraction is performed by integrating the flux over an aperture of about 1″-radius, centered on the photometric center. The spectrum of 47171 (1999 TC$_{36}$) was then divided by the spectra of the corresponding solar analogue (see Table 4.2) and cleaned as explained in Alvarez-Candal et al. (2007). The spectrum was finally smoothed using a running box, to obtain a final spectral resolution of about 100 while increasing S/N.

ISAAC observations   ISAAC at the VLT Unit Telescope 1 (Antu), has been used to obtain J-band spectroscopy of the binary from 1.1 to 1.4 μm. The short wavelength (SW) mode with a slit of 1″width and a spectral resolution of about 500 has been used (Protopapa et al. 2008a). Together with spectroscopic measurements, near-infrared photometry in J, H, and Ks filters (Demeo et al. 2009) centered at 1.25, 1.65, and 2.16 μm, respectively, has been obtained.

The spectroscopic data reduction follows the procedure described by Barucci et al. (2002). The wavelength calibration was performed using Xenon and Argon lamp spectral lines. The object spectrum was divided by the spectrum of the solar analogue HD 2966 observed at similar airmass (see Table 4.2) to correct from telluric lines and to remove the Sun's contribution to the spectrum, obtaining in this way the relative reflectance spectrum of the target. This final J-band spectrum was smoothed using a median filtering to reach a spectral resolution of about 100, in order to improve S/N.

The ESO ISAAC data reduction pipeline using the Eclipse package has been used to perform the photometric data reduction (Devillard 1997). The target flux was then measured using classical photometry methods with apertures determined by the seeing and the growth curve of the object. Zero-points and extinction coefficients have been computed by a least-square-fit of the standard stars. The apparent magnitudes obtained for (47171) 1999 TC$_{36}$ in J, H, and Ks filters are presented in Table 4.5

FORS1 observations   FORS1 at the VLT Unit Telescope 2 (Kueyen) has been used to obtain spectroscopic and photometric observations in the visible range. In particular the spectroscopic measurements have been acquired using the low resolution grism with a 1″wide slit, covering the 0.4-0.94 μm wavelength range with a spectral resolution of about 200 (Alvarez-Candal et al. 2008). The photometric measurements have been obtained in the Bessel V and I filters centered at 0.554 μm and 0.768 μm, respectively (Demeo et al. 2009).

The spectra were reduced using ordinary procedures of data reduction (Fornasier et al. 2004b) with the software packages Midas and IDL. The reduction procedure includes: subtraction of the bias from the raw data, flat-field correction, cosmic rays removal, background subtraction, collapsing the two-dimensional spectra to one dimension, wavelength calibration. The wavelength calibration was made using a lamp with Helium and Argon emission lines. The reflectivity of the object has been obtained by dividing the target spectrum by that of the solar analogue star closest in time and airmass, as reported in Table 4.2. The spectrum has been smoothed with a median filter technique, using a box of 0.0039 μm width in the spectral direction for each point of the spectrum.

The CCD images were reduced and calibrated with a standard method consisting of sky subtraction and flat-fielding, aperture photometry for the target flux measurement, and photometric calibration by the use of standard stars. Table 4.5 lists the V magnitude and the V-I color.

4.3   Observational Results

In this section we present all the results of the unresolved binary system (47171) 1999 TC_{36} obtained from the observations described above. The attention will be focused on the agreement between the near-infrared photometric and spectroscopic observations obtained on the November and October 2006 observing runs. Thereafter a comparison between the two data sets (November 2006 and October 2006) is performed. This section ends presenting the relative reflectance spectrum of (47171) 1999 TC_{36} in the wavelength range between 0.37 and 2.33 μm obtained combining all the November 2006 results.

Figure 4.4 shows the relative reflectance spectrum acquired with ISAAC (solid line) in J-band and SINFONI (dashed line) in H- and K-bands, normalized to 1 around 1.25 μm. The ISAAC and SINFONI spectra have been adjusted using the photometric J-H color (diamonds) determined by the ISAAC data on 9 November 2006 (Demeo et al. 2009) and reported in Table 4.5. This has been done using the general formula

$$R_F = R_G 10^{-0.4[(M_F-M_G)-(M_F-M_G)_\odot]} ,$$ (4.3)

where R_F (R_G) is the target reflectivity in the filter F (G) while M_F (M_G) and $M_{F\,\odot}$ ($M_{G\,\odot}$) are the magnitude in the filter F (G) of the object and the Sun, respectively (Doressoundiram et al. 2008). In the case of ISAAC and SINFONI observations, the filters G and F are the J and H filters, respectively. The reflectivity of the target in the J-band (R_J) is obtained averaging the ISAAC reflectance spectrum from 1.1 to 1.4 μm.

Once the SINFONI and ISAAC spectra are combined using the J-H color, the photometry performed in Ks filter is used only as check of the spectral slope. This is the
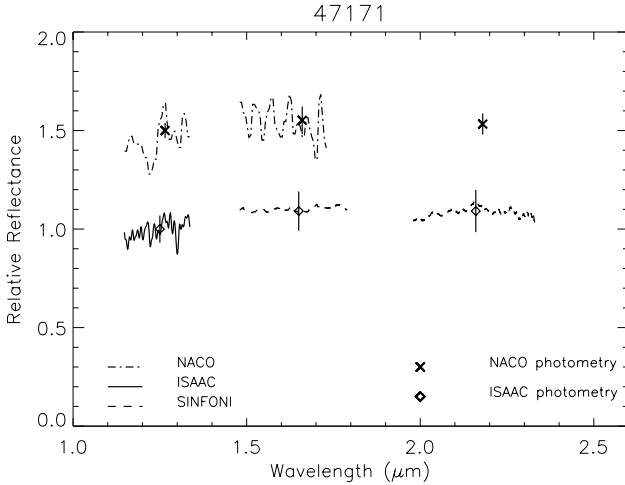
Figure 4.4: The relative reflectance spectrum of (47171) 1999 TC$_{36}$ acquired by ISAAC (solid line) in J-band and SINFONI (dashed line) in H- and K-bands is shown. The spectrum obtained with NACO instrument (dash-dot line) along the wavelength range (1.1-1.7) μm, normalized to 1 around 1.265 μm and shifted by 0.5 in reflectance, is also shown. The normalized photometry in JHKs is overplotted as obtained from ISAAC (diamonds, unit at 1.25 μm) and NACO observations (crosses, unit at 1.265 μm).

advantage of using the H+K grating of SINFONI, that covers at once the complete wavelength range from 1.5 to 2.4 μm. The ISAAC J-Ks color (diamond) confirms the spectral slope of the target.

The spectrum obtained with the NACO instrument (dash-dot line) almost one month earlier in the wavelength range (1.1-1.7) μm, normalized to 1 around 1.265 μm, and shifted by 0.5 in reflectance, is also shown. The spectrum in K-band is not considered because of its poor S/N. The photometric results (crosses) obtained averaging the NACO absolute magnitudes of the two different sets of measurements (see Table 4.5) are overplotted.

NACO spectrum does not show any evidence of particular absorption bands (apart from a feature at 1.22 μm due to a residual terrestrial absorption). Even if the quality of the NACO spectroscopic measurements is not as high as that obtained by ISAAC and SINFONI, NACO, using the prism S27_P1, gives the possibility to have the spectrum of the target in the complete wavelength range (1.1-1.7) μm, without introducing uncertainties related with the adjustment of the spectra taken in separate filters. Moreover, the photometric measurements, which are completely independent from the spectroscopic ones, give the possibility to verify the spectral slope of the target in J- and H-bands. The NACO photometric and spectroscopic results are, within the error bars, in good agreement in J- and H-bands. This agreement makes sure the validity of the NACO measurements.

The spectral behaviour of (47171) 1999 TC$_{36}$ recorded with the NACO instrument in

J- and H-bands is similar to that obtained combining ISAAC and SINFONI spectroscopic observations. Also the photometric results obtained with NACO and ISAAC are compatible within two standard deviation in all the three filters J, H, and Ks, while the colors $J - H$ and $H - Ks$ are in agreement within one standard deviation. All the presented photometric and spectroscopic observations are related to the unresolved binary system (Trujillo and Brown 2002). However, since the visual magnitude difference between the primary and secondary is 2.14±0.02 mag (Stansberry et al. 2006), these observations are dominated by the primary component. Since the rotational motion of the primary component could be "complex" and a large error appears upon extrapolating the period of 6.21 ± 0.02 h, determined by Ortiz et al. (2003) (0.06 mag of amplitude), on 27 days, it is impossible to unambiguously link our spectra to specific rotational phases of this component. Hence, it is difficult to conclude that the similar spectral behaviour recorded on October and November 2006 is a sign of surface homogeneity of (47171) 1999 TC$_{36}$.

Figure 4.5 shows ISAAC and SINFONI spectroscopic observations combined with the visible spectrum obtained by FORS1 on 9 November 2006 (Alvarez-Candal et al. 2008). The different spectral ranges have been adjusted using the V, I, J, H, and Ks photometric colors and converted in reflectivity as described above – see eq. (4.3) – using the solar colors given by Hardop (1980) and Campins et al. (1985). The target spectrum presents a positive spectral slope in the visible range characterized by a spectral gradient S equals to $37.3 \pm 0.7\% (0.1 \mu m)^{-1}$ (Alvarez-Candal et al. 2008) and two possible absorption features around 2.0 and 2.3 μm.

4.4 Modeling

In order to extract information about the surface composition of the Plutino (47171) 1999 TC$_{36}$, the radiative transfer model of Hapke (1993) (see Chapter 2 for details) has been used to obtain the best-fit model of the relative reflectance spectrum of the target, shown in red dash-dot line in Figure 4.5. This was accomplished using an intimate mixture of Triton tholin, Titan tholin, serpentine, and H$_2$O:Tr, representing Triton tholin diluted in crystalline water ice. Tholins are the best candidates to reproduce the spectral slope of the target up to 1 μm. Serpentine is a good choice as darkening agent of the albedo level. Also serpentine together with water ice is a good candidate to reproduce the possible feature at 2.0 μm in the target spectrum and it presents, instead of water ice, an absorption at 2.3 μm. Difficulties in fitting the target spectral slope in the visible range arise considering areal instead of intimate mixture. The optical constants of H$_2$O:Tr have been obtained as described by Douté et al. (1999, Section 3.3.1.1). The reader is referred to Table 4.7 for details on the optical constants of the components used for the modeling, while the characteristics of the best-fit model of the 2006 data are listed in Table 4.6 (see Model 1 2006 data). Using Triton tholin diluted in crystalline water ice improves the fit of the spectral slope in the visible region. An albedo value of 7.2% at 0.55 μm has been considered (Stansberry et al. 2008). Isotropical scattering has been hypothesized, while the values assumed for surface roughness (θ) and compaction parameter (h) are 0° and 0.05 (a lunar-like surface), respectively. The best-fit model has been obtained considering as free parameters the grain size and concentration of each surface terrain in the mixture, iteratively modified by means of a χ^2 minimization algorithm (Levenberg-Marquardt least-squares
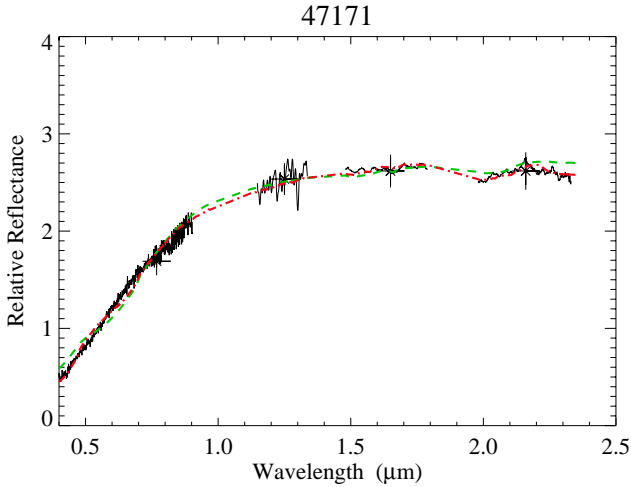
Figure 4.5: Spectral reflectance of (47171) 1999 TC$_{36}$ in the wavelength range (0.37-2.33) μm, normalized to 1 at 0.55 μm. The spectrum has been adjusted using the V, I, J, H, and Ks colors, which are represented by crosses with relative errors (Demeo et al. 2009). The best-fit model (red dash-dot line) obtained with an intimate mixture of Triton tholin, Titan tholin, serpentine, and Triton tholin diluted in crystalline water ice is shown. The green dashed line represents the best-fit model obtained considering an intimate mixture of Titan tholin, amorphous carbon, and Triton tholin diluted in crystalline water ice.
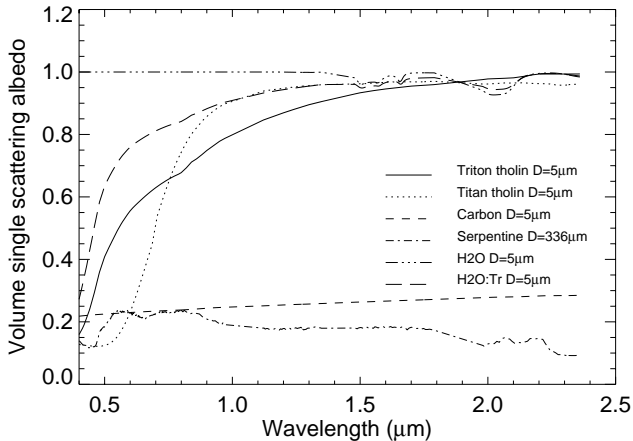
Figure 4.6: Volume single scattering albedo of each element considered in the modeling analysis of (47171) 1999 TC$_{36}$.

minimization) until a best-fit to the observations was achieved. However, we note that the model solution may not be unique and it depends on the surface components considered.

Previous spectroscopic analysis considered the presence of tholins, water ice, and amorphous carbon on the surface of (47171) 1999 TC_{36} (Dotto et al. 2003). The tentative best-fit model for the 47171 (1999 TC_{36}) spectrum obtained considering amorphous carbon instead of serpentine is shown by the green dashed line in Figure 4.5 (for details see Table 4.6, Model 2 2006 data). Considering serpentine instead of amorphous carbon in the mixture improves the best-fit only marginal reducing the χ^2 by 5%. Figure 4.6 shows the volume single scattering albedo of each single terrain considered in the modeling.

Model	Triton Tholin	Titan Tholin	Serpentine	Carbon	H$_2$O:Tr
Model 1 2006 data	1% 5μm	1% 5μm	97% 336μm	0%	1% 5μm (45% Tr)
Model 2 2006 data	0%	30% 5μm	0%	44% 5μm	26% 5μm (49% Tr)
Model 1 2001 data	0%	10% 13 μm	85% 138μm	0%	5% 8μm (39% Tr)
Model 2 2001 data	0%	38% 10 μm	0%	27% 9μm	35% 12 μm (18% Tr)

Table 4.6: The best-fit model solutions for (47171) 1999 TC$_{36}$.

Element	Optical constants	Wavelength range
Triton Tholin	Khare et al. (1994)	(0.05-124) μm
Titan Tholin	Imanaka et al. (2004)	(0.19-25) μm
Serpentine	Roger Clark (private communication)	(0.3-2.5) μm
H_2O	Warren (1984)	(0.30-0.88) μm
	Roush (1996)	(0.88-0.96) μm
	Grundy and Schmitt (1998)	(0.96-2.74) μm
Carbon	Zubko et al. (1996)	(0.2-4.0) μm

Table 4.7: Optical constants.

4.5   Comparison with published results

Dotto et al. (2003) combined near-infrared spectroscopic observations, obtained with the ISAAC instrument on 9 and 10 of September 2001, with the visible spectrum acquired by Lazzarin et al. (2003) with the FORS1 instrument on 15 October 2001. The spectra have been adjusted using the photometric B, V, R, I, J, H, and Ks colors obtained in September and October 2001. Figure 4.7 shows the reflectance spectrum presented by Dotto et al. (2003) together with the photometric colors and the modeling proposed. The modeling solution consisted of 57% of Titan tholin, 25% of ice tholin, 10% of amorphous carbon, and 8% of water ice (see solid continuous line). In the same panel, shifted by 1 unit in reflectance, the relative reflectance spectrum obtained on October 2003 by Merlin et al. (2005) is shown, compared with the same modeling of Dotto et al. (2003) (see solid continuous line). In order to correlate the 2001 and 2003 observations with those acquired in 2006, the FORS1-ISAAC-SINFONI observations together with the best-fit modeling proposed in this work, are shown in the same panel, shifted by 2.5 unit in reflectance. The reflectance spectra acquired in 2001 and 2003, presenting similar spectral behaviour, differ from the 2006 reflectance spectrum. This difference can be quantified in terms of photometric colors and spectroscopic modeling.

Comparing the photometric colors reported in Table 4.5 with those obtained by previous observations and listed in Table 4.1 (Fulchignoni et al. 2008), it is possible to conclude that the color V-I is unaltered. Also the spectral gradient measured by Alvarez-Candal et al. (2008) on the 2006 FORS1 observations ($S = 37.3 \pm 0.7\%(0.1\mu m)^{-1}$) is in agreement with that obtained by Lazzarin et al. (2003) from the 2001 FORS1 measurements ($S = 30.6 \pm 0.2\%(0.1\mu m)^{-1}$), taking into account the slightly different wavelength ranges in which the determination has been performed. The colors V-J and V-H decreased of approximately 0.2 mag and 0.3 mag, respectively, with respect to previous measurements. The color V-Ks changed by 0.2 mag instead.

In order to perform a comparison in terms of surface composition between the 2001 and 2006 data, the Hapke radiative transfer model applied to the 2006 observations (Section 4.4) has been applied also to the 2001 data. This approach guarantees a consistent comparison between the retrieved compositions of the target. Figure 4.8 shows the relative reflectance spectrum of (47171) 1999 TC$_{36}$ presented by Dotto et al. (2003) together with our best-fit modeling for these observations, obtained by using the same surface components as for the modeling of the 2006 data. Green dashed line represents an intimate mixture of Titan tholin, amorphous carbon, and H_2O:Tr (see Table 4.6, Model 2
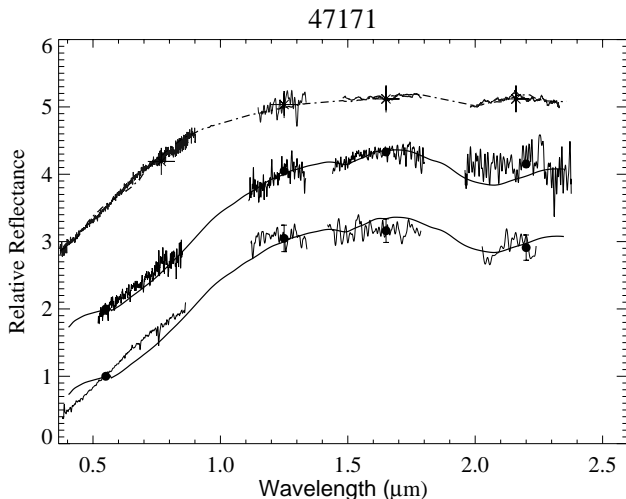
Figure 4.7: Relative reflectance spectrum of (47171) 1999 TC$_{36}$ obtained in 2001 by Dotto et al. (2003) (bottom), in 2003 by Merlin et al. (2005) (shifted by 1 unit in reflectance) and in 2006 (this work) (shifted by 2.5 unit in reflectance). The two continuous solid lines represent the modeling suggested by Dotto et al. (2003), while in dash-dot line is shown the best-fit modeling proposed in this work (see red dash-dot line in Figure 4.5).

2001 data). The best-fit model acquired using serpentine instead of amorphous carbon (see Table 4.6, Model 1 2001 data) is shown in red dash-dot line. Both modeling results have been obtained in the same conditions as those retrieved for the 2006 data. The evidence that serpentine gives a better fit with respect to amorphous carbon not only for the 2006 observations (Section 4.4) but also for the 2001 data strengthens the presence of this element on the surface of the target.

The modeling analysis of the 2006 and 2001 observations revealed that the surface composition of the target has changed (see Table 4.6).

4.6   Conclusions

The surface composition of the Plutino (47171) 1999 TC$_{36}$ has been investigated. Near-infrared photometric and spectroscopic observations of the unresolved binary system (47171) 1999 TC$_{36}$ taken with the adaptive optics instrument NACO at the ESO VLT on 12 October 2006 are presented together with ISAAC, and SINFONI observations carried out on 9 November 2006 and 8 November 2006, respectively. The two data sets taken almost one month apart reveal the same spectral behaviour. Unfortunately, because of the inaccuracy with which the rotational period is known, it is difficult to unambiguously link our observations to specific rotational phases of the target.
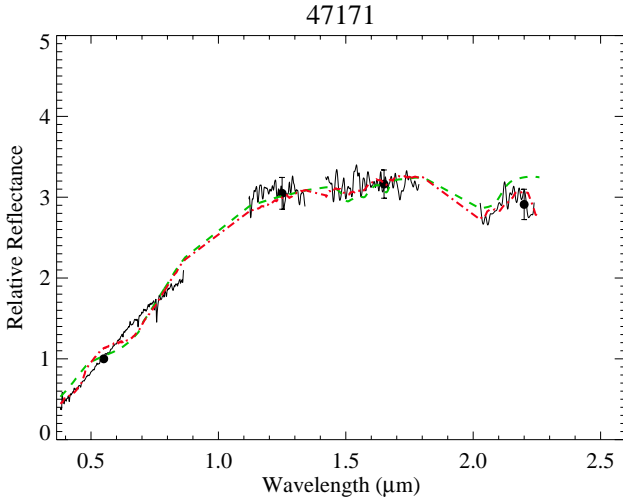
Figure 4.8: Spectral reflectance of (47171) 1999 TC$_{36}$ presented by Dotto et al. (2003). Our models for these observations are overplotted. The green dashed line represents the best-fit model obtained considering an intimate mixture of Titan tholin, amorphous carbon, and Triton tholin diluted in crystalline water ice. The best-fit model (red dash-dot line) obtained with an intimate mixture of Titan tholin, serpentine, and Triton tholin diluted in crystalline water ice is also shown.

The ISAAC and SINFONI spectroscopic observations were combined with the visible spectrum obtained by FORS1 on 9 November 2006 and the relative reflectance spectrum of (47171) 1999 TC$_{36}$ in the wavelength range (0.37-2.33) μm is presented. An intimate mixture of Titan tholin, Triton tholin, serpentine, and Triton tholin diluted in water ice gives the best-fit to the measured spectrum.

The (47171) 1999 TC$_{36}$ observations obtained combining FORS1, ISAAC and SINFONI have been compared with those obtained in 2001 and 2003 by Dotto et al. (2003) and Merlin et al. (2005), respectively. The 2006 observations in H- and K-bands present an higher S/N with respect to published measurements that have been acquired using the ISAAC instrument. The reflectance spectra obtained in 2001 and 2003, presenting similar spectral behaviour, differ from the 2006 reflectance spectrum. Indeed the 2001 and 2006 observations present similar spectral gradient in the visible range but different V-J, V-H, and V-Ks colors. In order to quantify the spectral difference between the 2001 and 2006 data in terms of spectroscopic modeling, the Hapke radiative transfer model applied to the 2006 observations has been applied also to the 2001 data. This approach has revealed that the surface composition of the target has changed between 2001 and 2006.

The described spectral behaviour could be due to time variations or to spatial variations. Although time variations are possible (Protopapa et al. 2008b), we consider them less likely since the target surface is volatile-free and interactions between surface and

atmosphere can not be taken into account. It is more probable that the surface portion of (47171) 1999 TC$_{36}$ observed by Dotto et al. (2003) and Merlin et al. (2005) was not the same as observed in 2006. However, it is difficult to know which are the different longitudes observed in 2001, 2003, and 2006 since the rotation period of the target is not known with sufficient accuracy for an accurate phasing of the observing epochs. Surface heterogeneities have already been observed at the surface of several TNOs like 1996 TO$_{66}$ (Brown et al. 1999), 38628 Huya and 47932 2000 GN$_{171}$ (de Bergh et al. 2004) maybe due to partial resurfacing by non-disruptive collisions and/or cometary activity (Merlin et al. 2005).

5 Conclusions

In this thesis we have presented the analysis and results of the surface characterization of three Transneptunian objects: Pluto, Charon, and the unresolved binary system (47171) 1999 TC_{36}. The spectral behaviour recorded by measurements performed at the ESO VLT has been interpreted by using the Hapke radiative transfer model, which allows us to reproduce the observed spectral features, and to model the surface by areal or intimate mixtures of several minerals and ices. We have made full use of the VLT capabilities that enabled us to obtain the first resolved Pluto and Charon spectra up to 5 μm and 4 μm, respectively, and to perform spectroscopic observations at unprecedented accuracy.

Regarding the Pluto/Charon system the main results are the following:

- For the first time the complete L-band spectrum of Pluto is measured by 2005 VLT observations, without unresolved contamination by light from Charon. Moreover, we present the first Pluto M-band spectrum ever. Charon has been studied in some detail in the JHK wavelength region, but was never measured in the L-band, beyond 2.5 μm. Extending the wavelength coverage of the surface spectroscopy beyond K-band complements the New Horizons mission, that will perform spectroscopy of Pluto and Charon surface in JHK band only.

- Apart from known and expected absorption bands from methane ice, our Pluto spectrum reveals a new absorption feature in the M-band centered around 4.6 μm. The main candidate to explain this signature is CO ice, which has an absorption band at 4.67 μm and that is known to be present on Pluto's surface from the short wavelength region. Nitriles, arising from C and N connected with a triple bond, may also contribute. Nitriles have been predicted to be present on the surface of the dwarf planet but were never detected. Finally, the 4.56-μm absorption of deuterated methane, CH_3D, might weakly contribute.

- An areal mixture of pure methane ice with two different grain sizes, methane and CO ice diluted in nitrogen, CH_2CHCN, and Titan tholin fits best Pluto's spectrum, although not in all details.

- Comparing our Pluto observations obtained at VLT in 2005 with those obtained at Keck in 2001 (Olkin et al. 2007), we note a significant change of the slope between 2.9 and 3.1 μm. The modeling analysis of NACO and Keck observations revealed that the concentration of pure CH_4 may have increased by 15% from 2001 to 2005. Since different viewing longitudes is an unlikely explanation, one could consider instead changes in the observed sub-solar latitude or effects of atmosphere-surface interaction. Two possible resurfacing scenarios can take place: recondensation of

ice from the atmosphere or wind transport of ice grains. In the first case, as Pluto is moving further from the Sun, its atmosphere cools down with CH_4 freezing out first. The second scenario involves instead a redistribution of methane ice on the surface due to global scale winds.

- The L-band spectrum of Charon presents broad water ice signatures, in agreement with the (1-2.5) μm wavelength range. The "standard model" of Buie and Grundy (2000), extended beyond 2.6 μm, is systematically lower than the observations beyond 3.2 μm. NACO measurements of Charon enabled to calculate the hypothetical spectral properties of the unknown neutral absorber beyond 2.6 μm to compensate for these deviations. Hence, we present a standard spectroscopic model for Charon that can be used to subtract Charon light from ground-based spectra of the combined Pluto/Charon system.

- Comparing the spectrum of Pluto/Charon combined with that of Pluto alone, we have found that Charon's contribution to the unresolved system is 7% in JHK and about 2% in the L-band.

Regarding the binary system (47171) 1999 TC_{36} we can reach the following conclusions:

- We present the reflectance spectrum of the unresolved binary system (47171) 1999 TC_{36} in the wavelength range (0.37-2.33) μm. These new measurements have the advantage of a higher signal-to-noise ratio in H- and K-bands, with respect to previous published observations (Dotto et al. 2003; Merlin et al. 2005). In this way, we could detect two new features around 2.0 and 2.3 μm. An intimate mixture of Titan tholin, Triton tholin, serpentine, and Triton tholin diluted in water ice gives the best-fit to the measured spectrum. It is the first time that serpentine is considered as a possible element on the surface of (47171) 1999 TC_{36}. This represents a new step forward to the firm identification of hydrated minerals on the surface of Transneptunian objects, important for the understanding of aqueous alteration processes.

- The (47171) 1999 TC_{36} observations have been compared with those obtained in 2001 and 2003 by Dotto et al. (2003) and Merlin et al. (2005), respectively. The reflectance spectra obtained in 2001 and 2003, presenting similar spectral behaviour, differ from the 2006 reflectance spectrum. This differences, that have been quantified in terms of photometric colors and spectroscopic modeling, could be due to surface heterogeneity. Indeed, although temporal variations are possible, we consider them less probable since the target surface is volatile-free and surface-atmosphere interactions can not be taken into account.

This thesis work casts new light on Pluto/Charon and (47171) 1999 TC_{36} as individual members of the Transneptunian population, important because considered remnant from the formation of the Solar System. In particular the detailed analysis of the surface composition of Pluto/Charon gives information on the family of the large Transneptunian objects as a whole. The comparison between Pluto/Charon and (47171) 1999 TC_{36} allows us to better understand a possible correlation between surface composition and

dynamical properties. Indeed, both Pluto/Charon and (47171) 1999 TC_{36} belong to the Plutino population: Transneptunian objects in mean motion resonance with Neptune 3:2. In spite of the same dynamical history, the two systems present completely different surface characteristics, with Pluto and Charon dominated by the presence of methane and water ice, respectively, and (47171) 1999 TC_{36} almost completely covered by serpentine, an hydrated mineral. This finding gives support to the volatile loss theory formulated by Schaller and Brown (2007a), which is dominated by atmospheric escape. The difference in gravity between Pluto and (47171) 1999 TC_{36} (of a factor of several tens in favour of Pluto) is sufficient to explain the surface composition of the two objects, one volatile-rich and the other volatile-free.

Based on our and recently published results by Licandro et al. (2006a) and Abernathy et al. (2008), there is growing evidence of weather patterns driven phenomena on the surface of dwarf planets. However, this scenario should be further explored by observation and modeling work.

This thesis work can be expanded in different directions. Low-dispersion L+M band spectroscopy together with high-dispersion spectroscopy in J-, H-, and K-bands of two opposite hemispheres of the dwarf planet would allow us to perform a systematic study of the spatial and temporal distribution of Pluto's surface ices. The main goal of the rotation-phase resolved L+M spectra of Pluto is to measure spectral changes with longitude, i.e. differences in the chemical composition and in the areal mixing ratios of the detected ices. In particular, L+M band low-dispersion spectroscopy would allow to follow the temporal evolution of the slope changes in the 2.9-3.2 μm region that indicates variations in the CH_4 surface coverage. Also, better signal-to-noise ratio spectra would be important to confirm the new absorption band at 4.6 μm. The high-dispersion JHK spectra would complement the investigation of surface heterogeneities in L-band, since further CH_4 absorption bands as well as N_2 and CO ice absorptions could be resolved. In particular, H- and K-band would allow to assess in a very complementary approach the determination of CH_4/CH_4:N_2 since the mixing ratio of pure and diluted CH_4 ice can be studied via the wavelength shift of the CH_4 absorptions bands. Also, following Pluto along its orbit would allow to better define which surface-atmosphere interaction scenario is the most probable one. Further observations are thus needed and must be complemented by a modeling of Pluto global circulation.

A high precision determination of the orbital period of (47171) 1999 TC_{36}, that can be pursued by light curves measurements, is needed for the planning of new observations of this target, in order to confirm the hypothesized surface heterogeneity. Also, resolving the binary system, obtaining low dispersion JHK spectra of the two components, would help to better understand the origin of Transneptunian binaries.

The techniques adopted to perform the work presented in this dissertation are powerful tools to draw a global picture of the Transneptunian population. The systematic application to statistically significant sample of TNOs would thus greatly increase our knowledge on the characteristics, composition, and origin of these intriguing bodies.

A Multiple Scattering

In this appendix eq. (2.19) for the multiply scattered radiance I_{Dm}, defined by the following relation

$$I_{Dm} = \int_0^\infty \frac{w(\tau)}{4\pi} \int_{4\pi} P(\tau, \Omega', \Omega_D) I(\tau, \Omega') d\Omega' \, e^{-\frac{\tau}{\mu}} \frac{d\tau}{\mu} \, , \qquad (A.1)$$

will be obtained, in order to include multiple scattering in the calculation of the bidirectional reflectance. The two-stream method will be used to obtain an approximate solution to the radiative-transfer equation for a semiinfinite medium of isotropic scatterers. The geometry is the same as in Figure 2.2. Collimated irradiance J is incident on a particulate medium. The space above the plane corresponding to $\tau = 0$ is empty, except for the source and the detector, and the volume below this plane contains particles that both scatter and absorb. Thermal emission is assumed to be negligible.

Consider a radiance field $I(s, \Omega)$ which describes the intensity of electromagnetic radiation at point s, propagating into a direction Ω, that has been scattered or emitted at least once within a particulate medium. The units of $I(s, \Omega)$ are power per unit area per unit solid angle. In general, unless stated otherwise, $I(s, \Omega)$ will also be a function of wavelength or frequency; however this dependence usually will not be noted explicitly. Suppose s lies on the base of a right cylinder of area dA, length ds and volume $dsdA$ where ds points in the direction of Ω. The equation of radiative transfer for $I(s, \Omega)$, used to calculate how the intensity of an electromagnetic wave is changed by the processes of emission, absorption, and scattering as the wave propagates through a complex medium, is

$$\frac{\partial I(s, \Omega)}{\partial s} = -E(s, \Omega) I(s, \Omega) + \frac{1}{4\pi} \int_{4\pi} I(s, \Omega') G(s, \Omega', \Omega) d\Omega' + F(s, \Omega) \, , \qquad (A.2)$$

where the meaning of E, G, and F has been explained in Section 2.2. The previous equation is the general form of the equation of radiative transfer. In most applications, like in the case considered in Section 2.2, the medium is horizontally stratified. Let the positive z axis point in the vertical direction, and let ds make an angle θ with dz, so that $dz = ds \cos \theta$. Making this substitution gives

$$\cos \theta \frac{\partial I(z, \Omega)}{\partial z} = -E(z, \Omega) I(z, \Omega) + \frac{1}{4\pi} \int_{4\pi} I(z, \Omega') G(z, \Omega', \Omega) d\Omega' + F(z, \Omega) \, . \qquad (A.3)$$

If we consider single scattering, the only process that contributes to the volume emission $(F \to F_S)$, and taking into account eq. (2.10), (2.11), and (2.12), the previous equation can be written in the following way

$$-\cos \theta \frac{\partial I(\tau, \Omega)}{\partial \tau} = -I(\tau, \Omega) + \frac{w(\tau)}{4\pi} \int_{4\pi} I(\tau, \Omega') P(\tau, \Omega', \Omega) d\Omega' +$$

$$+ \frac{J}{4\pi} w(\tau) P(\tau, \Omega_0, \Omega)\, e^{-\dfrac{\tau}{\mu_0}} . \tag{A.4}$$

The *multistream method* for obtaining approximate solutions of the radiative transfer equation will be used. The sphere of all propagation directions Ω is broken up into N regions of solid angle $\Delta\Omega_j$, which need not to be equal. The radiative transfer equation – see eq. (A.4) – is integrated in solid angle over each of the regions $\Delta\Omega_j$ and each resulting equation divided by $\Delta\Omega_j$, giving N equations of form

$$-\frac{1}{\Delta\Omega_j} \int_{\Delta\Omega_j} \frac{\partial I(\tau, \Omega)}{\partial \tau} \cos\theta\, d\Omega = -\frac{1}{\Delta\Omega_j} \frac{\partial}{\partial \tau} \int_{\Delta\Omega_j} I(\tau, \Omega) \cos\theta\, d\Omega =$$

$$= -\frac{1}{\Delta\Omega_j} \int_{\Delta\Omega_j} I(\tau, \Omega)\, d\Omega + \frac{w(\tau)}{4\pi} \frac{1}{\Delta\Omega_j} \int_{\Delta\Omega_j} \int_{4\pi} I(\tau, \Omega') P(\tau, \Omega', \Omega)\, d\Omega'\, d\Omega +$$

$$+ J \frac{w(\tau)}{4\pi} e^{-\dfrac{\tau}{\mu_0}} \frac{1}{\Delta\Omega_j} \int_{\Delta\Omega_j} P(\tau, \Omega_0, \Omega)\, d\Omega . \tag{A.5}$$

Define the following average quantities for the j-th zone

$$I_j(\tau) = \frac{1}{\Delta\Omega_j} \int_{\Delta\Omega_j} I(\tau, \Omega)\, d\Omega , \tag{A.6}$$

$$\mu_j = \frac{1}{\Delta\Omega_j} \int_{\Delta\Omega_j} \cos\theta\, d\Omega , \tag{A.7}$$

$$p_{hj} = \frac{1}{\Delta\Omega_h} \frac{1}{\Delta\Omega_j} \int_{\Delta\Omega_h} \int_{\Delta\Omega_j} P(\tau, \Omega', \Omega)\, d\Omega'\, d\Omega , \tag{A.8}$$

$$\overline{p}_j = \frac{1}{\Delta\Omega_j} \int_{\Delta\Omega_j} P(\tau, \Omega_0, \Omega)\, d\Omega . \tag{A.9}$$

Note that p_{hj} is the fraction of the radiance travelling in the direction of the center of region h that is scattered into region j and $\overline{p}_j$ is p_{hj} with Ω_h considered as the region containing the direction to the collimated source. In eq. (A.5), $I(\tau, \Omega)$ is replaced by its average value $I_j(\tau)$, which may then be taken out of the integrals over angle. Then the equation for the radiance in the j-th directional region becomes

$$-\mu_j \frac{dI_j(\tau)}{d\tau} = -I_j(\tau) + \frac{w(\tau)}{4\pi} \sum_{h=1}^{N} \Delta\Omega_h p_{hj} I_h(\tau) + J \frac{w(\tau)}{4\pi} \overline{p}_j\, e^{-\dfrac{\tau}{\mu_0}} . \tag{A.10}$$

Thus, the partial integrodifferential equation – see eq. (A.4) – is replaced by N linear, first-order coupled differential equations. If N is small enough, the equations can be solved analytically. In particular if $N = 2$, the method is known as the *two stream* or *Schuster-Schwarzschild* method (Schuster 1905). In this case, the sphere of all propagation directions is broken up in two regions: the upward-going hemisphere, denoted by $j = 1$, and the downward-going hemisphere, denoted by $j = 2$. Then $\Delta\Omega_1 = \Delta\Omega_2 = 2\pi$, and eq. (A.7), (A.8), and (A.9) become

$$\mu_1 = \frac{1}{2\pi} \int_0^{2\pi} d\psi \int_0^{\pi/2} \cos\theta \sin\theta\, d\theta = \int_0^{\pi/2} \cos\theta \sin\theta\, d\theta = \frac{1}{2} , \tag{A.11}$$

$$\mu_2 = \frac{1}{2\pi} \int_0^{2\pi} d\psi \int_{\pi/2}^{\pi} \cos\theta \sin\theta d\theta = \int_{\pi/2}^{\pi} \cos\theta \sin\theta d\theta = -\frac{1}{2} , \tag{A.12}$$

$$P(\tau, \Omega', \Omega) = 1 \Rightarrow p_{hj} = 1 \wedge \overline{p}_j = 1 , \tag{A.13}$$

where the hypothesis of isotropic scattering has been used. From eq. (A.10) we obtain the following set of two equations

$$-\frac{1}{2}\frac{dI_1(\tau)}{d\tau} = -I_1(\tau) + \frac{w(\tau)}{2}[I_1(\tau) + I_2(\tau)] + J\frac{w(\tau)}{4\pi} e^{-\frac{\tau}{\mu_0}} , \tag{A.14}$$

$$\frac{1}{2}\frac{dI_2(\tau)}{d\tau} = -I_2(\tau) + \frac{w(\tau)}{2}[I_1(\tau) + I_2(\tau)] + J\frac{w(\tau)}{4\pi} e^{-\frac{\tau}{\mu_0}} . \tag{A.15}$$

Put

$$\varphi = \frac{I_1 + I_2}{2} , \tag{A.16}$$

$$\Delta\varphi = \frac{I_1 - I_2}{2} , \tag{A.17}$$

and alternately add and subtract eq. (A.14) and eq. (A.15) to obtain

$$-\frac{1}{2}\frac{d\Delta\varphi}{d\tau} = -\gamma^2\varphi + J\frac{w}{4\pi} e^{-\frac{\tau}{\mu_0}} , \tag{A.18}$$

$$\frac{1}{2}\frac{d\varphi}{d\tau} = \Delta\varphi , \tag{A.19}$$

where

$$\gamma = \sqrt{1 - w} \tag{A.20}$$

is the albedo factor. Differentiating eq. (A.19)

$$\frac{d\Delta\varphi}{d\tau} = \frac{1}{2}\frac{d^2\varphi}{d\tau^2} \tag{A.21}$$

and inserting into eq. (A.18) gives

$$-\frac{1}{4}\frac{d^2\varphi}{d\tau^2} = -\gamma^2\varphi + J\frac{w}{4\pi} e^{-\frac{\tau}{\mu_0}} . \tag{A.22}$$

This second order differential equation with constant coefficients has the solution

$$\varphi(\tau) = Ae^{-2\gamma\tau} + Be^{2\gamma\tau} + Ce^{-\tau/\mu_0} , \tag{A.23}$$

where A and B are constants to be determined from the boundary conditions, while C can be obtained substituting eq. (A.23) in eq. (A.22). Thus, we have

$$C = \frac{J}{4\pi}\frac{4w\mu_0^2}{4\gamma^2\mu_0^2 - 1} . \tag{A.24}$$

123

The boundary conditions are that the radiance must remain finite everywhere

$$\varphi(\tau \to \infty) = cost , \tag{A.25}$$

and that there be no sources of diffuse radiation above the upper surface

$$I_2(\tau = 0) = 0 . \tag{A.26}$$

Applying the first boundary condition – see eq. (A.25) – to eq. (A.23) we have

$$B = 0 . \tag{A.27}$$

Considering the second boundary condition we have

$$\varphi(\tau = 0) = \Delta\varphi(\tau = 0) = \frac{I_1}{2} . \tag{A.28}$$

Substituting eq. (A.28) in eq. (A.19), and considering eq. (A.23) for $\varphi(\tau)$ with $B = 0$, we have

$$A + C = \frac{1}{2}\left[-2\gamma A - \frac{C}{\mu_0}\right] , \tag{A.29}$$

from which, substituting the expression for C, it is obtained

$$A = -\frac{J}{4\pi}\frac{2\mu_0(1 - \gamma)(1 + 2\mu_0)}{4\gamma^2\mu_0^2 - 1} . \tag{A.30}$$

Let's consider the expression (A.1) for I_{Dm}. Assuming ω independent from z or τ, as is often the case, and isotropic scattering ($P = 1$) we have

$$I_{Dm} = \frac{w}{4\pi}\int_0^\infty \int_{4\pi} I(\tau, \Omega')d\Omega' \, e^{-\frac{\tau}{\mu}}\frac{d\tau}{\mu} =$$
$$= \frac{w}{4\pi}\int_0^\infty \left[\int_{\Delta\Omega_1} I(\tau, \Omega')d\Omega' + \int_{\Delta\Omega_2} I(\tau, \Omega')d\Omega'\right] e^{-\frac{\tau}{\mu}}\frac{d\tau}{\mu} \tag{A.31}$$

that, considering eq. (A.6), becomes

$$I_{Dm} = \frac{w}{4\pi}\int_0^\infty [I_1(\tau)\Delta\Omega_1 + I_2(\tau)\Delta\Omega_2] \, e^{-\frac{\tau}{\mu}}\frac{d\tau}{\mu} =$$
$$= w\int_0^\infty \varphi(\tau) \, e^{-\frac{\tau}{\mu}}\frac{d\tau}{\mu} . \tag{A.32}$$

Substituting the expression for φ given by eq. (A.23) and taking into account eq. (A.30), (A.27), and (A.24) for A, B, and C, respectively, we obtain

$$I_{Dm} = \frac{Jw}{4\pi}\frac{\mu_0}{\mu + \mu_0}[H(\mu)H(\mu_0) - 1] , \tag{A.33}$$

with

$$H(x) = \frac{1 + 2x}{1 + 2\gamma x} . \tag{A.34}$$

B Reference wavelengths for the dispersion solution of the prism L27_P1

Wavelength (μm)	Pixel position
1.19000	341
1.50500	367
1.65500	375
2.10500	399
2.21000	423
2.96227	512
3.21992	541
3.33665	554
4.84364	828
4.89553	840
4.95301	852
5.02235	868
5.14446	882
5.20933	896
5.28962	912

Table B.1: The table lists the reference wavelengths considered for the determination of the dispersion relation of NACO prism L27_P1 and the associated pixel position.

Bibliography

Abernathy, M. R., Tegler, S. C., Grundy, W. M., Licandro, J., Romanishin, W., Corneli-son, D., Vilas, F., 2008, Digging into the surface of the icy dwarf planet Eris, Icarus, submitted

Alvarez-Candal, A., Barucci, M. A., Merlin, F., Guilbert, A., de Bergh, C., 2007, A search for rotational variations on trans-Neptunian objects, A&A, 475, 369–374

Alvarez-Candal, A., Fornasier, S., Barucci, M. A., de Bergh, C., Merlin, F., 2008, Visible spectroscopy of the new ESO large program on trans-Neptunian objects and Centaurs. Part 1, A&A, 487, 741–748

Barkume, K. M., Brown, M. E., Schaller, E. L., 2006, Water Ice on the Satellite of Kuiper Belt Object 2003 EL_{61}, ApJ, 640, L87–L89

Barucci, M. A., Boehnhardt, H., Dotto, E., Doressoundiram, A., Romon, J., Lazzarin, M., Fornasier, S., de Bergh, C., Tozzi, G. P., Delsanti, A., Hainaut, O., Barrera, L., Birkle, K., Meech, K., Ortiz, J. L., Sekiguchi, T., Thomas, N., Watanabe, J., West, R. M., Davies, J. K., 2002, Visible and near-infrared spectroscopy of the Centaur 32532 (2001 PT_{13}). ESO Large Program on TNOs and Centaurs: First spectroscopy results, A&A, 392, 335–339

Barucci, M. A., Cruikshank, D. P., Dotto, E., Merlin, F., Poulet, F., Dalle Ore, C., Fornasier, S., de Bergh, C., 2005, Is Sedna another Triton?, A&A, 439, L1–L4

Barucci, M. A., Merlin, F., Dotto, E., Doressoundiram, A., de Bergh, C., 2006, TNO surface ices. Observations of the TNO 55638 (2002 VE_{95}), A&A, 455, 725–730

Barucci, M. A., Brown, M. E., Emery, J. P., Merlin, F., 2008, Composition and Surface Properties of Transneptunian Objects and Centaurs, pp. 143–160, The Solar System Beyond Neptune

Bernstein, G. M., Trilling, D. E., Allen, R. L., Brown, M. E., Holman, M., Malhotra, R., 2004, The Size Distribution of Trans-Neptunian Bodies, AJ, 128, 1364–1390

Boehnhardt, H., Tozzi, G. P., Birkle, K., Hainaut, O., Sekiguchi, T., Vair, M., Watanabe, J., Rupprecht, G., The FORS Instrument Team, 2001, Visible and near-IR observations of transneptunian objects. Results from ESO and Calar Alto Telescopes, A&A, 378, 653–667

Bowell, E., Lumme, K., 1979, Colorimetry and magnitudes of asteroids, pp. 132–169, Asteroids

Brown, M. E., 2001, The Inclination Distribution of the Kuiper Belt, AJ, 121, 2804–2814

Brown, M. E., 2002, Pluto and Charon: Formation, Seasons, Composition, Annual Review of Earth and Planetary Sciences, 30, 307–345

Brown, M. E., 2008, The Largest Kuiper Belt Objects, pp. 335–344, The Solar System Beyond Neptune

Brown, M. E., Calvin, W. M., 2000, Evidence for Crystalline Water and Ammonia Ices on Pluto's Satellite Charon, Science, 287, 107–109

Brown, M. E., Trujillo, C. A., Rabinowitz, D. L., 2005, Discovery of a Planetary-sized Object in the Scattered Kuiper Belt, ApJ, 635, L97–L100

Brown, M. E., van Dam, M. A., Bouchez, A. H., Le Mignant, D., Campbell, R. D., Chin, J. C. Y., Conrad, A., Hartman, S. K., Johansson, E. M., Lafon, R. E., Rabinowitz, D. L., Stomski, Jr., P. J., Summers, D. M., Trujillo, C. A., Wizinowich, P. L., 2006, Satellites of the Largest Kuiper Belt Objects, ApJ, 639, L43–L46

Brown, M. E., Barkume, K. M., Blake, G. A., Schaller, E. L., Rabinowitz, D. L., Roe, H. G., Trujillo, C. A., 2007a, Methane and Ethane on the Bright Kuiper Belt Object 2005 FY_9, AJ, 133, 284–289

Brown, M. E., Barkume, K. M., Ragozzine, D., Schaller, E. L., 2007b, A collisional family of icy objects in the Kuiper belt, Nature, 446, 294–296

Brown, R. H., Cruikshank, D. P., 1983, The Uranian satellites - Surface compositions and opposition brightness surges, Icarus, 55, 83–92

Brown, R. H., Cruikshank, D. P., Pendleton, Y., 1999, Water Ice on Kuiper Belt Object 1996 TO_66, ApJ, 519, L101–L104

Buie, M. W., Fink, U., 1987, Methane absorption variations in the spectrum of Pluto, Icarus, 70, 483–498

Buie, M. W., Grundy, W. M., 2000, The Distribution and Physical State of H_2O on Charon, Icarus, 148, 324–339

Buie, M. W., Cruikshank, D. P., Lebofsky, L. A., Tedesco, E. F., 1987, Water frost on Charon, Nature, 329, 522–523

Buie, M. W., Tholen, D. J., Wasserman, L. H., 1997, Separate Lightcurves of Pluto and Charon, Icarus, 125, 233–244

Campins, H., Rieke, G. H., Lebofsky, M. J., 1985, Absolute calibration of photometry at 1 through 5 microns, AJ, 90, 896–899

Chandrasekhar, S., 1960, Radiative transfer, New York: Dover, 1960

Chirikov, B. V., 1960, Resonance processes in magnetic traps, Journal of Plasma Physics, 1, 253–260

Christy, J. W., Harrington, R. S., 1978, The satellite of Pluto, AJ, 83, 1005–1008

Cook, J. C., Desch, S. J., Roush, T. L., Trujillo, C. A., Geballe, T. R., 2007, Near-Infrared Spectroscopy of Charon: Possible Evidence for Cryovolcanism on Kuiper Belt Objects, ApJ, 663, 1406–1419

Cruikshank, D. P., Pilcher, C. B., Morrison, D., 1976, Pluto - Evidence for methane frost, Science, 194, 835–837

Cruikshank, D. P., Allamandola, L. J., Hartmann, W. K., Tholen, D. J., Brown, R. H., Matthews, C. N., Bell, J. F., 1991, Solid C triple bond N bearing material on outer solar system bodies, Icarus, 94, 345–353

Cruikshank, D. P., Roush, T. L., Owen, T. C., Geballe, T. R., de Bergh, C., Schmitt, B., Brown, R. H., Bartholomew, M. J., 1993, Ices on the surface of Triton, Science, 261, 742–745

Cruikshank, D. P., Roush, T. L., Poulet, F., 2003, Quantitative modeling of the spectral reflectance of Kuiper Belt objects and Centaurs, Comptes Rendus Physique, 4, 783–789

Cruikshank, D. P., Imanaka, H., Dalle Ore, C. M., 2005, Tholins as coloring agents on outer Solar System bodies, Advances in Space Research, 36, 178–183

de Bergh, C., Boehnhardt, H., Barucci, M. A., Lazzarin, M., Fornasier, S., Romon-Martin, J., Tozzi, G. P., Doressoundiram, A., Dotto, E., 2004, Aqueous altered silicates at the surface of two Plutinos?, A&A, 416, 791–798

de Bergh, C., Schmitt, B., Moroz, L. V., Quirico, E., Cruikshank, D. P., 2008, Laboratory Data on Ices, Refractory Carbonaceous Materials, and Minerals Relevant to Transneptunian Objects and Centaurs, pp. 483–506, The Solar System Beyond Neptune

dello Russo, N., Khanna, R. K., 1996, Laboratory Infrared Spectroscopic Studies of Crystalline Nitriles with Relevance to Outer Planetary Systems, Icarus, 123, 366–395

Delsanti, A., Jewitt, D., 2006, The Solar System Beyond The Planets, pp. 267–294, Solar System Update

Delsanti, A., Peixinho, N., Boehnhardt, H., Barucci, A., Merlin, F., Doressoundiram, A., Davies, J. K., 2006, Near-Infrared Color Properties of Kuiper Belt Objects and Centaurs: Final Results from the ESO Large Program, AJ, 131, 1851–1863

Delsemme, A. H., 1982, Chemical composition of cometary nuclei, in IAU Colloq. 61: Comet Discoveries, Statistics, and Observational Selection, (Ed.) L. L. Wilkening, pp. 85–130

Demeo, F. E., Fornasier, S., Barucci, M. A., Perna, D., Protopapa, S., Alvarez-Candal, A., Delsanti, A., Doressoundiram, A., Merlin, F., de Bergh, C., 2009, Visible and near-infrared colors of Transneptunian objects and Centaurs from the second ESO large program, A&A, 493, 283–290

Devillard, N., 1997, The eclipse software., The Messenger, 87, 19–20

Domingue, D., Hapke, B., 1992, Disk-resolved photometric analysis of Europan terrains, Icarus, 99, 70–81

Doressoundiram, A., Barucci, M. A., Romon, J., Veillet, C., 2001, Multicolor Photometry of Trans-neptunian Objects, Icarus, 154, 277–286

Doressoundiram, A., Peixinho, N., de Bergh, C., Fornasier, S., Thébault, P., Barucci, M. A., Veillet, C., 2002, The Color Distribution in the Edgeworth-Kuiper Belt, AJ, 124, 2279–2296

Doressoundiram, A., Tozzi, G. P., Barucci, M. A., Boehnhardt, H., Fornasier, S., Romon, J., 2003, ESO Large Programme on Trans-Neptunian Objects and Centaurs: Spectroscopic Investigation of Centaur 2001 BL_{41} and TNOs (26181) 1996 GQ_{21} and (26375) 1999 DE_9, AJ, 125, 2721–2727

Doressoundiram, A., Peixinho, N., Doucet, C., Mousis, O., Barucci, M. A., Petit, J. M., Veillet, C., 2005, The Meudon Multicolor Survey (2MS) of Centaurs and trans-neptunian objects: extended dataset and status on the correlations reported, Icarus, 174, 90–104

Doressoundiram, A., Boehnhardt, H., Tegler, S. C., Trujillo, C., 2008, Color Properties and Trends of the Transneptunian Objects, pp. 91–104, The Solar System Beyond Neptune

Dotto, E., Barucci, M. A., Boehnhardt, H., Romon, J., Doressoundiram, A., Peixinho, N., de Bergh, C., Lazzarin, M., 2003, Searching for water ice on 47171 1999 TC_{36}, 1998 SG35, and 2000 QC243: ESO large program on TNOs and centaurs*, Icarus, 162, 408–414

Douté, S., Schmitt, B., Quirico, E., Owen, T. C., Cruikshank, D. P., de Bergh, C., Geballe, T. R., Roush, T. L., 1999, Evidence for Methane Segregation at the Surface of Pluto, Icarus, 142, 421–444

Dumas, C., Merlin, F., Barucci, M. A., de Bergh, C., Hainault, O., Guilbert, A., Vernazza, P., Doressoundiram, A., 2007, Surface composition of the largest dwarf planet 136199 Eris (2003 UB_{313}), A&A, 471, 331–334

Duncan, M., Quinn, T., Tremaine, S., 1988, The origin of short-period comets, ApJ, 328, L69–L73

Duncan, M. J., Levison, H. F., Budd, S. M., 1995, The Dynamical Structure of the Kuiper Belt, AJ, 110, 3073–3081

Ehrenfreund, P., Boogert, A. C. A., Gerakines, P. A., Jansen, D. J., Schutte, W. A., Tielens, A. G. G. M., van Dishoeck, E. F., 1996, A laboratory database of solid CO and CO_2_ for ISO., A&A, 315, L341–L344

Fernandez, J. A., Ip, W.-H., 1981, Dynamical evolution of a cometary swarm in the outer planetary region, Icarus, 47, 470–479

Fornasier, S., Doressoundiram, A., Tozzi, G. P., Barucci, M. A., Boehnhardt, H., de Bergh, C., Delsanti, A., Davies, J., Dotto, E., 2004a, ESO Large Program on physical studies of Trans-Neptunian objects and Centaurs: Final results of the visible spectrophotometric observations, A&A, 421, 353–363

Fornasier, S., Dotto, E., Marzari, F., Barucci, M. A., Boehnhardt, H., Hainaut, O., de Bergh, C., 2004b, Visible spectroscopic and photometric survey of L5 Trojans: investigation of dynamical families, Icarus, 172, 221–232

Fulchignoni, M., Belskaya, I., Barucci, M. A., de Sanctis, M. C., Doressoundiram, A., 2008, Transneptunian Object Taxonomy, pp. 181–192, The Solar System Beyond Neptune

Gladman, B., Kavelaars, J. J., Petit, J.-M., Morbidelli, A., Holman, M. J., Loredo, T., 2001, The Structure of the Kuiper Belt: Size Distribution and Radial Extent, AJ, 122, 1051–1066

Gladman, B., Marsden, B. G., Vanlaerhoven, C., 2008, Nomenclature in the Outer Solar System, pp. 43–57, The Solar System Beyond Neptune

Goldreich, P., Lithwick, Y., Sari, R., 2002, Formation of Kuiper-belt binaries by dynamical friction and three-body encounters, Nature, 420, 643–646

Gomes, R., Levison, H. F., Tsiganis, K., Morbidelli, A., 2005, Origin of the cataclysmic Late Heavy Bombardment period of the terrestrial planets, Nature, 435, 466–469

Gomes, R. S., 2003, The origin of the Kuiper Belt high-inclination population, Icarus, 161, 404–418

Gomes, R. S., Fernàndez, J. A., Gallardo, T., Brunini, A., 2008, The Scattered Disk: Origins, Dynamics, and End States, pp. 259–273, The Solar System Beyond Neptune

Grundy, W. M., Buie, M. W., 2001, Distribution and Evolution of CH_4, N_2, and CO Ices on Pluto's Surface: 1995 to 1998, Icarus, 153, 248–263

Grundy, W. M., Buie, M. W., 2002, Spatial and Compositional Constraints on Non-ice Components and H_2O on Pluto's Surface, Icarus, 157, 128–138

Grundy, W. M., Fink, U., 1996, Synoptic CCD Spectrophotometry of Pluto Over the Past 15 Years, Icarus, 124, 329–343

Grundy, W. M., Schmitt, B., 1998, The temperature-dependent near-infrared absorption spectrum of hexagonal H_2O ice, J. Geophys. Res., 103, 25 809–25 822

Grundy, W. M., Schmitt, B., Quirico, E., 1993, The Temperature-Dependent Spectra of α and β Nitrogen Ice with Application to Triton, Icarus, 105, 254–258

Grundy, W. M., Buie, M. W., Spencer, J. R., 2002a, Spectroscopy of Pluto and Triton at 3-4 Microns: Possible Evidence for Wide Distribution of Nonvolatile Solids, AJ, 124, 2273–2278

Grundy, W. M., Schmitt, B., Quirico, E., 2002b, The Temperature-Dependent Spectrum of Methane Ice I between 0.7 and 5 μm and Opportunities for Near-Infrared Remote Thermometry, Icarus, 155, 486–496

Grundy, W. M., Noll, K. S., Stephens, D. C., 2005, Diverse albedos of small trans-neptunian objects, Icarus, 176, 184–191

Hapke, B., 1981, Bidirectional reflectance spectroscopy. 1. Theory, J. Geophys. Res., 86, 4571–4586

Hapke, B., 1984, Bidirectional reflectance spectroscopy. III - Correction for macroscopic roughness, Icarus, 59, 41–59

Hapke, B., 1986, Bidirectional reflectance spectroscopy. IV - The extinction coefficient and the opposition effect, Icarus, 67, 264–280

Hapke, B., 1993, Theory of reflectance and emittance spectroscopy, Topics in Remote Sensing, Cambridge, UK: Cambridge University Press

Hapke, B., 2002, Bidirectional Reflectance Spectroscopy5. The Coherent Backscatter Opposition Effect and Anisotropic Scattering, Icarus, 157, 523–534

Hardorp, J., 1980, The sun among the stars. III - Energy distributions of 16 northern G-type stars and the solar flux calibration, A&A, 91, 221–232

Henyey, L. G., Greenstein, J. L., 1941, Diffuse radiation in the Galaxy, ApJ, 93, 70–83

Hillier, J., Veverka, J., Helfenstein, P., Lee, P., 1994, Photometric diversity of terrains on Triton, Icarus, 109, 296–312

Horne, K., 1986, An optimal extraction algorithm for CCD spectroscopy, PASP, 98, 609–617

Imanaka, H., Khare, B. N., Elsila, J. E., Bakes, E. L. O., McKay, C. P., Cruikshank, D. P., Sugita, S., Matsui, T., Zare, R. N., 2004, Laboratory experiments of Titan tholin formed in cold plasma at various pressures: implications for nitrogen-containing polycyclic aromatic compounds in Titan haze, Icarus, 168, 344–366

Jewitt, D., Luu, J., Marsden, B. G., 1992, 1992 QB1, IAU Circ., 5611, 1

Jewitt, D. C., Luu, J., 2004, Crystalline water ice on the Kuiper belt object (50000) Quaoar, Nature, 432, 731–733

Jewitt, D. C., Luu, J. X., 2001, Colors and Spectra of Kuiper Belt Objects, AJ, 122, 2099–2114

Kenyon, S. J., Luu, J. X., 1998, Accretion in the Early Kuiper Belt. I. Coagulation and Velocity Evolution, AJ, 115, 2136–2160

Kenyon, S. J., Luu, J. X., 1999a, Accretion in the Early Kuiper Belt. II. Fragmentation, AJ, 118, 1101–1119

Kenyon, S. J., Luu, J. X., 1999b, Accretion in the Early Outer Solar System, ApJ, 526, 465–470

Khare, B. N., Sagan, C., Arakawa, E. T., Suits, F., Callcott, T. A., Williams, M. W., 1984, Optical constants of organic tholins produced in a simulated Titanian atmosphere - From soft X-ray to microwave frequencies, Icarus, 60, 127–137

Khare, B. N., Thompson, W. R., Murray, B. G. J. P. T., Chyba, C. F., Sagan, C., Arakawa, E. T., 1989, Solid organic residues produced by irradiation of hydrocarbon-containing H2O and H2O/NH3 ices - Infrared spectroscopy and astronomical implications, Icarus, 79, 350–361

Khare, B. N., Sagan, C., Heinrich, M., Thompson, W. R., Arakawa, E. T., Tuminello, P. S., Clark, M., 1994, Optical Constants of Triton Tholin: Preliminary Results, in Bulletin of the American Astronomical Society, vol. 26 of Bulletin of the American Astronomical Society, p. 1176

Krasnopolsky, V. A., Cruikshank, D. P., 1999, Photochemistry of Pluto's atmosphere and ionosphere near perihelion, J. Geophys. Res., 104, 21 979–21 996

Kuchner, M. J., Brown, M. E., Holman, M., 2002, Long-Term Dynamics and the Orbital Inclinations of the Classical Kuiper Belt Objects, AJ, 124, 1221–1230

Lazzarin, M., Barucci, M. A., Boehnhardt, H., Tozzi, G. P., de Bergh, C., Dotto, E., 2003, ESO Large Programme on Physical Studies of Trans-Neptunian Objects and Centaurs: Visible Spectroscopy, AJ, 125, 1554–1558

Levison, H. F., Stern, S. A., 2001, On the Size Dependence of the Inclination Distribution of the Main Kuiper Belt, AJ, 121, 1730–1735

Levison, H. F., Morbidelli, A., Vanlaerhoven, C., Gomes, R., Tsiganis, K., 2008, Origin of the structure of the Kuiper belt during a dynamical instability in the orbits of Uranus and Neptune, Icarus, 196, 258–273

Licandro, J., Grundy, W. M., Pinilla-Alonso, N., Leisy, P., 2006a, Visible spectroscopy of 2003 UB_{313}: evidence for N_2 ice on the surface of the largest TNO?, A&A, 458, L5–L8

Licandro, J., Pinilla-Alonso, N., Pedani, M., Oliva, E., Tozzi, G. P., Grundy, W. M., 2006b, The methane ice rich surface of large TNO 2005 FY_9: a Pluto-twin in the trans-neptunian belt?, A&A, 445, L35–L38

Malhotra, R., 1996, The Phase Space Structure Near Neptune Resonances in the Kuiper Belt, AJ, 111, 504–516

Margot, J. L., Brown, M. E., Trujillo, C. A., Sari, R., 2004, HST observations of Kuiper Belt binaries, in Bulletin of the American Astronomical Society, vol. 36, p. 1081

Masterson, C. M., Khanna, R. K., 1990, Absorption intensities and complex refractive indices of crystalline HCN, HC3N, and C_4N_2 in the infrared region, Icarus, 83, 83–92

McBride, N., Green, S. F., Davies, J. K., Tholen, D. J., Sheppard, S. S., Whiteley, R. J., Hillier, J. K., 2003, Visible and infrared photometry of Kuiper Belt objects: searching for evidence of trends, Icarus, 161, 501–510

McDonald, G. D., Thompson, W. R., Heinrich, M., Khare, B. N., Sagan, C., 1994, Chemical investigation of Titan and Triton tholins, Icarus, 108, 137–145

Merlin, F., Barucci, M. A., Dotto, E., de Bergh, C., Lo Curto, G., 2005, Search for surface variations on TNO 47171 and Centaur 32532, A&A, 444, 977–982

Merlin, F., Alvarez, A., Barucci, M., Delsanti, A., Fornasier, S., de Bergh, C., 2007, Spectrum of Eris from 0.5 to 2.4 Microns. Clues for a Stratified Surface., in AAS/Division for Planetary Sciences Meeting Abstracts, vol. 39

Morbidelli, A., 2002, Modern Integrations of Solar System Dynamics, Annual Review of Earth and Planetary Sciences, 30, 89–112

Morbidelli, A., Levison, H. F., 2003, Planetary science: Kuiper-belt interlopers, Nature, 422, 30–31

Morbidelli, A., Levison, H. F., Gomes, R., 2008, The Dynamical Structure of the Kuiper Belt and Its Primordial Origin, pp. 275–292, The Solar System Beyond Neptune

Noll, K. S., Grundy, W. M., Chiang, E. I., Margot, J.-L., Kern, S. D., 2008, Binaries in the Kuiper Belt, pp. 345–363, The Solar System Beyond Neptune

Olkin, C. B., Young, E. F., Young, L. A., Grundy, W., Schmitt, B., Tokunaga, A., Owen, T., Roush, T., Terada, H., 2007, Pluto's Spectrum from 1.0 to 4.2 μm: Implications for Surface Properties, AJ, 133, 420–431

Ortiz, J. L., Gutiérrez, P. J., Casanova, V., Sota, A., 2003, A study of short term rotational variability in TNOs and Centaurs from Sierra Nevada Observatory, A&A, 407, 1149–1155

Owen, T. C., Roush, T. L., Cruikshank, D. P., Elliot, J. L., Young, L. A., de Bergh, C., Schmitt, B., Geballe, T. R., Brown, R. H., Bartholomew, M. J., 1993, Surface ices and the atmospheric composition of Pluto, Science, 261, 745–748

Palumbo, M. E., Strazzulla, G., 1993, The 2140/cm band of frozen CO - Laboratory experiments and astrophysical applications, A&A, 269, 568–580

Peixinho, N., Doressoundiram, A., Romon-Martin, J., 2002, Visible-IR colors and lightcurve analysis of two bright TNOs: 1999 TC_{36} and 1998 SN_{165}, New Astronomy, 7, 359–367

Persson, S. E., Murphy, D. C., Krzeminski, W., Roth, M., Rieke, M. J., 1998, A New System of Faint Near-Infrared Standard Stars, AJ, 116, 2475–2488

Poulet, F., Cuzzi, J. N., Cruikshank, D. P., Roush, T., Dalle Ore, C. M., 2002, Comparison between the Shkuratov and Hapke Scattering Theories for Solid Planetary Surfaces: Application to the Surface Composition of Two Centaurs, Icarus, 160, 313–324

Protopapa, S., Alvarez-Candal, A., Barucci,, M. A., Tozzi, G. P., Fornasier, S., Delsanti, A., Merlin, F., 2008a, ESO large program about TNOs: Surface variations on (47171) 1999 TC_{36}, A&A, in press

Protopapa, S., Boehnhardt, H., Herbst, T. M., Cruikshank, D. P., Grundy, W. M., Merlin, F., Olkin, C. B., 2008b, Surface characterization of Pluto and Charon by L and M band spectra, A&A, 490, 365–375

Quirico, E., Schmitt, B., 1997a, A Spectroscopic Study of CO Diluted in N_2 Ice: Applications for Triton and Pluto, Icarus, 128, 181–188

Quirico, E., Schmitt, B., 1997b, Near-Infrared Spectroscopy of Simple Hydrocarbons and Carbon Oxides Diluted in Solid N_2 and as Pure Ices: Implications for Triton and Pluto, Icarus, 127, 354–378

Quirico, E., Schmitt, B., Bini, R., Salvi, P. R., 1996, Spectroscopy of some ices of astrophysical interest: SO_2, N_2 and N_2:CH_4 mixtures, Planet. Space Sci., 44, 973–986

Quirico, E., Doute, S., Schmitt, B., de Bergh, C., Cruikshank, D. P., Owen, T. C., Geballe, T. R., Roush, T. L., 1999, Composition, Physical State, and Distribution of Ices at the Surface of Triton, Icarus, 139, 159–178

Romon-Martin, J., Barucci, M. A., de Bergh, C., Doressoundiram, A., Peixinho, N., Poulet, F., 2002, Observations of Centaur 8405 Asbolus: Searching for Water Ice, Icarus, 160, 59–65

Roush, T. L., 1994, Charon: More than water ice?, Icarus, 108, 243–254

Roush, T. L., 1996, Near-IR (0.8-2.5 micrometers) Optical Constants of Water Ice at 100K, in Lunar and Planetary Institute Conference Abstracts, vol. 27 of Lunar and Planetary Institute Conference Abstracts, p. 1107

Schaller, E. L., Brown, M. E., 2007a, Volatile Loss and Retention on Kuiper Belt Objects, ApJ, 659, L61–L64

Schaller, E. L., Brown, M. E., 2007b, Detection of Methane on Kuiper Belt Object (50000) Quaoar, ApJ, 670, L49–L51

Schmitt, B., Quirico, E., 1992, Laboratory Data on Near-Infrared Spectra of Ices of Planetary Interest, in Bulletin of the American Astronomical Society, vol. 24 of Bulletin of the American Astronomical Society, p. 968

Schmitt, B., Quirico, E., Lellouch, E., 1992, Near infrared spectra of potential solids at the surface of Titan, in Symposium on Titan, (Ed.) B. Kaldeich, vol. 338 of ESA Special Publication, pp. 383–388

Schuster, A., 1905, Radiation Through a Foggy Atmosphere, ApJ, 21, 1–22

Shkuratov, Y., Starukhina, L., Hoffmann, H., Arnold, G., 1999, A Model of Spectral Albedo of Particulate Surfaces: Implications for Optical Properties of the Moon, Icarus, 137, 235–246

Spencer, J. R., Buie, M. W., Bjoraker, G. L., 1990, Solid methane on Triton and Pluto - 3- to 4-micron spectrophotometry, Icarus, 88, 491–496

Stansberry, J., Grundy, W., Brown, M., Cruikshank, D., Spencer, J., Trilling, D., Margot, J.-L., 2008, Physical Properties of Kuiper Belt and Centaur Objects: Constraints from the Spitzer Space Telescope, pp. 161–179, The Solar System Beyond Neptune

Stansberry, J. A., Grundy, W. M., Margot, J. L., Cruikshank, D. P., Emery, J. P., Rieke, G. H., Trilling, D. E., 2006, The Albedo, Size, and Density of Binary Kuiper Belt Object (47171) 1999 TC_{36}, ApJ, 643, 556–566

Stephens, D. C., Noll, K. S., 2006, Detection of Six Trans-Neptunian Binaries with NIC-MOS: A High Fraction of Binaries in the Cold Classical Disk, AJ, 131, 1142–1148

Stern, S. A., Colwell, J. E., 1997a, Accretion in the Edgeworth-Kuiper Belt: Forming 100-1000 KM Radius Bodies at 30 AU and Beyond., AJ, 114, 841–849

Stern, S. A., Colwell, J. E., 1997b, Collisional Erosion in the Primordial Edgeworth-Kuiper Belt and the Generation of the 30-50 AU Kuiper Gap, ApJ, 490, 879–882

Stern, S. A., Weaver, H. A., Steffl, A. J., Mutchler, M. J., Merline, W. J., Buie, M. W., Young, E. F., Young, L. A., Spencer, J. R., 2006, A giant impact origin for Pluto's small moons and satellite multiplicity in the Kuiper belt, Nature, 439, 946–948

Szokoly, G. P., 2005, Optimal slit orientation for long multi-object spectroscopic exposures, A&A, 443, 703–707

Tegler, S. C., Grundy, W. M., Romanishin, W., Consolmagno, G. J., Mogren, K., Vilas, F., 2007, Optical Spectroscopy of the Large Kuiper Belt Objects 136472 (2005 FY_9) and 136108 (2003 EL_{61}), AJ, 133, 526–530

Tegler, S. C., Grundy, W. M., Vilas, F., Romanishin, W., Cornelison, D. M., Consolmagno, G. J., 2008, Evidence of N_2-ice on the surface of the icy dwarf Planet 136472 (2005 FY_9), Icarus, 195, 844–850

Trujillo, C. A., Brown, M. E., 2001, The Radial Distribution of the Kuiper Belt, ApJ, 554, L95–L98

Trujillo, C. A., Brown, M. E., 2002, 1999 TC_{36}, IAU Circ., 7787, 1

Trujillo, C. A., Brown, M. E., Barkume, K. M., Schaller, E. L., Rabinowitz, D. L., 2007, The Surface of 2003 EL_{61} in the Near-Infrared, ApJ, 655, 1172–1178

Tryka, K. A., Brown, R. H., Chruikshank, D. P., Owen, T. C., Geballe, T. R., Debergh, C., 1994, Temperature of nitrogen ice on Pluto and its implications for flux measurements, Icarus, 112, 513–527

Tsiganis, K., Gomes, R., Morbidelli, A., Levison, H. F., 2005, Origin of the orbital architecture of the giant planets of the Solar System, Nature, 435, 459–461

Veillet, C., Doressoundiram, A., Shapiro, J., Kavelaars, J. J., Morbidelli, A., 2001, S/2000 (1998 WW$_{31}$) 1, IAU Circ., 7610, 1

Warren, S. G., 1984, Optical constants of ice from the ultraviolet to the microwave, Appl. Opt., 23, 1206–1225

Weaver, H. A., Stern, S. A., Mutchler, M. J., Steffl, A. J., Buie, M. W., Merline, W. J., Spencer, J. R., Young, E. F., Young, L. A., 2006, Discovery of two new satellites of Pluto, Nature, 439, 943–945

Weaver, H. A., Gibson, W. C., Tapley, M. B., Young, L. A., Stern, S. A., 2008, Overview of the New Horizons Science Payload, Space Science Reviews, p. 85

Whitaker, E. A., 1969, An Investigation of the Lunar Heiligenschein, NASA Special Publication, 201, 38

Young, E. F., Galdamez, K., Buie, M. W., Binzel, R. P., Tholen, D. J., 1999, Mapping the Variegated Surface of Pluto, AJ, 117, 1063–1076

Young, L. A., Stern, S. A., Weaver, H. A., Bagenal, F., Binzel, R. P., Buratti, B., Cheng, A. F., Cruikshank, D., Gladstone, G. R., Grundy, W. M., Hinson, D. P., Horanyi, M., Jennings, D. E., Linscott, I. R., McComas, D. J., McKinnon, W. B., McNutt, R., Moore, J. M., Murchie, S., Porco, C. C., Reitsema, H., Reuter, D. C., Spencer, J. R., Slater, D. C., Strobel, D., Summers, M. E., Tyler, G. L., 2008, New Horizons: Anticipated Scientific Investigations at the Pluto System, Space Science Reviews, in press

Zheng, W., Jewitt, D., Kaiser, R. I., 2008, Amorphization of Crystalline Water Ice, ArXiv e-prints, 801

Zubko, V. G., Mennella, V., Colangeli, L., Bussoletti, E., 1996, Optical constants of cosmic carbon analogue grains - I. Simulation of clustering by a modified continuous distribution of ellipsoids, MNRAS, 282, 1321–1329

Publications

Refereed contributions:

Protopapa, **S.**, Boehnhardt, H., Herbst, T. M., Cruikshank, D. P., Grundy, W. M., Merlin, F., and Olkin, C. B., *Surface characterization of Pluto and Charon by L and M band spectra*, 2008, A&A, 490, 365

Protopapa, **S.**, Alvarez-Candal, A., Barucci, M. A., Tozzi, G. P., Fornasier, S., Delsanti, A., and Merlin, F., *ESO large program about TNOs: Surface variations on (47171) 1999 TC_{36}*, A&A, in press

Non refereed contributions:

Protopapa, **S.**, Herbst, T., Boehnhardt, H., *Surface ice spectroscopy of Pluto, Charon and Triton*, 2007, The Messenger, 129, 58

Posters and Presentations:

Protopapa, **S.**, Boehnhardt, H., Herbst, T. M., Cruikshank, D. P., Grundy, W. M., Merlin, F., and Olkin, C. B., *Spectra of Pluto and Charon resolved up to 5µm: Implication for surface properties*. ACM, Baltimore, July 13-18, 2008. (Oral)

Protopapa, **S.**, Boehnhardt, H., Herbst, T., Merlin, F., Cruikshank, D. P., Grundy, W. M., *Surface Ice Spectroscopy of Pluto and Charon Resolved*. DPS meeting, Orlando, October 7-12, 2007. (Oral)

Protopapa, **S.**, Herbst, T., Boehnhardt, H., *Surface ice spectroscopy of Pluto, Charon and Triton*. European Planetary Science Congress, Potsdam, August 19-24, 2007. (Oral)

Protopapa, **S.**, Herbst, T., Boehnhardt, H., Gruen, E., Grundy, W. M., Spencer, J. A., Stern, A., *J and M band spectroscopy of Pluto and Charon*. Trans Neptunian Objects: Dynamical and Physical properties, Catania, July 3-7, 2006. (Oral)

Acknowledgements

It seems yesterday I came for the first time in this village, I entered in the Max-Planck-Institute knowing the importance of the place where I was, longing to be accepted as PhD student... and now, here I am, closing this wonderful period I spent at the limit between student and researcher.

First and foremost, I would like to thank my supervisor, Dr. Hermann Boehnhardt, for accepting me as his PhD student with the challenging and exiting topic I worked on. His capability to communicate with me especially at the beginning of this adventure, in spite of my sort (more than a sort!) of language barrier, made me understanding his character, calm and patient. I have to thank Hermann for always letting me trying, without pushing for an immediate result, and giving me smart inputs when I was stuck. He gave me the possibility to learn from him and from other many "celebrities" of the Transneptunian studies, like M.A. Barucci (LESIA, Observatoire de Paris), D. Cruikshank (NASA Ames Research Center), W. Grundy (Lowell Observatory), C. Olkin (Department of Space Studies, Southwest Research Institute). All these persons have collaborated to the successful completion of this thesis. In particular, I thank M.A. Barucci for giving me the possibility to work for the Large Program, D. Cruikshank for making available to me his experience in terms of planetary analogues, W. Grundy and C. Olkin for long email exchanges to discuss about the Hapke radiative transfer model and the modeling results presented in this thesis. Moreover, I wish to thank Gian Paolo Tozzi and Luis Barrera, two irreplaceable observing campaigners. I am grateful to Frederic Merlin, for providing me the first version of the modeling algorithm, and to Sonia Fornasier for making me understanding what means to be perseverant in trying to get always the best result.

A particular thank goes to Dr. Dieter Schmitt for giving me the support of the IM-PRS school and for allowing me to discover various aspects of the Solar System research, through the very interesting courses and retreats. I am also glad to thank my Braunschweig supervisor, Prof. Dr. Jürgen Blum, for having always shown interest and curiosity toward my work and for having given me important insights.

In addition to all the important people in my research life, I am grateful to all my friends who have contributed to make this period in Lindau joyful and unforgettable. A particular thank goes to Clementina Sasso and Luca Maltagliati, that since the first day made me feeling at home. A particular acknowledgement goes to Luca, for having the lucky opportunity to read all this thesis long in advance! No acknowledgments would be complete without mentioning the other friends came along me during these three years: Maya, Rupali, Gennaro, Cecilia, Nico, Anya, Richard, Pedro, Manuela (a really good friend and colleague), Julia, Philippe, Michal, Ray, Hannah, Maria, Judith.

A special thank goes to my family: my beloved husband (this is another merit of the Max-Planck-Institute!), my father and all my sisters and their respective husbands. They

have been always by my side. Particularly important since the beginning of my scientific carrier has been Francesco, with his strong enthusiasm for science and long experience.

Curriculum Vitae

Persönlische daten

Name: Silvia Protopapa

Geburtsdatum: 15. July 1981

Geburtsort: Galatina, Italien

Staatsangehörigkeit: italienisch

Schulausbildung

1987–1992 Scuola Elementare Statale "via Spoleto", Galatina, Italien

1992–1995 Scuola Media Statale "Giovanni XXIII", Galatina, Italien

1995–2000 Liceo Scientifico di Stato "A. Vallone", Galatina, Italien

Studium

2000–2005 Degree in Physics
           Università degli Studi di Lecce, Italien